

Efficient Coupling between Optical Fibers and Photonic Integrated Circuits

Von der Fakultät Informatik, Elektrotechnik und Informationstechnik
der Universität Stuttgart

zur Erlangung der Würde eines Doktor-Ingenieurs (Dr.-Ing.)
genehmigte Abhandlung

Vorgelegt von

Wissem Sfar Zaoui

aus Sousse (Tunesien)

Hauptberichter: Prof. Dr.-Ing. Manfred Berroth

Mitberichter: Prof. Dr.-Ing. Joachim Burghartz

Tag der mündlichen Prüfung: 28. November 2014

Institut für Elektrische und Optische Nachrichtentechnik
der Universität Stuttgart

2014

Contents

Abbreviations and symbols	IV
Zusammenfassung	XIII
Abstract	XVI
1. Introduction	1
1.1. Motivation	1
1.2. State-of-the-art fiber-to-chip couplers	4
1.3. Objective and outline of the thesis	7
2. Coupling issue between optical fibers and PICs	9
2.1. Nanophotonics technology	9
2.2. Coupling concepts	11
2.2.1. On-fiber nanocouplers	11
2.2.2. Stand-alone nanocouplers.....	13
2.2.3. On-chip nanocouplers.....	15
2.3. Conclusion.....	17
3. Fundamentals of optical data transmission	19
3.1. Components of optical transmission systems.....	19
3.1.1. Transmitter concepts	20
3.1.2. Optical links.....	24
3.1.3. Receiver concepts	25
3.2. Electromagnetic wave propagation	27
3.2.1. Wave equations.....	27
3.2.2. Reflection and refraction	31
3.2.3. Interference and diffraction	33
3.3. Waveguiding effect.....	38
3.3.1. Planar waveguides	39
3.3.2. Strip waveguides	40

3.3.3. Single-mode optical fibers	44
3.4. Wave propagation in periodic media	45
4. Negative index metamaterials	47
4.1. Theory of metamaterials	47
4.1.1. The negative refractive index	48
4.1.2. Homogenization and retrieval procedure	49
4.2. Negative index lenses as nanocouplers	52
4.3. Design of negative index metamaterials	57
4.3.1. Single layer	57
4.3.2. Multilayer	61
4.3.3. Focusing ability of the designed metamaterial	66
4.4. Characterization of the internal properties	67
4.4.1. Measurement setup	68
4.4.2. Measured S-parameters and retrieved properties	69
4.5. Focusing ability of the fabricated metamaterial	72
4.5.1. Measurement setup	72
4.5.2. Measured field distribution and focus position	73
4.6. Negative index metamaterials at optical frequencies	76
4.7. Conclusion	78
5. Bragg diffraction gratings	80
5.1. Theory of grating couplers	80
5.2. Diffraction gratings as nanocouplers	84
5.3. Design of periodic gratings	87
5.4. Optimization procedure	90
5.4.1. Improvement of the directionality	90
5.4.2. Enhancement of the modal overlap	93
5.5. Fabrication process	99
5.6. Characterization of the structures	101
5.6.1. Measurement setup	101
5.6.2. Periodic grating couplers	103
5.6.3. Aperiodic grating couplers	105

5.7. Conclusion	109
6. Summary and outlook.....	111
6.1. Summary.....	111
6.2. Outlook	113
Appendix	114
A. Diffraction at different slit apertures	114
A.1. Rectangular single-slit aperture	114
A.2. Circular single-slit aperture	115
A.3. N -slits aperture.....	117
B. Equivalent LC circuit of a fishnet NIM	119
C. Design of an aspheric lens at radio frequencies.....	121
D. Waveguide losses.....	122
E. 1D Bragg gratings for TM coupling.....	124
E.1. Single polarization coupling	124
E.2. Polarization beam splitting.....	125
References.....	127
Personal publications	138
Curriculum Vitae.....	142
Acknowledgment	143

Abbreviations and symbols

Abbreviations

<i>Abbreviation</i>	<i>Description</i>
1D	One-dimensional
2D	Two-dimensional
3D	Three-dimensional
ADC	Analog-to-digital converter
ADS	Advanced Design System
Ag	Silver
Al	Aluminum
AOC	Active optical cable
ARC	Antireflection coating
ASK	Amplitude shift keying
AWG	Arrayed waveguide grating
BER	Bit error rate
BOX	Buried oxide
BW	Beam waist
CMOS	Complementary metal-oxide-semiconductor
CST MWS	Computer Simulation Technology Microwave Studio
CUHK	The Chinese University of Hong Kong
CW	Continuous wave
DAC	Digital-to-analog converter
DBR	Distributed Bragg reflector
DFB	Distributed feedback
DLI	Delay line interferometer
DP	Dual polarization
DPSK	Differential phase shift keying
DSP	Digital signal processor

DUT	Device under test
EO	Electro-optical
EON	Elastic optical network
FDTD	Finite-difference time domain
FF	Fill factor
FFL	Front focal length
FOM	Figure of merit
FSR	Free spectral range
FTTB	Fiber-to-the-building
FTTH	Fiber-to-the-home
GeO ₂	Germanium dioxide
GRIN	Gradient index
I	In-phase carrier signal
IC	Integrated circuit
IMEC	Interuniversity Microelectronics Centre
IMS CHIPS	Institute for Microelectronics Stuttgart
InP	Indium phosphide
INT	Institute of Electrical and Optical Communications Engineering
LC	Inductive-capacitive
LD	Laser diode
LED	Light emitting diode
LO	Local oscillator
MFD	Mode field diameter
MIL	Matching index liquid
MMF	Multimode fiber
MMI	Multimode interferometer
MZM	Mach-Zehnder modulator
NA	Numerical aperture
NIM	Negative index metamaterial
NSOM	Near field scanning optical microscope
OE	Opto-electrical
OEWG	Open-ended waveguide
OOK	On-off-keying

OSNR	Optical signal-to-noise ratio
PBS	Polarization beam splitter
PDM	Polarization division multiplexing
PIC	Photonic integrated circuit
PMF	Polarization maintaining fiber
PSK	Phase shift keying
Q	Quadrature carrier signal
QAM	Quadrature amplitude modulation
QPSK	Quadrature phase shift keying
SDM	Space division multiplexing
SEM	Scanning electron microscope
Si	Silicon
SiO ₂	Silicon dioxide
SMF	Single-mode fiber
SOI	Silicon-on-insulator
S-parameters	Scattering parameters
SPP	Surface plasmon polariton
SSC	Spot size converter
TE	Transverse electric
TIA	Transimpedance amplifier
TM	Transverse magnetic
TRM	Thru-reflect-match
UV	Ultraviolet
WDM	Wavelength division multiplexing

Symbols

<i>Symbol</i>	<i>Description</i>	<i>Unit</i>
Latin characters		
A	Area	m^2
A_{NIM}	Absorption coefficient of the NIM	
a_S	Setup loss	
$\underline{a}_{in,i}$	Complex amplitude of the incoming wave at port i	
$\underline{a}_{out,i}$	Complex amplitude of the outgoing wave at port i	
B	Phase parameter	
\vec{B}	Magnetic induction vector	Vs/m^2
b	Grating rib length	m
C	Constant used in the definition of the Fraunhofer integral	W/m^6
c	Wave phase velocity	m/s
c_0	Velocity of light in vacuum	m/s
D	Circular slit diameter, lens diameter	m
D_F	Fiber core diameter	m
D_f	Focused spot diameter	m
\vec{D}	Dielectric displacement vector	As/m^2
d	Metamaterial thickness	m
d_{ARC}	ARC thickness	m
d_{BOX}	BOX thickness	m
d_m	Metamaterial metallic layer thickness	m
d_s	Metamaterial substrate thickness	m
d_{sp}	Metamaterial spacer thickness	m
E_f	Electric field amplitude of the fundamental fiber mode	V/m
E_g	Electric field amplitude of the diffracted wave on the grating	V/m
E_p	Electric field amplitude of the beam at the focal plane	V/m
E_w	Electric field amplitude of the first-stage waveguide	V/m

$E_{x y}$	Electric field amplitude along the x y direction	V/m
\vec{E}, \vec{E}'	Electric field vector	V/m
$\vec{E}_{i r t}$	Electric field vector of the incident reflected transmitted wave	V/m
F	Lens focal length	m
f	Electromagnetic wave frequency	Hz
g	Grating groove length	m
\vec{H}, \vec{H}'	Magnetic field vector	A/m
$\vec{H}_{i r t}$	Magnetic field vector of the incident reflected transmitted wave	A/m
h	Film layer thickness	m
I, I_0	Intensity	W/m ²
i	Index	
J_1	Bessel function of the first kind of order 1	
\vec{J}	Current density vector	A/m ²
j	Unit imaginary number	
K	Grating reciprocal lattice	1/m
\vec{K}	Bloch wave vector	1/m
k	Wave number	1/m
k_0	Wave number in free space	1/m
k_T	Transverse wave vector component	1/m
k_i	Wave number of the incident wave	1/m
k_m	Wave number of the diffracted wave	1/m
\vec{k}	Wave vector	1/m
$\vec{k}_{i r t}$	Incident reflected transmitted wave vector	1/m
L_c	Cavity length	m
l	Slit length	m
m	Integer	
N	Number of slits, metamaterial layers, grating periods	

n	Refractive index	
n_{ARC}	Refractive index of the ARC	
n_{MIL}	Refractive index of the MIL	
n_{WG}	Refractive index of the waveguide material	
n_{air}	Refractive index of free space	
n_c	Refractive index of the cladding material	
n_{eff}	Effective refractive index	
$n_{\text{eff,TE TM}}$	Effective refractive index of the TE TM mode	
n_g	Group index	
n_i	Refractive index of medium i	
n_s	Refractive index of the substrate material	
\underline{n}	Complex refractive index	
$\underline{n}_{\text{eff}}$	Complex effective refractive index	
P	Optical power	W
$P_L, P_{L,\text{dBm}}$	Input optical power of the laser	W, dBm
$P_P, P_{P,\text{dBm}}$	Measured optical power at the power meter	W, dBm
P_{down}	Downward-diffracted optical power	W
P_{in}	Input optical power	W
P_{out}	Output optical power	W
P_s	Total scattered power	W
P_{up}	Upward-diffracted optical power	W
P_w	Diffracted optical power from the fiber into the waveguide	W
p	Index	
q	Positive integer	
R	Reflectivity	
R_{NIM}	Reflectivity of the NIM	
$R_{\text{TE TM}}$	Reflectivity of the TE TM wave	
R_a	Lens curvature radius	m

R_m	Metamaterial metallic cylinder radius	m
R_{up}	Upward reflectivity	
R_z, R_y	Major and minor radii of the confocal grating ellipses	m
r, r_0	Position in the Cartesian coordinate system	m
\vec{r}, \vec{r}'	Position vector	m
\underline{S}_{ij}	Complex S-parameters (squared amplitude)	
\vec{S}	Poynting vector	W/m ²
\underline{s}_{ij}	Complex S-parameters	
T	Transmissivity	
T_C	Transmissivity from free space to the cladding	
T_{NIM}	Transmissivity through the NIM	
$T_{TE TM}$	Transmissivity of the TE TM wave	
T_{WG}	Transmissivity to the waveguide	
T_{down}	Downward transmissivity to the substrate	
t	Time variable	s
V	Frequency parameter	
w	Slit width, waveguide width	m
w_0	Beam radius	m
w_{GC}	Width of the grating coupler	m
w_L	Width of the lens	m
w_i	Width of waveguide i	m
w_m	Metamaterial metallic wire width	m
x	Coordinate in the Cartesian system	m
y	Coordinate in the Cartesian system	m
y_f	y -coordinate of the common origin of confocal ellipses	m
Z	Wave impedance	Ω
Z_0	Wave impedance in free space	Ω
Z_i	Wave impedance in medium i	Ω

\underline{Z}	Complex wave impedance	Ω
z	Coordinate in the Cartesian system	m
z_f	z -coordinate of the common origin of confocal ellipses	m
\underline{z}	Complex relative wave impedance	
Greek characters		
α	Angle	$^\circ, \text{rad}$
α_c	Critical angle	$^\circ, \text{rad}$
$\alpha_{i r t}$	Angle of the incident reflected transmitted wave	$^\circ, \text{rad}$
α_m	Diffraction angle	$^\circ, \text{rad}$
β_m	Propagation constant of the diffracted wave in the waveguide	1/m
Γ	Reflection coefficient	
γ	Damping coefficient	1/s
$\gamma_{s c n}$	Auxiliary quantities	
$\Delta\lambda_{1\text{dB}}$	1 dB bandwidth	m
$\Delta\lambda_{3\text{dB}}$	3 dB bandwidth	m
$\Delta\varphi$	Phase difference	$^\circ, \text{rad}$
δ	Phase	$^\circ, \text{rad}$
ε_0	Dielectric constant in free space	As/(Vm)
$\varepsilon_r, \varepsilon'_r$	Relative permittivity	
$\varepsilon_{r,\infty}$	High-frequency relative permittivity	
$\underline{\varepsilon}_r$	Complex relative permittivity	
$\underline{\varepsilon}_{r,\text{eff}}$	Complex effective relative permittivity	
η, η_{dB}	Coupling efficiency	
η_D	Directionality of the grating coupler	
η_{GC}	Coupling efficiency of the grating coupler	
η_O	Overlap integral	
η_T	Mode conversion efficiency of the taper	
κ	Extinction coefficient	

κ_{GC}	Coupling strength of the grating	1/m
Λ	Slit period, metamaterial period, grating period	m
$\vec{\Lambda}$	Lattice vector	m
λ	Wavelength	m
λ_0	Wavelength in free space	m
μ_0	Magnetic constant in free space	Vs/(Am)
μ_r	Relative permeability	
$\underline{\mu}_r$	Complex relative permeability	
$\underline{\mu}_{r,eff}$	Complex effective relative permeability	
ν	Scaling factor	
$\vec{\xi}$	Electric or magnetic field vector	V/m, A/m
ρ	Charge density	C/m ³
σ	Conductivity	S/m
ϕ_G	Goos-Hänchen phase shift	°, rad
ω, ω'	Electromagnetic wave angular frequency	rad/s
ω_p	Plasma angular frequency	rad/s

Zusammenfassung

Die photonische Integration hat in der näheren Vergangenheit beachtliche Fortschritte gemacht, ähnlich denen der Integration elektronischer Schaltkreise vor ca. fünfzig Jahren. Speziell für die optische Kommunikation wird diese rasche Entwicklung nicht nur die Übertragung größerer Datenmengen ermöglichen, sondern auch die kostengünstigere Massenproduktion, die Minimierung des Montageaufwands und die Reduzierung des Energieverbrauchs. Weitere Vorteile der photonischen Integration können erreicht werden, wenn für die Umsetzung die Silizium-Plattform dank der fortgeschrittenen komplementären Metall-Oxid-Halbleiter-Technologie genutzt wird. Somit können die zunehmend komplexen Sender- und Empfänger-Architekturen kostengünstiger hergestellt werden.

Die Silizium-Plattform bietet außerdem einen hohen Brechungsindexkontrast, was die Realisierung von kompakten photonischen Schaltungen auf kleinsten Chipflächen ermöglicht. Allerdings stellt die Miniaturisierung der Dimensionen ein Hindernis für die Anbindung an die vorhandenen optischen Glasfasern dar. Während die integrierten Wellenleiterstrukturen einen Querschnitt der Größenordnung $0,1 \mu\text{m}^2$ haben, weist der optische Glasfaserkern eine Stirnfläche von $50 \mu\text{m}^2$ auf. Dieser große Unterschied kann zu beträchtlichen Einfüguungsverlusten führen, so dass ein bedeutendes Einkoppelproblem zwischen den integrierten Wellenleitern und den herkömmlichen Glasfasern auftritt.

Auf den ersten Blick könnte das Problem aufgrund der zahlreichen verfügbaren Einkoppelhilfen als trivial betrachtet werden. Diese beruhen auf konventionellen Methoden wie z.B. getaperten Glasfasern oder Linsensystemen. Allerdings fordern die strengen Spezifikationen in industriellen Anwendungen leistungsfähigere Methoden mit höherer Effizienz, kompakteren Dimensionen und flexiblerer Einkopplungstechnik. Für diesen Zweck wurde zwar eine Vielzahl von Ansätzen entwickelt, beginnend von dreidimensionalen Tapern bis hin zu photonischen Kristallen und plasmonischen Strukturen, aber keiner dieser Ansätze hat aufgrund diverser Nachteile den Sprung in konkrete Anwendungen geschafft.

Im Rahmen dieser Arbeit werden zwei verschiedene Vorgehen zur Glasfasereinkopplung untersucht. Die erste Methode beruht auf den Metamaterialien, die neuartige, nicht in der Natur bekannte Effekte ermöglichen. Die zweite Methode befasst sich mit anwendungsorientierteren Strukturen, die als Bragg-Beugungsgitter bekannt sind. Das gemeinsame Ziel der beiden Themen ist die konkrete Realisierung von hocheffizienten Kopplern, die den abrupten Übergang zwischen konventionellen optischen Glasfasern und integrierten einmodigen Silizium-Wellenleitern verringern. Als Richtwert soll die Koppeffizienz -1 dB übertreffen, während die 1 dB-Bandbreite größer als 35 nm sein soll, um das gesamte C-Band abzudecken.

Die Untersuchung der fokussierenden Metamaterialien wird im ersten Schritt bei Millimeterwellenlängen durchgeführt, da die Herstellung und die Charakterisierung der Strukturen einfacher als im Infrarot-Bereich sind. Das Hauptziel dieser Methode ist die Erzeugung eines negativen Brechungsindex, um ebene Wellen in einen schmalen Fokus bei einem kleinen Abstand zu konzentrieren. Darüber hinaus muss das Negativ-Index-Metamaterial kleine Reflexions- und Absorptionsverluste in einer großen Bandbreite aufweisen. Anschließend werden die Dimensionen der fokussierenden plankonkaven Negativ-Index-Linse in den Mikrometer-Bereich herunterskaliert, um deren Einsatz bei der Telekommunikationswellenlänge 1550 nm zu untersuchen.

Die einzelnen Schichten des Metamaterials wurden basierend auf den dielektrisch-metallischen Fischnetz-Strukturen entworfen und mittels herkömmlicher Ätzverfahren gefertigt. Das simulierte Design zeigt eine hohe Transmission von ca. $-0,5$ dB mit einem negativen Brechungsindex von -1 bei der Betriebsfrequenz 38,5 GHz und einer 1 dB-Bandbreite von 0,8 GHz. Die Messergebnisse stimmen mit den theoretischen Berechnungen gut überein. Um eine fokussierende Metamaterial-Linse zu bekommen, wird die Form des Stapels in eine plankonkave Konfiguration umgestaltet. Die Linse zeigt gute Fokussierungsfähigkeiten mit einer Reduzierung der Strahlbreite um einen Faktor von 2,2 bei einem Abstand von nur $6 \lambda_0$. Im Vergleich zur Negativ-Index-Linse zeigt eine asphärische plankonvexe dielektrische Linse die doppelte Breite bei einem Abstand von über $12 \lambda_0$.

Auch nach der Herunterskalierung der Dimensionen zeigt die Negativ-Index-Linse bei einer Frequenz von 193,55 THz, was einer Wellenlänge von 1550 nm entspricht, theore-

tisch ein ähnliches Verhalten mit einer Reduzierung der Strahlbreite um einen Faktor von 3,8 bei einem Abstand von $8,7 \lambda_0$. Trotz der vorteilhaften Eigenschaften dieser Linse für die Einkopplung zwischen Glasfasern und integrierten Wellenleitern zeigen sich die Metallverluste besonders deutlich und reduzieren die Gesamteffizienz auf kleiner als -2 dB. Daher lässt sich die Zieleffizienz mittels Metamaterialien nicht erreichen, solange die Absorptionsverluste im optischen Bereich nicht kompensiert werden.

Die zweite Einkoppelmethode in dieser Arbeit beschäftigt sich mit den Beugungsgittern. Diese Strukturen haben im Vergleich zur ersten Vorgehensweise den Vorteil, dass sie mit den integrierten Wellenleitern kostengünstiger auf dem Chip realisiert werden können. Außerdem bietet dieser Lösungsansatz eine zur Chipoberfläche nahezu senkrechte Einkopplung, und somit kann das Testen der Strukturen an einer beliebigen Stelle auf dem Wafer stattfinden, ohne dass es erforderlich ist, die Chips zu spalten und zu polieren. Des Weiteren besitzen die Beugungsgitter kompakte Dimensionen in der Größenordnung des Glasfaserkerns und können durch einfache adiabatische Taper oder fokussierende Ausfertigungen an die schmalen Wellenleiter angepasst werden.

Da die Koppel-effizienz von einem konventionellen Beugungsgitter relativ gering ist, werden die Verlustquellen analysiert. Hier stellen die niedrige Direktionalität und die geringe Modenüberlappung mit dem Glasfaserprofil die limitierenden Faktoren dar. Während die erste Begrenzung in dieser Arbeit durch einen metallischen Spiegel unterhalb des Gitters umgangen wird, wird der letzte Faktor durch Umgestaltung der einzelnen Gitterelemente optimiert. Die theoretischen Ergebnisse zeigen mögliche Effizienzen von über $-0,3$ dB mit einer 1 dB-Bandbreite von mehr als 40 nm.

Die entworfenen Gitterkoppler einschließlich der Metall-Spiegel wurden kostengünstig mittels konventioneller Technologie-Verfahren am IMS CHIPS gefertigt. Etwa 75% der hergestellten Strukturen auf dem Silizium-Wafer zeigen eine höhere Koppel-effizienz als $-0,75$ dB. Der beste Wert beträgt $-0,62$ dB bei einer Wellenlänge von 1531 nm. Dies entspricht der weltweit höchsten jemals gemessenen Effizienz. Darüber hinaus beträgt die 1 dB-Bandbreite 40 nm und übertrifft den vordefinierten Zielwert. Daher bietet diese Arbeit eine Lösung zum bekannten Einkopplungsproblem und schließt somit die Lücke zwischen Glasfasern und photonischen integrierten Schaltungen.

Abstract

The progress that photonic integration is undergoing may be compared to that of electronic integration nearly half a century ago. Its development will not only enable the transmission of huge amounts of information – particularly in optical data communication – but will also pave the way for large scale fabrication, the minimization of assembly processes, and the reduction in energy consumption. The benefits of photonic integration can even be increased by harnessing the salient properties of the silicon-on-insulator platform. In fact, silicon photonics can leverage the existing complementary metal-oxide-semiconductor infrastructure, and hence can offer a low-cost solution for the more and more complex sender and receiver architectures.

Another advantage of the silicon-on-insulator platform is the possibility for high-density integration owing to the offered large index contrast between silicon and silicon dioxide. This property certainly enables the realization of compact circuitries with numerous functionalities on very small areas; however, it also creates a barrier to the connection with available optical fibers. While the integrated waveguide structures on the chip have cross sections in the order of $0.1 \mu\text{m}^2$, external optical fiber cores possess dimensions of more than $50 \mu\text{m}^2$. This large mismatch can lead to extreme insertion losses, and hence the advantage of miniaturization turns into a problem of coupling with the existent conventional fibers.

At first view, the issue highlighted may be seen as trivial since several standard coupling techniques, such as tapered fibers or lensing systems, are available. Nevertheless, the stringent requirements for high efficiency, compact dimensions, and more flexible coupling in industrial applications indicate that better performing configurations have to be implemented. For this purpose, a variety of approaches starting from three-dimensional tapers to photonic crystals and plasmonic structures have been proposed. Each of these techniques, however, offers more cons than pros, and thus none of them have yet made the leap into practical application.

Within the scope of this thesis, two different coupling approaches are investigated. The first method deals with metamaterials, which allow for the realization of effects not seen in nature. The second method is based on more application-oriented structures, known as Bragg gratings. The common purpose of both topics is the concrete realization of highly efficient couplers that alleviate the size difference between conventional optical fibers and integrated single-mode silicon waveguides. As a benchmark, the coupling efficiency has to exceed the value of -1 dB, whereas the 1 dB bandwidth has to be larger than 35 nm in order to cover the whole C-band.

The investigation of focusing metamaterial structures is done first at millimeter wavelengths owing to the fabrication and characterization convenience. The main target of this approach is to create a negatively refracting material that can focus an input beam into a much smaller spot size at a short distance. Furthermore, the negative index metamaterial has to exhibit low reflection and absorption losses, and hence high transmissivity in a large frequency range. Thereafter, the dimensions of the focusing metamaterial lens are scaled down in order to analyze their applicability at telecommunication wavelengths.

The metamaterial functional layer is designed based on the dielectric-metallic fishnet structure and fabricated using conventional etching techniques. The designed metamaterial stack exhibits a high transmissivity of nearly -0.5 dB with a negative refractive index of -1 at the operating frequency 38.5 GHz and a 1 dB bandwidth of 0.8 GHz. The measurement results are shown to be in good agreement with the theoretical calculations. Thereafter, in order to achieve a focusing metamaterial lens, the shape of the stack is modified to form a plano-concave configuration. This structure shows good focusing ability with a reduction of the launched beam waist by a factor of 2.2 at a distance of only $6 \lambda_0$. In comparison, a fabricated aspheric dielectric lens exhibits twice the beam waist at a distance of more than $12 \lambda_0$. The negative index lens, therefore, is a good candidate to replace conventional lenses at radio frequencies owing to its better focusing performance and more compact dimensions.

Indeed, scaling the dimensions of the lens down to infrared wavelengths theoretically shows a similar behavior with a beam width reduction by a factor of 3.8 at a distance of $8.7 \lambda_0$, which is advantageous for nanocoupling between optical fibers and integrated

waveguides. However, the considerable metal losses decrease the total efficiency to lower than -2 dB. Hence, the target efficiency cannot be achieved, and alternative solutions have to be used in the future in order to compensate for these absorption losses at optical frequencies.

The second coupling method investigated in this thesis relies on Bragg diffraction gratings. In comparison to the first method, these structures have the advantage of being directly integrated with the waveguides on the chip, and thus they can be realized more cost-effectively. Moreover, this procedure allows out-of-plane coupling and wafer-scale testing without the need for edge cleaving and polishing. These advantages make grating couplers good candidates to compete with the in-plane coupling spot size converters, which require a much larger footprint, provided that the efficiency is enhanced to the same order of magnitude.

As the coupling efficiency of standard diffraction gratings is relatively low, the loss sources have to be analyzed, and possible improvement methods have to be implemented. In fact, there are two main factors that limit the performance of grating couplers: directionality and modal overlap with the fiber profile. In this work, the first issue is tackled using a metal mirror at an adequate distance underneath the grating; the second factor, meanwhile, is rigorously optimized by reshaping the diffracted field profile based on a home-made algorithm. The theoretical results show efficiencies better than -0.3 dB with a 1 dB bandwidth larger than 40 nm.

The designed grating couplers, including the metal mirrors, are fabricated cost-effectively using a complementary metal-oxide-semiconductor compatible technological process at IMS CHIPS. Placed at different positions on the wafer, around 75% of the fabricated structures exhibit a better coupling efficiency than -0.75 dB. The highest value reaches -0.62 dB at 1531 nm, which is, to the best of knowledge, the highest measured efficiency on a grating coupler reported so far. Furthermore, the achieved 1 dB bandwidth amounts to 40 nm and exceeds the predefined target value. This work, therefore, can be seen as a milestone in the field of silicon photonics and a bridging gap between optical fibers and photonic integrated circuits.

1. Introduction

1.1. Motivation

As the need for higher data rates is rising more and more, the demand for high bandwidth communication increases at all levels. This is largely being driven by the considerable growth in internet traffic, which has risen with increasing numbers of users, connected devices, and bandwidth-hungry applications such as high-definition internet video and file sharing.

In a study published by Cisco in [1], annual global internet traffic will reach 1.4 zettabytes by 2017, which represents a threefold increase compared to 2012. In order to manage the tremendous amount of data in this so-called “zettabyte era”, the existing telecommunication network has to be adapted to meet exploding bandwidth demand. Indeed, the optical fiber backbone represents a sustainable and expandable infrastructure, which allows the transmission of several terabits per second owing to the high capacity of optical fibers, but more developments have also to be achieved on the sender and receiver sides.

Awarding the Nobel Prize in Physics 2009 to Charles Kao for his seminal achievements in the transmission of light in fibers proves the importance of optical communication in today’s life [2]. In fact, optical fibers have enabled the transfer of very high data rates over long distances, which cannot be realized using electrical cables. In addition to small signal attenuation at high frequencies, fibers exhibit a huge bandwidth and immunity to electromagnetic interference.

Due to the advantages offered by optical links, today’s long haul and metropolitan communications are based on fiber networks covering several thousands of kilometers, connecting a great many countries and cities. The trend is further approaching individual users, making benefit of emerging technologies such as fiber-to-the-home (FTTH) and fiber-to-the-building (FTTB) with data rates even higher than 1 Gbit/s [3]. Besides long and medium distance links, short reach optical interconnects are progressively

gaining more interest and are considered the best candidate to replace electrical copper cables at high data rates in the near future. This includes network traffic in data centers down to backplanes, chip-to-chip, and on-chip communication links.

It has recently been demonstrated that nearly 100 Tbit/s can be transmitted on a single-core fiber [4], whereas more than 1 Pbit/s are able to be transmitted on a multi-core fiber [5]. These record data rates have been realized using a combination of various techniques such as wavelength division multiplexing (WDM), polarization multiplexing, and high-order modulation formats. Therefore, higher data rates require more complex senders and receivers with numerous processing methods and a large variety of optoelectronic components, which also increase the expense of the optical communication links. Moreover, the extensive assembling of the different components augments the overall costs and represents a major obstacle for this emerging technology.

Meanwhile, the integration of optical devices on chips has offered a significant progress to realize compact and more cost-effective high-speed optical interconnects. For this purpose, several approaches have been proposed based on different semiconductor platforms such as the silicon-on-insulator (SOI), the indium phosphide (InP), and hybrid integration technologies. Since each solution has its own advantages and drawbacks, however, it is difficult to find a universal approach that provides all components with the properties required.

Indeed, the SOI platform has gained more interest during the last years owing to its compatibility with existing electronic system architectures realized on silicon (Si) substrates and the maturity of the complementary metal-oxide-semiconductor (CMOS) fabrication process, which represents an important solution to maintain low-cost production of photonic components. Si, furthermore, is transparent at telecommunication wavelengths 1310 nm and 1550 nm, and hence offers the possibility of optical waveguiding in analogy to the electric wires in electronic circuits. Silicon photonics is also known for high refractive index contrast, which enables high-density integration owing to the strong light confinement, and thus more compactness of the puzzle elements for optical data processing. Over the last decade, substantial progress has been made in realizing high-performance components in silicon photonics: from passive waveguiding structures to active devices such as photodetectors, modulators, and recently lasers.

Nevertheless, this technology still encounters many obstacles that must be solved soon in order to accelerate photonic integration and control the fast increase in data and energy consumption. While the proposed monolithic germanium-on-silicon laser in [6] exhibits an extremely high threshold current density and a low output power efficiency to be used in real applications, the coupling issue between integrated nanophotonic waveguides and standard optical fibers restricts the Si chips to communicating with the “outside world”. For short and middle term, the hybrid integration of III/V semiconductor light sources with the existing Si platform may be the most adequate solution for the former problem. The latter issue, by contrast, has to be addressed fundamentally to bridge the gap between standard optical fibers and photonic integrated circuits (PICs).

In fact, as the large refractive index difference of the SOI platform offers the advantage of high-density integration and compact dimensions in the order of submicrometer, it simultaneously involves the challenge of coupling light from existing optical cables to integrated waveguides, and vice versa. Figure 1.1 shows the size comparison between a single-mode integrated waveguide in SOI and the core of a single-mode fiber (SMF).

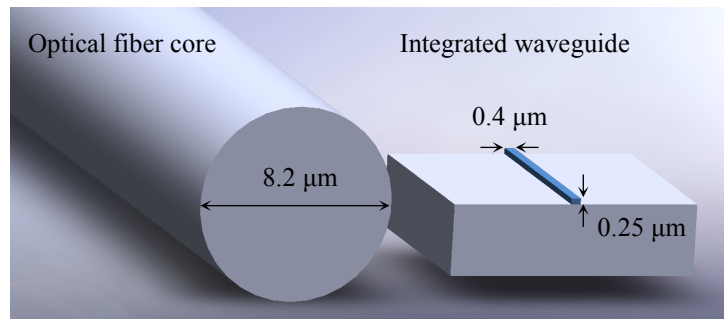


Figure 1.1: Graphical representation of the dimensional difference between a single-mode fiber core and an integrated waveguide in the SOI platform.

A typical integrated waveguide has a width of $0.4\ \mu\text{m}$ and a height of $0.25\ \mu\text{m}$, whereas a standard SMF has a core diameter of $8.2\ \mu\text{m}$ and a mode field diameter (MFD) of $10.4\ \mu\text{m}$ at the wavelength $1550\ \text{nm}$ [7]. As the cross section of the waveguide is in the order of $\sim 10^{-3}$ smaller than that of the fiber core, considerable coupling losses govern the fiber-to-waveguide transition when using the butt coupling technique, i.e. when both components are butted up against one other, and efficiencies in the order of only 0.1%

can be achieved. Hence, there is a need of coupling elements that can relax the abrupt transition and increase the coupling efficiency between PICs and optical fibers.

1.2. State-of-the-art fiber-to-chip couplers

There exists a variety of concepts for better fiber-to-chip coupling efficiency than using the butt coupling method. All approaches rely on mode conversion between both waveguides using a so-called nanocoupler. In other words, this element is nothing else than an optical funnel, which concentrates light from a large to a smaller section with dimensions in the nanometer range [8]. The nanocoupler can be fabricated on the fiber, used as a stand-alone device, or integrated on the chip. Figure 1.2 shows a graphical representation of the three possible categories.

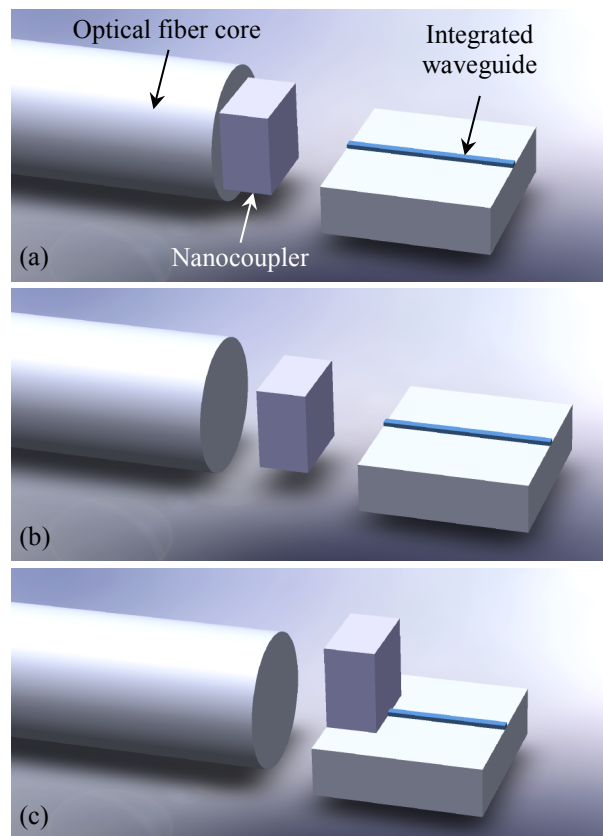


Figure 1.2: Schematic illustration of the possible fiber-to-chip coupling techniques using (a) on-fiber, (b) stand-alone, and (c) on-chip nanocouplers [8].

The on-fiber technique requires modifying the optical fiber end-face and saves the need for designing additional coupling structures on the chip itself. The best-known approaches rely on tapered or lensed fibers, which can focus light into very small spots, and hence decrease the large mode mismatch. When reducing the MFD of the fiber to $3\ \mu\text{m}$, the coupling efficiency to a single-mode nanowaveguide can be improved to around 2%. This technique can be advantageous in terms of space-saving on the chip, but the waveguides also have to be adapted beforehand to the lateral coupling by cleaving and polishing the end-face of the chip. In addition, the coupling efficiency is too low to use such fibers in practical products, and standard fibers are preferred to these costly solutions since they are commonly used in commercial applications.

In order to make use of the standard SMFs and with no special coupling structures on the chip, an appropriate solution would be the utilization of a stand-alone device that collects light based on a lensing system. Indeed, conventional dielectric lenses are known to focus electromagnetic waves and have been implemented for a long time in a countless number of optical applications; however, their diffraction-limited resolution may restrict their ability to act as nanocouplers. A more attractive procedure is based on negative index metamaterial (NIM) lenses, which are theoretically not diffraction-limited and can exhibit arbitrary internal properties, offering the possibility to mold the flow of light in a flexible fashion. Since NIMs include metallic structures, they feature significant losses at optical frequencies, and hence need to be optimized to compete with their positive index dielectric counterparts. Some other lensing methods can also be used such as photonic crystals or hyperlenses, but they present considerable losses as well.

The third possibility relies on the integration of the coupling structures directly on the chip. This approach may be the most adequate solution since it is generally compatible with standard fibers and does not require extensive alignment steps unlike the lensing devices. Here there is also a variety of possible implementations, but they can be classified into two main groups depending on the fiber orientation: in-plane and out-of-plane coupling. While the former technique is based on horizontal spot size converters (SSCs), where the fiber is positioned in the chip plane, the latter method rests on coupling light from a different direction than that of the waveguide such as using nanoan-

tennas or diffractive Bragg gratings. Hence, the SSCs need a length of several hundreds of micrometers to transform the fiber mode into the waveguide mode, whereas the Bragg gratings for example have dimensions as small as the fiber core. When combined with tapered fibers, the length of SSCs can be further reduced, and an efficiency of more than 90% with a 1 dB bandwidth larger than 100 nm can be achieved [9], [10], far exceeding the performance of grating couplers.

Among all approaches mentioned above, coupling based on Bragg gratings has been successfully established over the last years owing to the many advantages offered. Being much more compact than integrated SSCs, these structures can couple light directly from standard fibers without the need for additional tapering processes. In addition, they are fabricated cost-effectively due to the few required etching steps and can be placed at an arbitrary position on the chip without edge cleaving. Thus, this procedure has allowed wafer-scale testing possibilities, facilitated research investigations on new integrated components, and has recently enabled silicon photonics to gain access to commercial products [11]. Indeed, the efficiency and bandwidth achieved through experiments are still suboptimal, but grating couplers have the potential to replace the edge-coupling methods owing to their numerous advantages, auspicious theoretical predictions, and fast-achieved progress.

Table 1.1 summarizes the performance of some state-of-the-art integrated nanocouplers based on grating couplers with respect to their measured coupling efficiency and bandwidth. It can be seen that the achieved efficiencies are approaching the values realized by tapered spot size converters, i.e. nearly 90%, and hence they can be real candidates in commercial products based on integrated nanophotonics.

Table 1.1: State-of-the-art integrated grating couplers based on their measured efficiency and bandwidth.

Reference	Institution	Year	Coupling efficiency	1 dB bandwidth
[12]	IMEC	2010	69%	44 nm
[13]	CUHK	2011	76%	27 nm
[14]	Luxtera	2012	84%	29 nm
This work	INT	2013	87%	40 nm

All structures in Table 1.1 are realized in a CMOS-compatible SOI platform and serve to couple light from standard fibers to integrated Si nanowaveguides at wavelengths around 1550 nm. The coupler reported in [12] consists of a periodic grating and a Si overlay to inherently enhance the directionality of the diffracted field. This certainly yields an improved efficiency compared to standard structures, but losses are still present due to the mode mismatch between the fiber and the diffracted field. The latter problem is tackled in [13] and [14] by using a nonuniform grating that mimics the fiber Gaussian profile, and therefore increases the efficiency further.

In this thesis, it is demonstrated that the efficiency and the bandwidth can theoretically be improved using a backside metal mirror and an adequate nonuniform grating. Both methods are also proven experimentally to enhance the overall performance of grating couplers.

1.3. Objective and outline of the thesis

This thesis addresses the coupling issue between optical fibers and integrated nanowaveguides due to the large size difference and mode mismatch. For this purpose, a coupling structure is needed to alleviate the abrupt transition and increase the efficiency between both waveguiding elements. To tackle this problem, there are several approaches that can be applied whether on the fiber, as a stand-alone device, or directly on the chip. While there already exist well-known solutions based on tapered structures and dielectric lensing systems, new more powerful tools are emerging for better manipulation of light such as metamaterials and transformation optics [15]. Thanks to the progress of the fabrication procedures as well, even some old techniques such as diffractive gratings are being reinvented.

The first objective of the thesis is to investigate the feasibility of highly transmissive lenses based on NIMs and their ability to act as nanocouplers for telecommunication applications. Investigations are done primarily at radio frequencies due to the ease of fabrication and handling of the structures in the millimeter scale. Thereafter, an analogy is drawn at optical frequencies, and the limitation factors are presented.

The second objective is to develop the nanocoupler directly at telecommunication wavelengths. The challenge here is that the dimensions are in the micrometer scale, and a more sophisticated fabrication process is required. However, a better estimation of the coupling properties can be achieved, and the solution can be directly applied in integrated optical systems. Owing to the many advantages offered by grating couplers, these structures are investigated with the target of achieving an efficiency of 80% with a 1 dB bandwidth larger than 35 nm. The thesis comprises six chapters, including a description of the problem, together with theoretical and experimental investigations of the solutions discussed, and is organized as follows:

Chapter 2 addresses the coupling issue. The different concepts based on the on-fiber, stand-alone, and on-chip nanocouplers are considered in more detail. A short glimpse into nanophotonics technology is also given.

Chapter 3 introduces the fundamentals of optical data transmission. Here the main components in optical transmission systems are discussed, and the importance of optical waveguiding is emphasized. Besides this, the theory behind electromagnetic wave propagation and the waveguiding effect is explained.

Chapter 4 deals with the coupling approach based on NIMs. First, the theoretical background of such artificial materials and their advantages in lensing and nanocoupling applications are shown. Thereafter, a novel metamaterial design is proposed and its internal properties and lensing ability are experimentally investigated at millimeter waves. The parameters of the unit cell are also scaled down to the nanometer range, and the behavior is theoretically analyzed at infrared wavelengths.

Chapter 5 investigates structures based on diffraction gratings for direct light coupling from the optical fiber to integrated waveguides. After introducing the theoretical fundamentals of Bragg gratings, the optimization procedures of the structures are described in detail. Afterwards, the fabrication process and the experimental results are conducted and explained.

The results are summarized in Chapter 6, and a conclusion on the advantages and drawbacks of the applied approaches is given. Finally, a short outlook for potential future works is provided.

2. Coupling issue between optical fibers and PICs

In this chapter, a short insight into the field of nanophotonics and its importance in future optical data processing systems is given. Some examples of integrated components are also presented, and the coupling issue to optical fibers originating from the large dimension mismatch is emphasized. In addition to this, possible solutions based on different techniques are described in detail, and the corresponding advantages and drawbacks are pointed out.

2.1. Nanophotonics technology

Owing to the promising properties of optical links, which may solve the bandwidth bottleneck in long, medium, and short reach interconnects, important progress has been achieved in the field of integrated photonics. In fact, the integration of optical devices is a means to maintaining low-cost manufacturing, high bandwidth density, and low energy consumption. The SOI platform has also enabled the realization of very compact photonic circuits due to the large refractive index contrast offered. It has as such given rise to so-called nanophotonics technology.

Based on silicon nanophotonics, a very large bandwidth density of 30 Tbps/cm² on a single substrate for high bit rate inter-chip interconnects has recently been demonstrated [16]. This record density has been enabled by the small footprint of the required optical components and the high-speed of the electro-optical (EO) and opto-electrical (OE) converters. The realized interposer consists of waveguides, modulators, and germanium photodetectors, which are directly integrated in Si, whereas the III/V semiconductor lasers are hybridly integrated onto the chip and connected to the waveguides using SSCs. This shows the benefits of nanophotonics, which offers the possibility of integrating multiple functionalities on very small areas.

In general, the field of nanophotonics describes the manipulation of light based on components with dimensions in the nanometer scale. The main element of this technology is

the nanowaveguide, which may have a cross section in the subwavelength range and serves to guide the electromagnetic waves through the photonic circuits in analogy to the electric wire in electronic circuits. There exist several topologies of the waveguide such as the planar, the strip, the ridge, and the bandgap structure. The theory behind the waveguiding effect and some implementations of the waveguide are discussed in detail in the next chapter.

Since many modes are able to propagate in the photonic wire, which may cause signal dispersion, and so may limit transmitted data rate, it is reasonable to adjust the waveguide dimensions to carry only one mode. The cross section, therefore, is generally reduced to transmit solely the fundamental wave, and the waveguide is called single-mode. Figure 2.1 shows some examples of integrated components based on single-mode nanowaveguides.

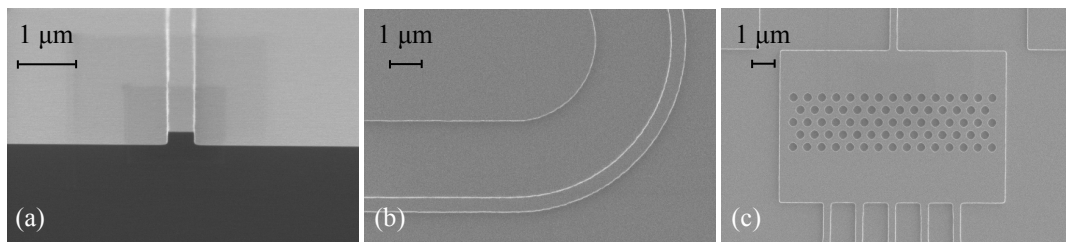


Figure 2.1: Scanning electron microscope (SEM) pictures of some integrated components in SOI: (a) A single-mode straight waveguide, (b) a single-mode bended waveguide, and (c) a photonic crystal with single-mode input and output waveguides.

In order to couple light from the optical fiber to the small cross section of the waveguides, the most axiomatic method rests on positioning the fiber core at the end-face of the integrated wire. This procedure, called butt coupling, nevertheless allows for a transmission of only 0.1% from the input fiber to the chip due to the losses caused by the large size mismatch. In addition, the integrated components commonly exhibit additional insertion losses, and hence the signal received at the OE converter on the chip or the retransmitted light from the chip to the output fiber may be extremely small and unquantifiable. To tackle this problem, there is a variety of concepts, which, as discussed in the previous chapter, can generally be classified into three categories.

2.2. Coupling concepts

2.2.1. On-fiber nanocouplers

The first category is based on on-fiber nanocouplers where the fiber tip is modified to refine the abrupt transition between the core and the integrated waveguide. Figure 2.2 shows some examples of this coupling method, which can in turn be classified into in-plane, such as in Figures 2.2(a) and 2.2(b), and out-of-plane, such as in Figure 2.2(c), depending on the fiber orientation.

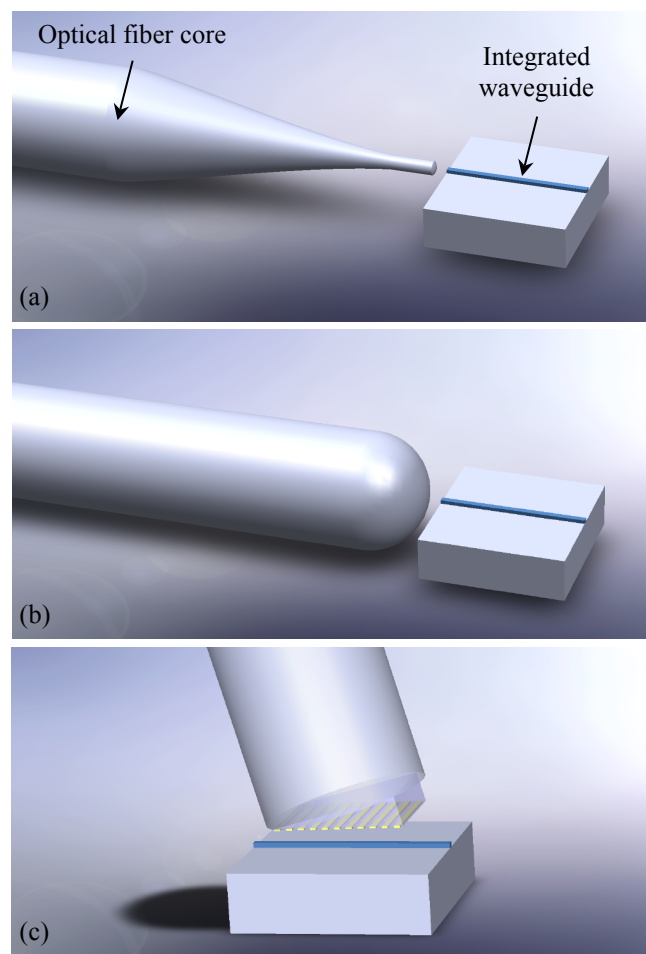


Figure 2.2: Schematic representation of different on-fiber coupling techniques using (a) a tapered fiber, (b) a lensed fiber, and (c) a grating on the fiber end-face. Only the core of the fiber is illustrated in the graphs.

While tapering the tip is achieved by heating and stretching a long section of the fiber, the lensed structure is realized by shaping only the end-face. In general, thinning the

fiber down to the waveguide dimensions does not solve the problem since light can no longer be confined inside the fiber core and is predominantly located at the fiber-air interface due to the low refractive index contrast between core and cladding [17]. The propagating mode, therefore, cannot easily be matched to the waveguide profile, and efficient coupling cannot be guaranteed. The second on-fiber coupling method relies on focusing the light into the waveguide using a microlens structure. Conventional lensed fibers possess a convex end-face, which contracts the MFD of the emitted beam to around 3 μm at a wavelength of 1550 nm [18]. The MFD can be further reduced to 1.2 μm when using high-index-layer coatings for example [18], [19], which may increase the coupling efficiency to the integrated single-mode waveguides to nearly 30%. Theoretically, a more than 90% efficiency is achievable when the MFD of the focused beam is reduced to 0.5 μm , which corresponds roughly to the dimensions of the waveguide cross section. Dielectric lenses, however, are not able to focus light into such a tight spot at the operating wavelength due to their diffraction-limited property.

Both in-plane configurations require additional cleaving and edge polishing of the chips to ensure lateral coupling. Moreover, adjusting the position of the tapered fiber in front of the waveguide may be challenging, whereas most lensed fibers need a certain working distance to be able to focus the beam into the waveguide, which may also introduce some alignment difficulties. Alternatively, instead of changing the shape of the fiber tip, a diffraction grating can be defined on the end-face, which permits vertical coupling, and hence wafer-scale testing [20]. This method can be advantageous as well when probing of the optical signal on the chip is required.

There also exists a number of other approaches, which are more sophisticated than the presented coupling techniques and are mainly based on plasmonic effects [21]-[23]. Indeed, oscillations of the metal electron plasma produced by the incident electromagnetic waves, which are known as surface plasmon polaritons (SPPs), can be generated at the interface between a thin metallic layer and the end-face of an optical fiber and enhance the light confinement to dimensions well below the diffraction limit. However, the high losses of metals at optical frequencies may prevent the suitability of such concepts in today's applications.

2.2.2. Stand-alone nanocouplers

The second category of nanocouplers relies on stand-alone devices, which allow the use of standard commercial fibers without the need for additional end-face forming as can be seen in Figure 2.3.

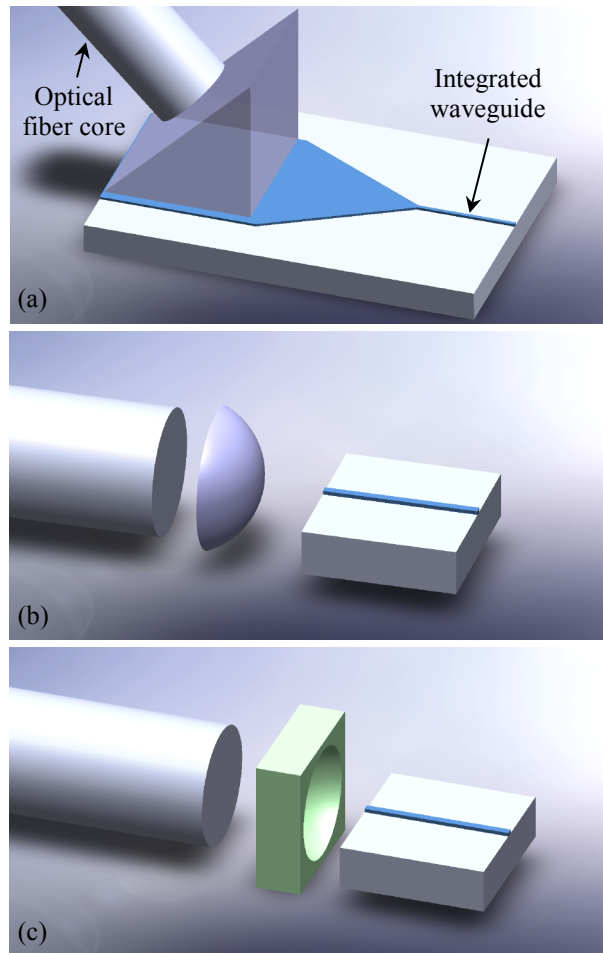


Figure 2.3: Schematic drawing of different stand-alone fiber-to-chip coupling devices based on (a) a prism coupler, (b) a plano-convex dielectric lens, and (c) a plano-concave NIM lens.

One of the well-known techniques makes use of prism couplers [24] that can be placed on top of the integrated waveguide and saves edge cleaving. However, the prism has to be made by a material with a higher refractive index than the waveguide, which can be challenging for SOI structures due to the high refractive index of Si. Besides, such a construction may damage the thin structures since it has to be placed in the immediate

vicinity of the film layer to ensure evanescent wave coupling [25], and additional tapering to the waveguide is also required.

Another more established method is based on dielectric lenses, which can also be used as stand-alone devices instead of being defined on the end-face of the fiber as described in the last subsection. These devices are applied in a large number of optical systems with different functionalities such as focusing, collimating, and magnifying the electromagnetic waves. They can mainly be classified into spherical, diffractive, and gradient index (GRIN) lenses [26]. In integrated optics, microball lenses are commonly utilized to couple light from the chip into the fiber, which can be mounted in a so-called V-groove to guarantee a good alignment [27]. However, focusing light from the fiber to the tiny waveguides may be challenging due to the diffraction-limited spot size. It should also be noted that focusing light into a small cross section is not enough to achieve a high coupling efficiency since matching to the waveguide mode profile must also be realized.

Over the last decade, other types of lenses, called superlenses – made by artificially engineered negative index materials – have aroused more interest owing to their superior capability of imaging objects well below the diffraction limit [28]. These flat lenses produce an amplification of the evanescent waves, which contain the superfine details of an object, and hence enable subwavelength resolution in the near field regime. Indeed, focusing a large beam into a smaller section cannot be realized using flat NIMs, but by using a plano-concave configuration, the incoming light can be concentrated in the far field, unlike positive index lenses, which focus light based on convex shapes. In addition to a larger numerical aperture than ordinary spherical lenses, these structures exhibit less aberration, stronger focusing ability, and especially a shorter focal length [29], [30]. Furthermore, the internal electromagnetic parameters can be freely adjusted to attain any positive or negative values, which may be favorable for perfect matching to free space, and consequently low reflections.

As focusing plano-concave NIM lenses cannot afford resolutions below the diffraction limit in the far field regime, some other kinds of constructions based on hyperlenses and metalenses have been proposed and have shown evidence of deep subwavelength focusing ability [31], [32], but again with low transmission characteristics.

2.2.3. On-chip nanocouplers

The third category deals with on-chip couplers, which are directly fabricated with the integrated waveguides as can be seen in Figure 2.4. Some of the lensing systems discussed can be implemented on the chip [33], [34], but the use of extensive nonstandard fabrication procedures may prohibit their introduction into commercial products.

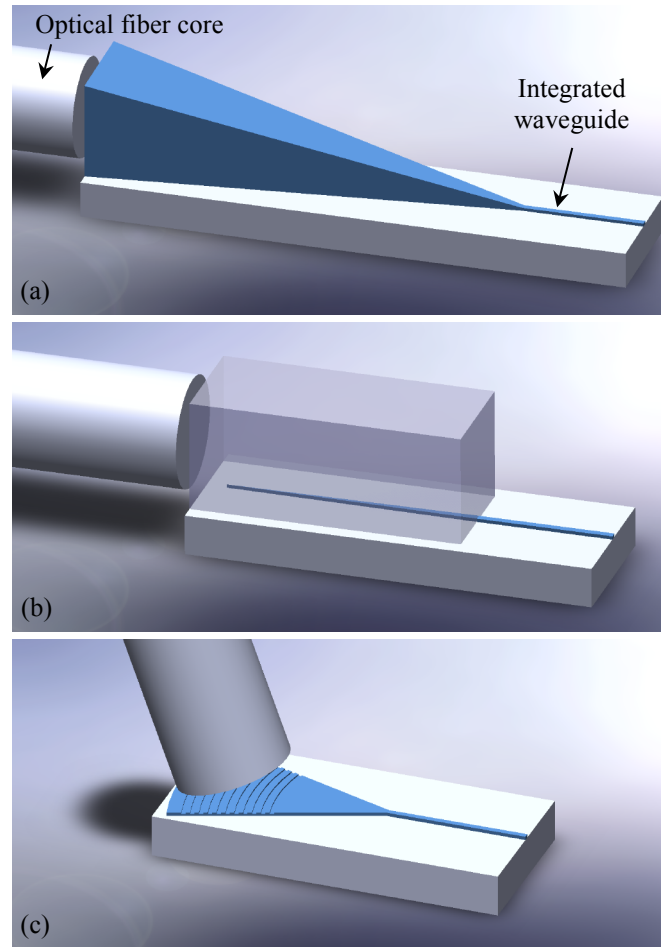


Figure 2.4: Different types of on-chip nanocouplers using (a) a three-dimensional (3D) taper, (b) an inverted taper, and (c) a diffractive grating.

Both integrated SSCs based on the 3D taper and the inverted taper are typically utilized to adiabatically adapt the fiber beam profile to the waveguide mode, and hence have a length of several hundred micrometers. These structures exhibit high coupling efficiency and low polarization dependence, but require disadvantageous edge coupling and are often used with tapered or lensed fibers to decrease the spot size of the incoming beam

and the overall length on the chip [9], [35]. Additionally, the inverted taper SSC needs a very narrow tip smaller than 50 nm to fully expand the optical mode outside the Si waveguide, which might be a technological challenge.

A more elegant solution, based on grating couplers, may provide more advantages than the latter approach since they are very compact in size and require less fabrication effort. These diffractive gratings offer the possibility to change the direction of the incoming light from a vertically aligned fiber to a laterally lying waveguide, or vice versa. By integrating the element on the chip, costly shaping of the fiber end-face is saved and standard SMFs can be used to carry out wafer-scale measurements instead of complicated butt coupling. Moreover, grating couplers can be designed to realize a variety of different functionalities and work for example as polarization beam splitters (PBSs) [36], power splitters or combiners [37], and wavelength demultiplexers [38]. Using an array of grating elements, coupling of the signal from several channels based on the recently developed space division multiplexing (SDM) scheme can also be achieved.

The simplest way to fabricate such couplers is by etching a linear grating in the film layer that fulfills the Bragg condition at the corresponding operating wavelength. The area of the structure should also be similar to the fiber core dimensions to couple most of the incident light, and thus the grating width has to be tapered over several hundreds of micrometers down to the single-mode waveguide width. This may be overcome by means of focusing arrangements to decrease the overall length to just a few micrometers [39]. Finally, despite the multiple benefits offered by this coupling technique, there are several loss mechanisms available in the grating structures, which have to be surmounted to make them compete with the highly efficient SSCs.

Some other integrated on-chip solutions based for example on plasmonic nanoantennas have also been proposed in order to tackle the coupling issue [8] but with more drawbacks than advantages. Indeed, nanoantennas and nanoparticles have very compact dimensions, much lower than all other presented configurations, and have shown remarkable field intensity enhancement owing to the resonant plasmonic behavior in several applications such as lasers [40] and photodiodes [41]. However, in the case of coupling between standard optical fibers and integrated dielectric waveguides, the theoretical

coupling efficiency of such nanoantennas is limited to only 50% [42] in addition to considerable conversion losses between the plasmonic and photonic modes.

2.3. Conclusion

It is clear that there exists a number of possible coupling concepts and not all of them may satisfy stringent industrial requirements. There is certainly an urgent need for nanophotonics in commercial products to appease the present bandwidth explosion, and thus cost-effective, high-efficiency, and reliable components are of most importance to make nanophotonics accessible for end-user products. Some of the proposed methods, therefore, may not qualify for large scale fabrication but may exhibit interesting phenomena that can be used in other applications.

Table 2.1 summarizes the advantages and disadvantages of some of the fiber-to-chip coupling techniques discussed with respect to their efficiency, bandwidth, compactness, possibility for wafer-scale coupling, and cost-effectiveness.

Table 2.1: Comparison of different coupling concepts. The “+” and “-” signs denote favorable and unfavorable respectively.

Concept	Efficiency	Bandwidth	Compactness	Wafer-scale	Cost
Tapered fiber	-	+	-	-	+
Lensed fiber	-	+	+	-	-
On-fiber grating	-	-	+	+	-
Prism coupler	+	-	-	+	+
Dielectric lens	+	+	-	-	+
NIM lens	-	-	+	-	-
3D taper	+	+	-	-	-
Inverted taper	+	+	-	-	-
Grating coupler	-	-	+	+	+

At first glance, the NIM lens may be the least advantageous for fiber-to-chip coupling due to the high losses in such kind of materials, the small bandwidth imposed by the resonant behavior, and the challenging fabrication. On the other hand, NIMs offer more degrees of freedom than conventional lenses and exhibit unprecedented properties, which enable molding the flow of light in a flexible way. Hence, several optimizations

have to be achieved to enhance their performance, and the focusing ability for possible fiber-to-chip nanocoupling is investigated in the fourth chapter.

Conversely, grating couplers show the most advantages among all coupling techniques, except for the efficiency and bandwidth that have to be improved to make them compete with integrated SSCs. This method, therefore, is investigated in the fifth chapter, and the origin of the loss factors is analyzed and tackled by adequate optimization of the grating parameters.

3. Fundamentals of optical data transmission

This chapter deals with the properties, components, and operating mode of optical transmission systems. A particular focus on the integrated components, and especially on the main element of the photonics technology, the nanowaveguide, is given. The theoretical background behind the electromagnetic wave propagation in waveguiding structures is presented, and the coupling issue to optical fibers is emphasized again. A short insight into the theory of the electromagnetic wave propagation in periodic media is also provided in order to pave the way for the selected topics in this thesis, which both rely on periodic arrangements for nanocoupling purposes.

3.1. Components of optical transmission systems

In general, the optical transmission architecture in its simplest form consists of a sender, an optical link, and a receiver as can be seen in Figure 3.1(a). As telecommunication data in today's systems are mainly generated by electronic integrated circuits (ICs), EO components are needed to convert the electrical signal into an optical one. Depending on the required bit rate of the information to be sent, the complexity of the transmitter and the modulation format used may vary from one system to another. Hence, additional components may be implemented on the PIC to process the optical signal.

Afterwards, the signal is carried by an optical link over a distance that can range from a few centimeters to thousands of kilometers according to the application reach. For this purpose, the optical fiber has been proven to be the best host owing to its large bandwidth and low attenuation and can be used in all applications, starting from short reach interconnects up to long haul networks. Indeed, costly optical amplifiers have to be used for long distances, whereas additional dispersion effects must also be electronically compensated to recover the transmitted information. As yet, no better medium has been developed to replace the optical fiber.

Finally, at the receiver, the signal is demodulated and converted back into an electrical signal. It should be noted that the complexity of the ICs increases with the complexity of the modulation format used and the required speed as well, especially the digital-to-analog converters (DACs) at the sender side and the analog-to-digital converters (ADCs) at the receiver side.

When the transmitter and the receiver are implemented together on one platform, as shown in Figure 3.1(b), the system is called a transceiver. This architecture exhibits two functionalities at the same time and serves to convert the incoming electrical signal into an optical one, or vice versa. A predominant application based on this approach is the active optical cable (AOC), which permits the transmission of very high data rates that cannot be bridged by copper wires [43].

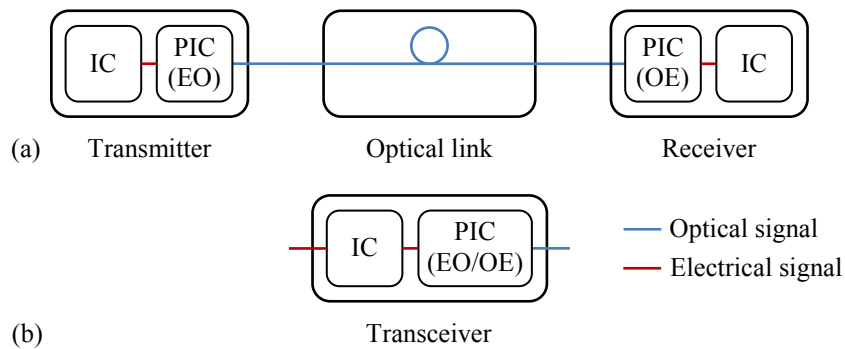


Figure 3.1: Schematic illustration of an optical transmission system based on (a) a separated transmitter and receiver connected by an optical link, and (b) a transceiver.

3.1.1. Transmitter concepts

The actual optical fiber telecommunication network relies mainly on the transmission of digital data owing to the innumerable advantages of digital storage, processing, and computing in addition to the exceeding performance in comparison with analog systems [44]. However, the transmission of this digital data on an optical fiber necessitates complex treatment and conversion. This is typically done through modulation of a light source driven by the electrical signal so that the transmitted optical signal can carry the information on the fiber.

The first step of this process is realized on the IC and consists of encoding the data, converting the digital signal into an analog one, and feeding the modulator driver. Thereafter, the light source is modulated, and then the optical signal can be further processed on the PIC depending on the used modulation format. While light emitting diodes (LEDs) can be used as optical continuous wave (CW) sources, laser diodes (LDs) are more preferable since they exhibit much narrower spectral widths, and hence a higher bandwidth-length product is realized [44]. The modulation procedure also plays a major role in the achievable bit rate and can be done internally by changing the injected current of the laser, which may be limited due to the detrimental chirp effect [45], or externally by using a Mach-Zehnder modulator (MZM) for example.

There is a variety of modulation schemes that can be applied depending on the required data rate and transmission distance such as amplitude shift keying (ASK) and phase shift keying (PSK) [46]. The constellation diagrams of some of these modulation formats are shown in Figure 3.2.

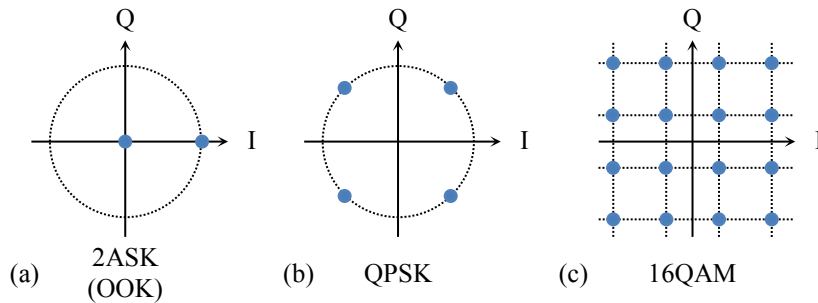


Figure 3.2: Signal space of different modulation formats based on (a) 2ASK (OOK), (b) QPSK, and (c) 16QAM.

The simplest method consists of modulating the amplitude between two states, “0” and “1”, which is a special case of the ASK and is also called on-off-keying (OOK). However, nonlinearity effects in the fiber may influence overall behavior due to the permanent on and off switching of the optical signal [44], which may be eliminated by keeping a constant power level and modulating the phase based on the PSK approach. In this case, in-phase (I) and quadrature (Q) carrier signals are needed to send symbols with the same amplitude and different phase states.

Higher-order modulation formats, such as quadrature phase shift keying (QPSK), are also widely applied owing to the high spectral efficiency offered. However, when using more phase levels, for example in the case of 16PSK, the distance between the different symbols is reduced and the bit error rate can deteriorate. A combination of both schemes, therefore, to a quadrature amplitude modulation (QAM) is reasonable [46].

To further increase the bit rate over a single channel, several multiplexing techniques based on different approaches can be applied. While the polarization division multiplexing (PDM) relies on the fact that both orthogonal polarization states propagate independently from each other in the fiber, WDM makes use of the different optical carriers that can be sent in a single band at a certain spacing. Recently, SDM has also enabled the transmission of very high data rates exceeding 1 Pbit/s by increasing the number of cores of a single fiber [5].

Obviously, these techniques require more optical components on the transmitter side such as polarization rotators and combiners for PDM and several laser sources and wavelength filters for WDM. Distributed feedback (DFB) lasers based on III/V semiconductors are commonly used to generate optical signals in the C- and L-bands at a very tight spacing of 0.4 nm and lower [47], but they have to be hybridly integrated on the SOI chip so long as no high-performance solutions for directly integrated lasers on Si are available. In addition, to generate the different phase states when using the high-order modulation formats, multiple MZM structures and phase shifters have to be implemented.

Figure 3.3 shows an example of an integrated dual-polarization (DP) QPSK transmitter PIC in the SOI platform. This modulation principle is used particularly in 100 Gbit/s Ethernet networks [48]. The transmitter PIC consists of a laser source coupled to the single-mode waveguide on the SOI chip by a nanocoupler that can be a lens, an SSC, or a grating as described in the previous chapter. Afterwards, the light is split equally by a multimode interferometer (MMI) to two branches [49] since two orthogonal polarizations have to be sent. In each branch, the “I” component is generated by an MZM structure, whereas the “Q” carrier signal needs an additional 90° phase shifter. Both components are then combined, and the signal of one branch is rotated to the orthogonal polarization plane. Finally, the light is coupled out to the optical fiber. It should be noted that

the illustrated two-dimensional (2D) grating works as a rotator, power combiner, and output coupler at the same time [50]. All represented structures can be realized following different approaches depending on the efficiency, footprint, and the technological process used, showing the high degree of freedom of the photonic integration.

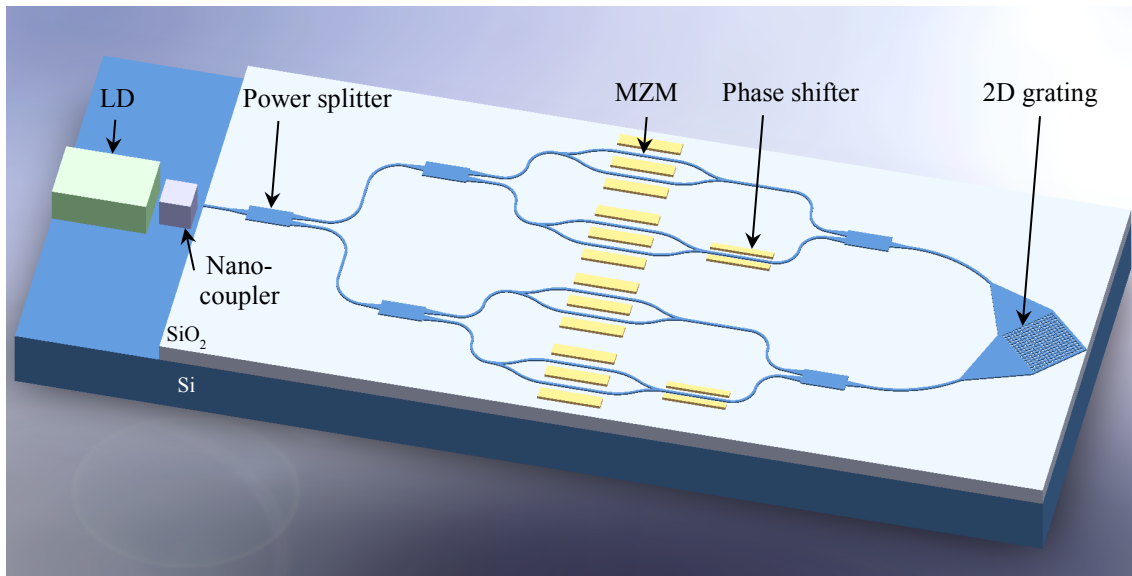


Figure 3.3: Graphical representation of a possible transmitter PIC in the SOI platform based on the DP QPSK modulation technique.

It is clear that high data rates necessitate a large number of integrated components, which augments the complexity of the transmitter PIC, and hence there is a trade-off between the required performance and fabrication costs. To follow the increasing bandwidth demand, there is a need for even higher data rates, and next generation networks beyond 100 Gbit/s have to be planned. This can theoretically be done by increasing the symbol rate, the modulation order, or the number of wavelength carriers [51]. While the first approach demands much higher bandwidth electronics and EO/OE converters, the second proposition requires an increased optical signal-to-noise ratio (OSNR), causing a reduction of the reach distance, and the third solution augments the PIC complexity. Therefore, customization of the telecommunication system in the future has to be done based on more adaptable concepts such as elastic optical networks (EONs), where the symbol rate, modulation format, and number of carriers are adjusted to bandwidth need in a flexible way [51].

3.1.2. Optical links

In an optical communication system, senders and receivers are connected to each other by an optical link that guides the transmitted light signal over a given distance. Fibers have been proven to exhibit excellent performance in terms of low loss and high bandwidth at optical frequencies and are indispensable in today's telecommunication network architectures.

Optical fibers are fabricated from silicon dioxide (SiO_2) with a lightly doped core using germanium dioxide (GeO_2) for example [52]. This configuration gives a core with a higher refractive index than the cladding, which is an essential condition for the waveguiding effect. The most important characteristic of fibers is the low attenuation at infrared wavelengths. Indeed, several loss factors caused by Rayleigh scattering and infrared absorption are present in this range, but a minimum attenuation loss takes place at a wavelength of 1550 nm and reaches a value of nearly 0.2 dB/km [52]. Therefore, in optical telecommunication networks, signals are commonly transmitted in the window around this wavelength, which is mainly divided in the S-band (1460 nm – 1530 nm), the C-band (1530 nm – 1565 nm), and the L-band (1565 nm – 1625 nm) [53].

Depending on the core dimensions, the fiber can guide one mode and is called SMF, or it can carry several modes and is called multimode fiber (MMF). In the presence of multiple modes, modal dispersion takes place and causes a broadening of the transmitted pulse, and thus SMFs are generally preferred, especially for long distance transmission. Nevertheless, other sources of dispersion, such as chromatic and polarization dispersion, are usually available and have to be eliminated using special kinds of fibers, compensated by signal predistortion at the sender, or corrected at the receiver.

Figure 3.4 illustrates the dimensions of a standard SMF and the intensity distribution of the fundamental mode. The exact solution of this mode has a Bessel profile and is generally approximated by a Gaussian function [54]. The MFD corresponds to the diameter at which the intensity falls to $1/e^2$ of the maximum value and amounts to 10.4 μm for standard fibers of type SMF-28 [7]. It should be noted that the MFD in this case is larger than the core diameter 8.2 μm and is an important value when designing coupling structures to integrated nanowaveguides.

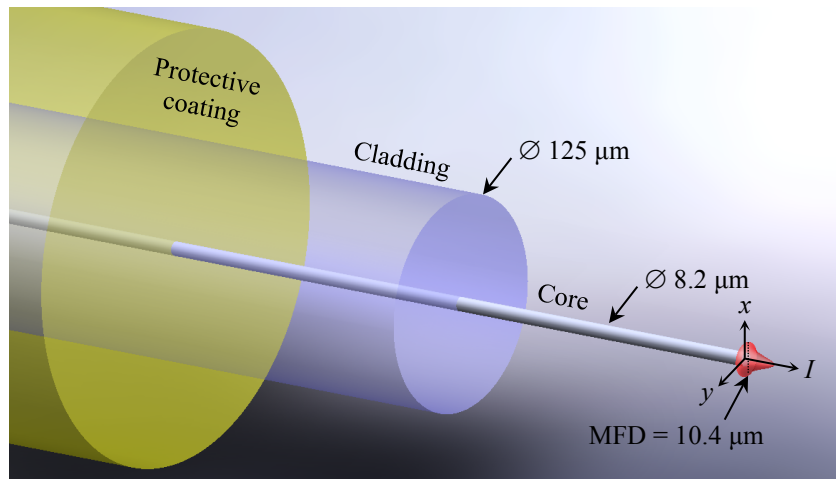


Figure 3.4: Schematic illustration of a standard SMF and the corresponding intensity distribution $I(x,y)$ of the fundamental mode.

3.1.3. Receiver concepts

After being transmitted on the optical link, the signal is demodulated at the receiver in accordance with the modulation scheme adopted at the sender. Receivers can mainly be classified into two categories depending on the detection procedure. While amplitude modulated signals are recovered by direct detection based on photodetectors, phase modulation requires additional optical components, and the signal is retrieved by coherent detection.

Since photodetectors can only measure the intensity of an optical signal, information encrypted in the phase is lost in direct detection schemes. Hence, light has to be mixed with a reference in an interferometric circuit to deliver the correct phase states before being detected by the photodetectors. The reference, also known as local oscillator (LO), can have the same frequency as the signal, and the demodulation procedure is called homodyne, or a different frequency, and the procedure is called heterodyne [46]. It should also be noted that there are other PSK modulation methods based on differentially encoded phases, such as differential phase shift keying (DPSK), which do not require coherent detection since information is encrypted in the phase difference of two consecutive symbols. In this case, instead of an LO source, a simple delay line interferometer (DLI) prior to OE conversion can be implemented [46].

In the case of wavelength or polarization multiplexed signals, additional optical components have to be realized on the receiver PIC. While WDM is demultiplexed by optical filters, for example using arrayed waveguide gratings (AWGs), PDM is retrieved based on PBSs that can be realized using simple waveguide structures or also diffraction gratings. In both methods, the basic circuit has to be repeated in function of the number of carriers. Figure 3.5 shows an example of an integrated DP QPSK receiver PIC in the SOI platform.

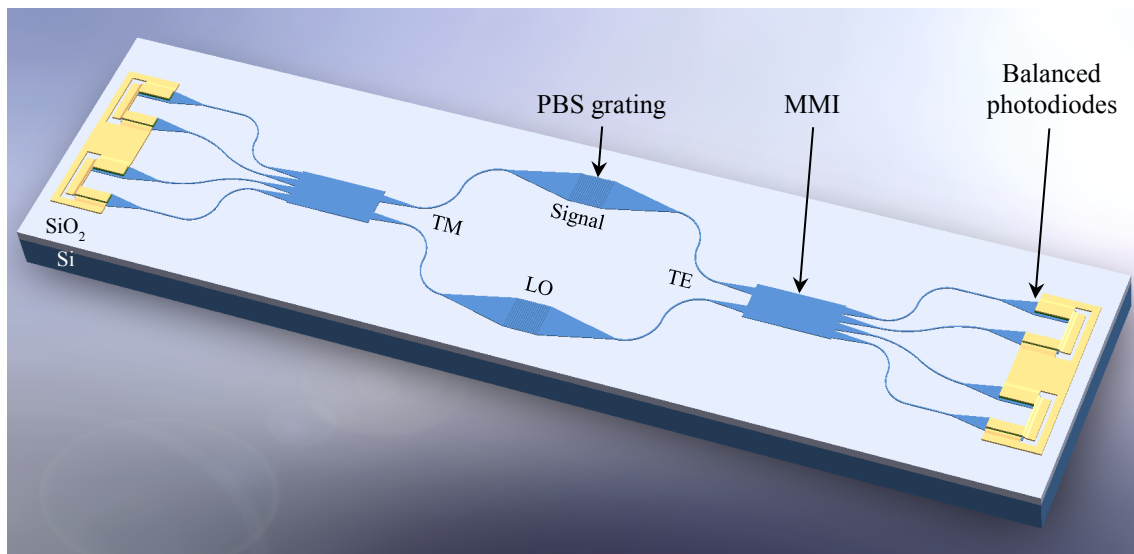


Figure 3.5: Graphical representation of a possible receiver PIC in the SOI platform based on the DP QPSK modulation technique.

The receiver PIC consists of two coupling elements for the signal and the LO, which rely here on polarization splitting diffractive gratings. The transverse electric (TE) state where the polarization is perpendicular to the waveguide sidewalls is directed to the right hand side of the PIC, whereas the other orthogonal polarization, the transverse magnetic (TM) state, is guided to the left hand side. In each section, the signal and the LO are mixed in the 90° hybrid, which is realized here using a 2×4 MMI, and the “I” and “Q” signal components are separated and subsequently detected by a pair of balanced photodetectors.

Finally, at the receiver IC, the photocurrent is amplified by transimpedance amplifiers (TIAs), and then the analog electrical signal is converted by ADCs to a digital one so that the digital signal processor (DSP) can compensate for dispersion and degradation

effects, which may have occurred over the optical link, and determines the transmitted information [55].

3.2. Electromagnetic wave propagation

As described in the previous subsections, optical transmission systems rely on the processing of light signals in photonic circuits and the propagation of these electromagnetic waves in linking elements such as nanowaveguides and fibers. To understand the theoretical background behind the waveguiding effect and in order to tackle the interface problem between PICs and optical fibers, a short insight into the fundamentals of the electromagnetic wave propagation is given.

3.2.1. Wave equations

To mathematically describe the interaction of electromagnetic waves with material, there are two important sets of equations that have to be considered: Maxwell's and material equations. For a sinusoidal time dependence of the field vectors, the complex form of Maxwell's equations is given by [56]

$$\text{curl}\vec{E} = -j\omega\vec{B}, \quad (3.1)$$

$$\text{curl}\vec{H} = \vec{J} + j\omega\vec{D}, \quad (3.2)$$

$$\text{div}\vec{D} = \rho, \quad (3.3)$$

$$\text{div}\vec{B} = 0, \quad (3.4)$$

where \vec{E} describes the electric field, \vec{B} the magnetic induction, \vec{H} the magnetic field, \vec{J} the current density, \vec{D} the dielectric displacement, and ρ the charge density. The angular frequency is denoted by $\omega = 2\pi f$, with f the electromagnetic wave frequency. All field quantities depend on time t and space, described by the position vector $\vec{r} = (x, y, z)$ in Cartesian coordinates, as follows

$$\vec{E} = \vec{E}(\vec{r})e^{j\omega t}. \quad (3.5)$$

The second set of equations is given by the material properties, which also relate the field quantities to each other. In linear, isotropic, and homogeneous media, these are

$$\vec{D} = \varepsilon_r \varepsilon_0 \vec{E}, \quad (3.6)$$

$$\vec{B} = \mu_r \mu_0 \vec{H}, \quad (3.7)$$

$$\vec{J} = \sigma \vec{E}, \quad (3.8)$$

with ε_0 and μ_0 the free space dielectric and magnetic constants respectively, whereas ε_r is the relative permittivity and μ_r is the relative permeability in the medium. Since the most used materials in the field of photonics are nonmagnetic, the permeability can be set to unity, i.e. $\mu_r = 1$. The conductivity is denoted by σ , which describes the ability of a material to conduct the electric current and at the same time losses interposing the electromagnetic waves.

The behavior of the electromagnetic waves depends strongly on the material properties. There are two main cases that have to be identified: lossless and lossy media. In the first case, for example in insulators, the conductivity is negligible, i.e. $\sigma = 0$. Taking into account the space dependence of the material properties in a system composed of different, lossless, charge-free regions and simplifying the time dependence of all field vectors, both previously described sets yield the general wave equations for the electric and magnetic field

$$\frac{1}{\varepsilon_r(\vec{r})} \text{curl}(\text{curl} \vec{E}(\vec{r})) = \left(\frac{\omega}{c_0}\right)^2 \vec{E}(\vec{r}), \quad (3.9)$$

$$\text{curl}\left(\frac{1}{\varepsilon_r(\vec{r})} \text{curl} \vec{H}(\vec{r})\right) = \left(\frac{\omega}{c_0}\right)^2 \vec{H}(\vec{r}), \quad (3.10)$$

with $c_0 = 1/\sqrt{\varepsilon_0 \mu_0}$ the velocity of light in vacuum. Each equation represents an eigenvalue problem, and the solution is the spatial profile of the corresponding field. Interestingly, there is a correlation between the dimensions of the system and the operating frequency. Scaling these dimensions by a factor $\nu \geq 1$ yields $\vec{r}' = \nu \vec{r}$, $\text{curl}' = \text{curl} / \nu$ and a new material configuration $\varepsilon'_r(\vec{r}') = \varepsilon_r(\vec{r})$ with the field profiles $\vec{E}'(\vec{r}')$ and $\vec{H}'(\vec{r}')$ [57]. The modified wave equations are then

$$\frac{1}{\varepsilon'_r(\vec{r}')}\text{curl}'(\text{curl}'\vec{E}'(\vec{r}')) = \left(\frac{\omega}{vc_0}\right)^2 \vec{E}'(\vec{r}'), \quad (3.11)$$

$$\text{curl}'\left(\frac{1}{\varepsilon'_r(\vec{r}')}\text{curl}'\vec{H}'(\vec{r}')\right) = \left(\frac{\omega}{vc_0}\right)^2 \vec{H}'(\vec{r}'), \quad (3.12)$$

and represent the same eigenvalue problem with the same solutions as in the original case but at the angular frequency $\omega' = \omega / \nu$. Hence, when scaling up the dimensions of a system by a certain factor, the behavior does not change at the reduced frequency by that factor. This may be advantageous when nanostructures cannot be investigated due to technological difficulties because enlarging the dimensions to the millimeter scale considerably relaxes the fabrication effort. In this case, instead of using light at THz frequencies, electromagnetic waves in the MHz or GHz ranges can be applied. Nevertheless, this condition is applicable only when the material properties are exactly the same in both domains, which cannot be guaranteed due to their frequency dependence. Indeed, similarly behaving dielectrics can be found in both frequency domains, but this is not a trivial task for lossy materials such as metals.

The solutions to the wave equations in a lossless, homogeneous medium can be given as

$$\vec{E}(\vec{r}) = \vec{E}_0 e^{-j\vec{k}\vec{r}}, \quad (3.13)$$

$$\vec{H}(\vec{r}) = \vec{H}_0 e^{-j\vec{k}\vec{r}}, \quad (3.14)$$

and represent a spatially plane wave with a phase propagating in the direction of the wave vector \vec{k} . The propagation direction of the energy flow is given by the Poynting vector, which is described by the cross product of the electric and magnetic field vectors

$$\vec{S}(\vec{r}) = \frac{1}{2} \text{Re}\left(\vec{E}(\vec{r}) \times \vec{H}^*(\vec{r})\right). \quad (3.15)$$

The dependence of the angular frequency on the wave number $k = |\vec{k}|$, also known as the propagation constant, is called the dispersion relation [58] and is represented by

$$\omega = \omega(k) = \frac{c_0}{n} k, \quad (3.16)$$

with $c_0/n = c$ the wave phase velocity and n the refractive index of the medium, which is related to the relative permittivity in nonmagnetic media as follows

$$n = \sqrt{\varepsilon_r \mu_r} \stackrel{\mu_r=1}{=} \sqrt{\varepsilon_r}. \quad (3.17)$$

The amplitudes of the electric and magnetic fields are also related to each other by the wave impedance [58]

$$Z = \frac{|\underline{E}|}{|\underline{H}|} = \sqrt{\frac{\mu_r \mu_0}{\varepsilon_r \varepsilon_0}} \stackrel{\mu_r=1}{=} \frac{1}{n} \sqrt{\frac{\mu_0}{\varepsilon_0}}, \quad (3.18)$$

which is constant in free space and denoted by Z_0 .

In the second case where conductivity exists such as in metals or lossy dielectrics, i.e. $\sigma \neq 0$, the relative permittivity has to be extended by the medium losses as follows

$$\underline{\varepsilon}_r = \varepsilon_r - j \frac{\sigma}{\omega \varepsilon_0} = \text{Re}(\underline{\varepsilon}_r) - j \text{Im}(\underline{\varepsilon}_r). \quad (3.19)$$

When this equation is inserted in (3.17), the refractive index becomes complex

$$\underline{n} = \sqrt{\underline{\varepsilon}_r} = n - j\kappa = \text{Re}(\underline{n}) - j \text{Im}(\underline{n}), \quad (3.20)$$

and hence the wave number as well. The imaginary part of the refractive index is called the extinction coefficient and is denoted by κ [56]. The solutions to the wave equations also contain in this case an exponentially decaying term, which describes a damped electromagnetic wave. The attenuation of the wave is generally associated to the energy absorption in the material [59]. Taking into account the frequency dependence of the conductivity, the complex relative permittivity can be furthermore expressed by the Drude model as [60]

$$\underline{\varepsilon}_r = \varepsilon_{r,\infty} - \frac{\omega_p^2}{\omega(\omega - j\gamma)}, \quad (3.21)$$

where $\varepsilon_{r,\infty}$ is the high-frequency relative permittivity, ω_p is the plasma angular frequency, and γ is the damping coefficient. At $\omega \ll \omega_p$, the real part of the relative permittivity is negative and large in magnitude, which implies a large extinction coefficient, and

hence high attenuation. This is a typical behavior in metals, which strongly reflect electromagnetic waves up to the optical range. Beyond the plasma frequency, which mainly lies in the ultraviolet (UV) region [61], the relative permittivity is positive, metals become transparent, and the waves are able to propagate.

3.2.2. Reflection and refraction

In addition to propagation in matter, there are several phenomena that encounter traveling electromagnetic waves, especially at the boundary of different media. The simplest case is reflection and refraction at the interface of two materials with different refractive indices n_1 and n_2 . Figure 3.6 illustrates a transverse plane wave incident at an angle α_i from medium 1 to medium 2 for the two orthogonal polarizations TE and TM, depending on whether the electric or magnetic field is perpendicular to the plane of incidence [62].

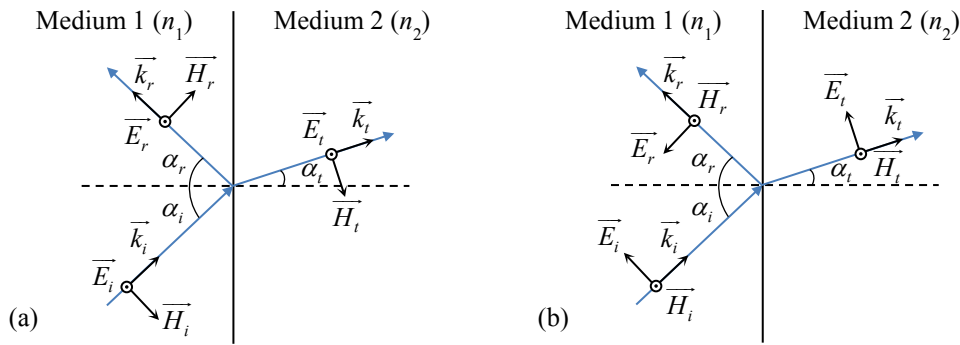


Figure 3.6: Reflection and refraction at the interface of two materials with $n_2 > n_1$ for a (a) TE and (b) TM wave.

For both cases, due to the continuity conditions at the boundary, a part of the incident wave is reflected back in medium 1 at an angle

$$\alpha_r = \alpha_i, \quad (3.22)$$

while the other part is transmitted to medium 2 at an angle α_t following Snell's law

$$n_1 \sin \alpha_i = n_2 \sin \alpha_t. \quad (3.23)$$

Snell's law is valid even when one of the media exhibits a negative refractive index. For example when $n_2 < 0$, the transmitted part does not propagate in the ordinary direction

but is negatively diffracted following an angle $-\alpha_t$. The electric field, the magnetic field, and the wave vector then form a left-handed system, in contrast to the conventional right-handed system shown in Figure 3.6. Indeed, negative refractive indices do not exist in nature, but artificial structures can be engineered to exhibit such behaviors using metamaterials for example as explained in the fourth chapter.

The latter laws, together with the boundary conditions, can be used to express the power reflection and transmission factors, also called reflectivity R and transmissivity T , as a function of the angles and media properties, i.e. refractive indices n_1 and n_2 or wave impedances Z_1 and Z_2 of medium 1 and medium 2 respectively. Depending on the polarization of the electromagnetic wave, the Fresnel equations for reflection are [62]

$$R_{\text{TE}} = \left| \frac{n_1 \cos \alpha_i - n_2 \cos \alpha_t}{n_1 \cos \alpha_i + n_2 \cos \alpha_t} \right|^2 = \left| \frac{Z_2 \cos \alpha_i - Z_1 \cos \alpha_t}{Z_2 \cos \alpha_i + Z_1 \cos \alpha_t} \right|^2, \quad (3.24)$$

$$R_{\text{TM}} = \left| \frac{n_2 \cos \alpha_i - n_1 \cos \alpha_t}{n_2 \cos \alpha_i + n_1 \cos \alpha_t} \right|^2 = \left| \frac{Z_1 \cos \alpha_i - Z_2 \cos \alpha_t}{Z_1 \cos \alpha_i + Z_2 \cos \alpha_t} \right|^2. \quad (3.25)$$

Due to the conservation of energy, the transmissivity for any polarization is given by

$$T_{\text{TE|TM}} = 1 - R_{\text{TE|TM}}. \quad (3.26)$$

In the special case when the electromagnetic wave propagates from medium 1 and perpendicularly impinges medium 2, i.e. $\alpha_i = 0$, the power reflection factors are identical for both polarizations, and hence the transmission factors as well. The reflectivity can then be expressed for the lossless case as

$$R = \frac{(n_1 - n_2)^2}{(n_1 + n_2)^2}, \quad (3.27)$$

whereas it amounts to

$$R = \frac{(n_1 - n_2)^2 + \kappa^2}{(n_1 + n_2)^2 + \kappa^2} \quad (3.28)$$

when medium 2 is lossy and possesses a complex refractive index $\underline{n}_2 = n_2 - j\kappa$. At frequencies far below the plasma frequency, metals exhibit large extinction coefficients, and consequently a high reflectivity $R \approx 1$ [56].

3.2.3. Interference and diffraction

Another important phenomenon that has to be considered in this chapter is the interference of electromagnetic waves. This principle takes place in a variety of photonic integrated components such as MMIs, MZMs, and coupling gratings, giving rise to different functionalities that can be used in optical data processing. Interference occurs by superposing at least two coherent waves, i.e. with a constant phase relation in space or time, so that the resulting intensity distribution can be smaller or larger than the intensity of the individual waves, depending on their phase relationship [63].

For example, two waves with nonorthogonal electric fields \vec{E}_1 and \vec{E}_2 having the same angular frequency ω and a phase difference $\Delta\varphi$

$$\begin{aligned}\vec{E}_1 &= \vec{E}_{1,0} e^{j\omega t} e^{-j\vec{k}\vec{r}} = \vec{E}_{1,0} e^{j\delta_1} \\ \vec{E}_2 &= \vec{E}_{2,0} e^{j(\omega t + \Delta\varphi)} e^{-j\vec{k}\vec{r}} = \vec{E}_{2,0} e^{j\delta_2}\end{aligned}\quad (3.29)$$

can be superposed to produce an electric field $\vec{E} = \vec{E}_1 + \vec{E}_2$, and hence an intensity, which is proportional to the squared magnitude of this field

$$I \sim |\vec{E}|^2 = \vec{E} \cdot \vec{E}^* = E_{1,0}^2 + E_{2,0}^2 + 2\vec{E}_{1,0} \cdot \vec{E}_{2,0} \cos(\delta_2 - \delta_1). \quad (3.30)$$

Thus, for a phase difference equal to $2m\pi$, where m is an integer, the intensity is maximal and the interference is called constructive, whereas for a phase difference of $(2m+1)\pi$ the intensity is minimal and the interference is called destructive. This effect is used in coherent detection for example in order to convert the phase information into intensity so that it can be detected by a photodiode.

Another example where interference takes place and represents the origin of several optical applications is based on a configuration called the Fabry-Pérot resonator [64]. Here light confined between two highly reflective mirrors gives rise to standing waves when interfering constructively at certain resonance frequencies. This effect plays a big role in lasers, waveguides, and interferometric structures, but it can also be harmful if the resonant reflections are not desirable in a certain system. The frequency difference Δf , or also wavelength difference $\Delta\lambda_0$, between two adjacent resonant modes is known as the free spectral range (FSR) and is given by [64]

$$\Delta f = \frac{c_0}{2n_g L_c} \text{ or } \Delta \lambda_0 = \frac{\lambda_{0,1} \lambda_{0,2}}{2n_g L_c}, \quad (3.31)$$

where n_g is the group index of the medium between the mirrors and L_c is the cavity length. $\lambda_{0,1}$ and $\lambda_{0,2}$ are the wavelengths of these two adjacent modes.

Interference also occurs when a single propagating electromagnetic wavefront encounters an obstacle by passing through an aperture. This phenomenon is called diffraction and can be explained by Huygens' principle, which indicates that each electromagnetic wavefront represents a source of secondary wavelets that can interfere when being bent on objects or obstacles [63]. The diffracted field is then obtained by summing all wavelet contributions on the aperture area A according to the Fraunhofer diffraction integral [63], and the resulting intensity distribution is given as

$$I = C \left| \int_A e^{-jk\vec{r}} dA \right|^2, \quad (3.32)$$

where C is a constant.

In the simplest case where a wave of a wavelength $\lambda = 2\pi/k$ traversing a very long rectangular slit aperture with a length l along the x -direction and a width w along the y -direction, there exists a path difference between the rays transmitted through the slit, which can be approximated for small diffraction angles α_m by $r - r_0 \approx y \sin \alpha_m$ as shown in Figure 3.7. The intensity distribution, calculated in appendix A.1, is then expressed as

$$I = C \left| \int_{-w/2}^{w/2} e^{-jk(r_0 + y \sin \alpha_m)} l dy \right|^2 \stackrel{\text{A.1}}{=} I_0 \left(\frac{\sin \gamma_s}{\gamma_s} \right)^2, \quad (3.33)$$

$$\text{with } \gamma_s = \frac{1}{2} kw \sin \alpha_m. \quad (3.34)$$

The resulting diffraction pattern shows intensity maxima and minima that are produced by the constructive and destructive interferences originating from the secondary wavelets.

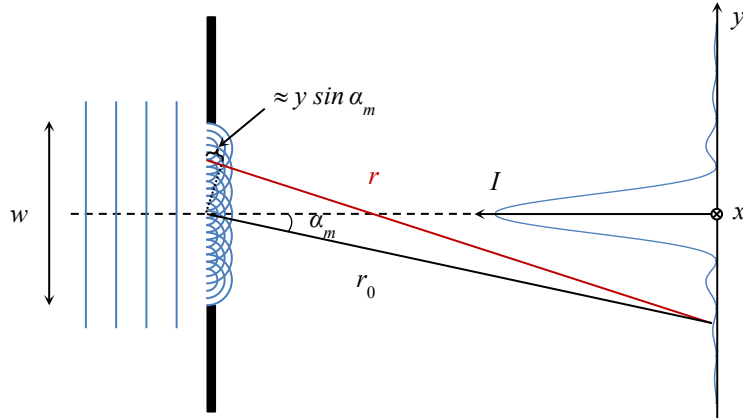


Figure 3.7: Schematic illustration of a diffracted plane wave at a single-slit aperture and the corresponding intensity distribution in the far field [63].

In the case of a rectangular aperture having a length in the order of the width dimension, a similar interference fringe is also observed in the x -direction, whereas a circular aperture of a diameter D gives a slightly different pattern. In the latter configuration, the intensity distribution is expressed by

$$I = C \left| \int_{-D/2}^{D/2} e^{-jk(r_0 + y \sin \alpha_m)} \left(2\sqrt{\left(\frac{D}{2}\right)^2 - y^2} \right) dy \right|^2 \stackrel{\text{A.2}}{=} I_0 \left(\frac{J_1(\gamma_c)}{\gamma_c} \right)^2, \quad (3.35)$$

$$\text{with } \gamma_c = \frac{1}{2} kD \sin \alpha_m \quad (3.36)$$

and J_1 the Bessel function of the first kind of order 1 as demonstrated in appendix A.2. The obtained symmetric diffraction pattern consists then of a bright spot in the middle, called Airy disk [63], surrounded by fading out rings. When a circular dielectric lens is additionally positioned in front of the aperture for focusing purposes, the diameter of the focused spot D_f can be determined from the minimum diffraction angle $\alpha_{m,\min}$ according to $I(\alpha_{m,\min}) = 0$. As the first zero of the Bessel function J_1 takes place at a value of around 3.83, the last equation yields

$$\frac{1}{2} kD \sin \alpha_{m,\min} \approx 3.83, \quad (3.37)$$

and hence for small diffraction angles

$$D_f \approx 2\alpha_{m,\min} F = 2.44\lambda \frac{F}{D}, \quad (3.38)$$

where F represents the focal length of the used lens. That means that the spot size depends not only on the light wavelength but also on the properties of the used lens. In general, a lens is characterized by its numerical aperture (NA), which is defined as [63]

$$\text{NA} \approx \frac{nD}{2F}, \quad (3.39)$$

where n is the refractive index of the surrounding material. Hence, the minimal achievable focus for a wavelength $\lambda = \lambda_0/n$ is

$$D_f = 1.22 \frac{\lambda_0}{\text{NA}}, \quad (3.40)$$

with λ_0 the free space wavelength. The latter relation shows that the optical resolution of lensing systems is restricted to the numerical aperture, and hence light emitted from an object cannot be infinitesimally focused. This is a direct consequence of the diffraction effect, and therefore conventional lensing systems are called diffraction-limited.

According to (3.40), it may be claimed that very large apertures $\text{NA} \rightarrow \infty$ may enable extremely small spots $D_f \rightarrow 0$. Nevertheless, due to Heisenberg's uncertainty principle for a propagating wave with a wave number $k = 2\pi/\lambda$, the transverse wave vector component k_T ranging from $-k$ to k given by [8]

$$\Delta r \Delta k_T \geq 2\pi \quad (3.41)$$

$$\text{yields } D_f \approx \Delta r_{\min} = \frac{2\pi}{2k} = \frac{\lambda}{2}. \quad (3.42)$$

Thus, no matter how large the lens aperture is, the focus size is at least limited to half the wavelength.

It should be noted that the limit described by (3.40) gets even worse due to the aberration effects in conventional lenses, such as spherical aberration [65], so that the focused spot size becomes much larger, and hence standard spherical lenses may be restrictive for nanocoupling purposes. However, the latter effect can be minimized using aspheric

configurations or also lenses based on materials with a negative index [29] as shown in the fourth chapter.

Finally, in order to visualize the behavior of diffraction gratings, a similar aperture to the first case is used but with N slits of a period Λ instead of a single-slit as shown in Figure 3.8.

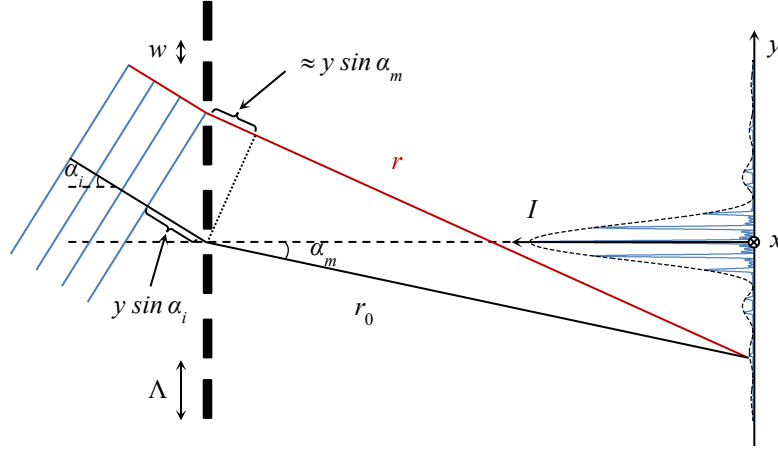


Figure 3.8: Schematic illustration of a diffracted plane wave at a grating with several slits and the corresponding intensity distribution in the far field [63].

Here the wavefront is incident at an angle α_i , and the total path difference between the rays transmitted through the slits is $r - r_0 = y(\sin \alpha_m - \sin \alpha_i)$. Hence, the intensity distribution in the far field is

$$I = C \left| \sum_{i=0}^{N-1} \int_{i\Lambda-w/2}^{i\Lambda+w/2} e^{-jk(r_0+y\sin\alpha_m-y\sin\alpha_i)} dy \right|^2 \stackrel{\text{A.3}}{=} I_0 \left(\frac{\sin \gamma_s}{\gamma_s} \right)^2 \left(\frac{\sin N\gamma_n}{\sin \gamma_n} \right)^2, \quad (3.43)$$

$$\text{with } \gamma_s = \frac{1}{2}kw(\sin \alpha_m - \sin \alpha_i) \text{ and } \gamma_n = \frac{1}{2}k\Lambda(\sin \alpha_m - \sin \alpha_i) \quad (3.44)$$

as shown in appendix A.3. The first term of the distribution is the intensity envelope and is similar to the result obtained using a single-slit, whereas the second term originates from the interference of the waves emitted from the different slits. The principal maxima take place at $\gamma_n = m\pi$, where m is an integer, called the diffraction order [63]. This yields the phase relation for constructive interference

$$k\Lambda(\sin \alpha_m - \sin \alpha_i) = 2m\pi, \text{ and hence} \quad (3.45)$$

$$k \sin \alpha_i + m \frac{2\pi}{\Lambda} = k \sin \alpha_m, \quad (3.46)$$

which represents the main equation for diffractive gratings, known as Bragg's law [66]. Using the latter relation, the period can be adequately determined in order to excite a specific diffraction order at the target wavelength and incidence angle. This result is discussed in detail in the fifth chapter.

3.3. Waveguiding effect

The main phenomena that encounter electromagnetic waves when propagating from a material to another one are discussed in the previous subchapter. In order to understand the waveguiding effect in integrated nanowaveguides and in optical fibers, the effects of reflection and refraction in dielectrics have to be called again with the condition that the wave propagates from medium 1 with a higher refractive index than medium 2, i.e. $n_1 > n_2$. It is clear that at incidence angles higher than a certain critical angle α_c with

$$\sin \alpha_c = \frac{n_2}{n_1}, \quad (3.47)$$

Snell's law yields [62]

$$\cos \alpha_t = -j \sqrt{\frac{n_1^2}{n_2^2} \sin^2 \alpha_i - 1}. \quad (3.48)$$

Inserting this imaginary value in the solutions to the wave equations at oblique incidence, it is clear that the wave decays evanescently in medium 2 while being totally back reflected to medium 1 [62]. This effect, therefore, called total internal reflection, can be used to confine waves in a material that is surrounded by another one with a lower refractive index. This behavior is similar to waveguiding in hollow metal pipes where electromagnetic waves at radio frequencies are kept inside by reflection on the metallic walls due to their high reflectivity [58].

It should be noted that the wave is not reflected directly at the interface between both dielectric materials but at a virtual plane defined by the penetration depth in medium 2.

Consequently, the wave suffers a phase shift ϕ_G produced by the lateral displacement, known as Goos-Hänchen shift [44].

3.3.1. Planar waveguides

Figure 3.9 illustrates an example of a symmetric planar structure where the wave is vertically guided in the film layer for incidence angles $\alpha_i = \alpha_r = \alpha > \alpha_c$. This wave can be observed as effectively propagating in the z -direction with the propagation constant

$$k = k_0 n_1 \sin \alpha = k_0 n_{eff} , \quad (3.49)$$

where k_0 is the wave number in free space and n_{eff} represents the effective refractive index of the waveguide [62].

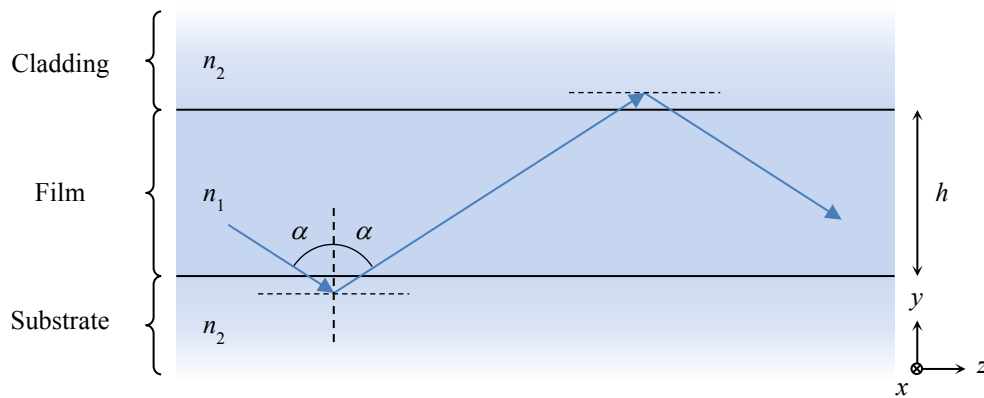


Figure 3.9: Schematic representation of a symmetric planar waveguide.

Since the wave is bouncing back and forth in the y -direction between the substrate and the cladding, interference takes place within the film layer. A waveguiding mode can be defined when the wave is constructively reproduced after each round-trip according to the following phase condition [62]

$$2k_0 n_1 h \cos \alpha - 2\phi_G = 2m\pi , \quad (3.50)$$

where h is the film layer thickness and m is an integer. The solutions to this equation represent the possible modes that are able to propagate in the symmetric planar waveguide and are identical for both TE and TM polarizations. When the substrate and the cladding have unequal refractive indices, i.e. the waveguide is asymmetric, the phase

condition has to be modified accordingly. In this case, two different sets of solutions have to be distinguished depending on the used polarization.

For a symmetric planar waveguide, the latter equation can be further developed to deliver the required thickness, for which only a single mode is present, as follows [62]

$$V\sqrt{1-B} = m\pi + 2 \arctan \sqrt{\frac{B}{1-B}}, \quad (3.51)$$

where V and B are the frequency and phase parameters respectively, defined as

$$V = k_0 h \sqrt{n_1^2 - n_2^2} \quad \text{and} \quad B = \frac{n_{\text{eff}}^2 - n_2^2}{n_1^2 - n_2^2}. \quad (3.52)$$

This means that for a given thickness h , there exist m different modes that are able to propagate. According to (3.51), the single-mode condition for the phase parameter can be written as $V < \pi$, which yields the maximum film layer thickness

$$h_{\text{max}} = \frac{1}{2} \cdot \frac{\lambda_0}{\sqrt{n_1^2 - n_2^2}}. \quad (3.53)$$

For example, at a wavelength of 1550 nm and using $n_1 = 3.476$ and $n_2 = 1.444$ [67], only the fundamental mode is able to propagate in the planar SOI waveguide when the Si layer thickness is less than or equal to 250 nm. The profile of the fundamental mode can be obtained by solving the wave equations in each region of the stack and using the corresponding propagation constants [62].

3.3.2. Strip waveguides

In order to ensure additional horizontal confinement to guide the wave in a wire-like configuration on the chip, there exist several geometrical types such as the rib, the strip, and the diffused waveguides [68]. The most common form is based on the rectangular buried strip since it offers the most compact dimensions among all dielectric waveguides. Indeed, the approximate value of the width parameter can be similarly calculated for single-mode condition when using the effective index of each region in the stack. However, nonplanar waveguides do not generally support TE and TM modes as in the planar case, but also other hybrid modes with nonzero components in the propagation

direction [68]. This approximation, therefore, is unreliable and the exact parameters cannot be determined adequately. For this purpose, numerical approaches, such as the beam propagation method [68], have to be applied.

Using the commercial software RSoft BeamPROP, it is still possible to identify two cases based on the orthogonal polarizations, the quasi-TE and quasi-TM. The reason for this behavior is that most waveguides support modes with a predominant polarization, whereas a small energy fraction is guided in the other polarization [69]. In order to guarantee the single-mode condition for both states, analytical approximations have been introduced based on numerical simulations. For a strip SOI waveguide of a height h and a width w , the following condition must therefore be fulfilled [67]

$$\frac{w}{\mu\text{m}} \leq -1.405 \frac{h}{\mu\text{m}} + 0.746. \quad (3.54)$$

For example, for a Si film layer of a thickness of 250 nm, the maximum waveguide width has to be around 400 nm. Using these parameters, the electric field profiles of the quasi-TE and quasi-TM fundamental modes, for simplicity hereinafter called TE and TM, are represented in Figure 3.10. Here the main part of the electric field is lying along the x -direction for TE and along the y -direction for the TM mode. The effective refractive index of both single-mode waveguides amounts to $n_{\text{eff,TE}} = 2.4$ and $n_{\text{eff,TM}} = 2$.

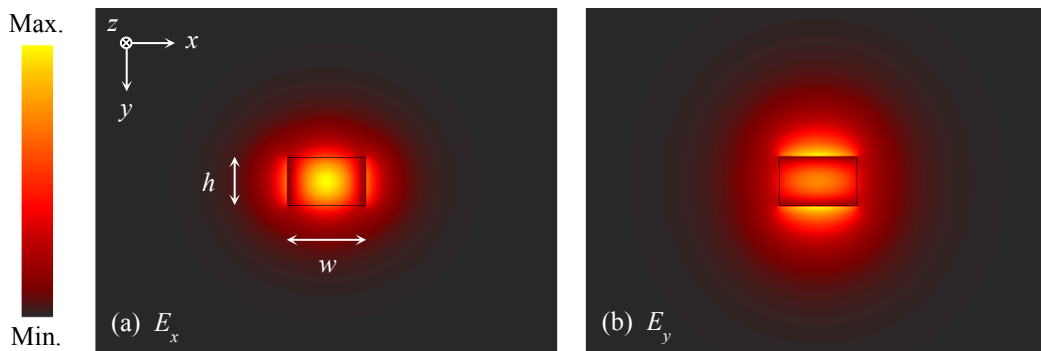


Figure 3.10: Electric field profile of a Si waveguide embedded in a SiO₂ environment at a wavelength of 1550 nm with $h = 250$ nm and $w = 400$ nm for (a) TE and (b) TM.

In general, the fundamental mode profile of these waveguides is described by a cosine function within the film layer and evanescently decaying parts in the surrounding medi-

um, which are the direct solutions to the wave equations [62], so that the overall profile can be approximated by a Gaussian function. However, both configurations show a discontinuity at the waveguide interface along the direction of the major component as illustrated in Figure 3.11. In fact, in material systems with a high refractive index contrast such as in SOI, the boundary conditions at the interface enforce the electric field in the cladding to suffer a large amplitude jump [70]. This is dictated by the fact that the normal component of the dielectric displacement at the interface has to be the same, i.e. $\varepsilon_{r,1}E_{n,1} = \varepsilon_{r,2}E_{n,2}$, with $E_{n,1}$ and $E_{n,2}$ are the major normal components of the electric field in the film and cladding layers respectively [62]. Taking the example of the TE mode, it follows

$$\frac{E_{x,2}}{E_{x,1}} = \left(\frac{n_1}{n_2}\right)^2, \quad (3.55)$$

which shows that the electric field, and hence the intensity, experiences a considerable increase at the Si/SiO₂ interface due to the large index difference. Therefore, the commonly used Gaussian approximation of the fundamental mode in the waveguide may not be adequate, and numerical methods have to be applied when optimizing coupling between different cross sections.

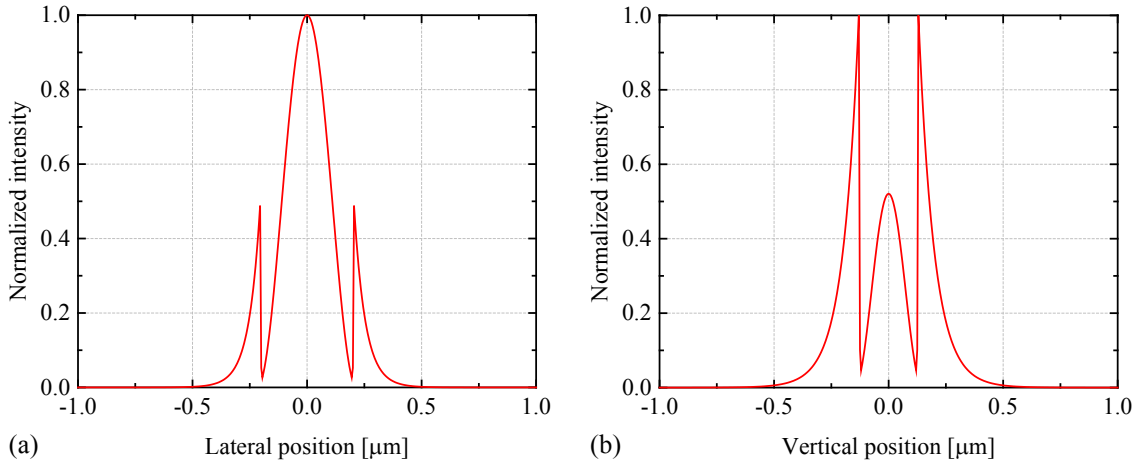


Figure 3.11: Fundamental mode profile (a) along the x -direction for TE and (b) along the y -direction for TM. The position at 0 μm corresponds to the center of the waveguide cross section.

It should be noted that the width of the waveguide can be enlarged to adapt the dimensions of wider integrated structures while still ensuring the single-mode condition. The simplest method to achieve good mode conversion efficiency between the two different cross sections is by adiabatically increasing the width along a sufficient length as exemplified in Figure 3.12(a). Here the fundamental mode of a nanowaveguide of a width $w_1 = 400$ nm and a height $h = 250$ nm is successfully converted to the fundamental mode of the larger waveguide having a width $w_2 = 10$ μm using a taper length of 100 μm . The simulated mode conversion efficiency in both directions is the same due to reciprocity and amounts to nearly 95%.

The transmission efficiency can be improved to approach 1 when the taper length is further increased as illustrated in Figure 3.12(b). Hence, there exists a trade-off between the required efficiency and the available footprint. It is also clear that the larger the width w_2 is, the longer the taper has to be for a certain mode conversion efficiency. While $w_2 = 5$ μm requires only a length of nearly 20 μm to achieve at least an efficiency of 95%, tapering to a width of 15 μm necessitates a length larger than 250 μm .

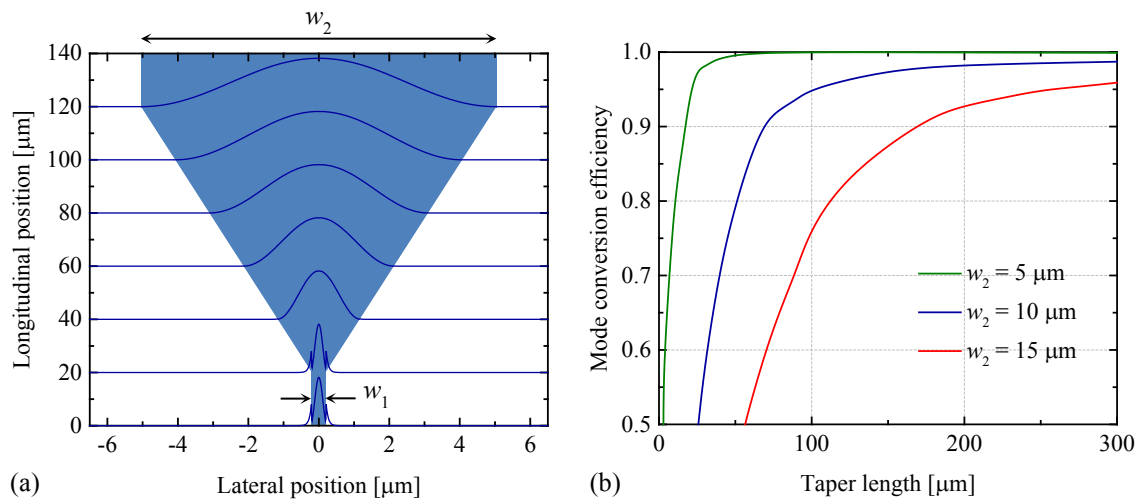


Figure 3.12: (a) Normalized intensity distributions during fundamental mode conversion between $w_1 = 400$ nm and $w_2 = 10$ μm along a linear taper. (b) Mode conversion efficiency of different w_2 values. The 3D simulations are done using RSoft BeamPROP for TE polarization at a wavelength of 1550 nm.

3.3.3. Single-mode optical fibers

In order to visualize the mode profile of an SMF, similar analytical approaches as previously shown for the planar waveguide can be applied since an optical fiber is a rotationally symmetric waveguide that obeys the effect of total internal reflection. The results are Bessel functions, defining the mode profiles of the fiber, and can be found in [68]. The single-mode condition for the core diameter D_F is given by the frequency parameter $V < 2.405$ [68], which yields

$$D_{F,max} = \frac{2.405}{\pi} \cdot \frac{\lambda_0}{\sqrt{n_1^2 - n_2^2}}. \quad (3.56)$$

Assuming $n_1 = 1.449$ and $n_2 = 1.444$ [71], the core diameter has to be less than or equal to $9.8 \mu\text{m}$ for an operating wavelength of 1550 nm . Using a standard fiber of type SMF-28 with $D_F = 8.2 \mu\text{m}$ [7], the fundamental mode profile is simulated and illustrated in Figure 3.13(a). In general, due to the small index contrast between the core and the cladding, the corresponding intensity profile can be approximated by a Gaussian function, which is shown in Figure 3.13(b) and given by

$$I(x, y) = I_0 e^{-2 \frac{x^2 + y^2}{(\text{MFD}/2)^2}}. \quad (3.57)$$

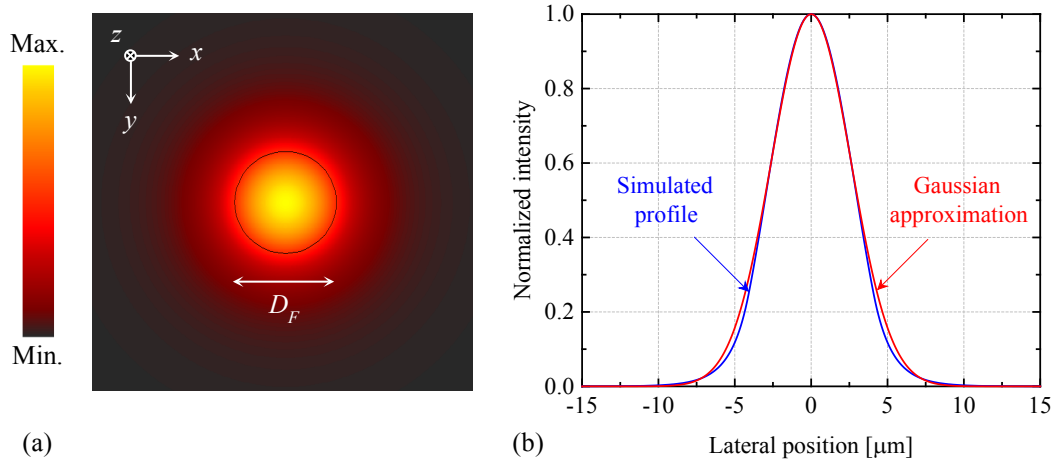


Figure 3.13: (a) Fundamental mode profile of an SMF with $D_F = 8.2 \mu\text{m}$ and (b) the corresponding intensity profile versus a Gaussian approximation with $\text{MFD} = 10.4 \mu\text{m}$. The position at $0 \mu\text{m}$ corresponds to the center of the fiber core cross section.

It is clear that both profiles of the integrated SOI waveguide and the optical fiber exhibit a large mode mismatch that cannot be easily bridged by direct coupling and needs an adequate technique to enhance the transmission efficiency.

3.4. Wave propagation in periodic media

In this thesis, the two adopted methods that are investigated to increase the coupling efficiency between optical fibers and integrated nanowaveguides rely on periodic media. Hence, it is necessary to present the main similarities and differences in such kind of arrangements.

In general, periodic media are described by the translational symmetry of their optical properties [72], i.e. in the case of nonmagnetic materials the permittivity distribution is invariant after a certain period Λ , also called lattice constant, and can be given by

$$\varepsilon_r(\vec{r}) = \varepsilon_r(\vec{r} + \vec{\Lambda}), \quad (3.58)$$

where $\vec{\Lambda}$ represents an arbitrary lattice vector. According to the Bloch theorem, the solutions to Maxwell's equations in such a periodic medium, known as Bloch waves, are a product of plane waves and periodic functions [72], described by

$$\vec{E}(\vec{r}) = \vec{E}_K(\vec{r})e^{-j\vec{K}\vec{r}} \quad \text{and} \quad \vec{H}(\vec{r}) = \vec{H}_K(\vec{r})e^{-j\vec{K}\vec{r}}, \quad (3.59)$$

where \vec{K} is the Bloch wave vector, whereas $\vec{E}_K(\vec{r})$ and $\vec{H}_K(\vec{r})$ are given as follows

$$\vec{E}_K(\vec{r}) = \vec{E}_K(\vec{r} + \vec{\Lambda}), \quad \vec{H}_K(\vec{r}) = \vec{H}_K(\vec{r} + \vec{\Lambda}). \quad (3.60)$$

In this case, the dispersion relation is more complex than in the homogeneous medium since for a certain K value different angular frequencies, corresponding to different Bloch modes, are possible [72]. In addition, there exist frequency regions where wave propagation is prohibited called photonic band gaps [57]. The reason for this behavior is that Bragg diffraction takes place when the period is in the order of the wavelength, and hence the overall response is governed by interference, which may be constructive for some frequencies and destructive for others. Due to their similarity to periodic crystal

structures, these arrangements are also known as photonic crystals [57]. Bragg gratings are an example of one-dimensional (1D) photonic crystals, which can be used to transmit certain frequencies or also to stop and reflect others and work as mirrors.

When the wavelength is much larger than the period, the wave does not perceive the fine structures anymore and diffraction does not take place as previously described. Instead, the electromagnetic response is governed by the effective-medium theory where the wave does not interact with the individual arrangements but with the averaged optical properties of the whole system [73]. NIMs are an example of artificially engineered materials that gain their effective characteristics from the overall response since the unit cells have subwavelength dimensions, which cannot be resolved by the electromagnetic wave. Although metamaterials are made by nonmagnetic metallic and dielectric structures, they may exhibit a strong magnetic response and permeability values different from unit when designed adequately. Hence, effective parameters can be assigned to these materials

$$\underline{\epsilon}_r = \underline{\epsilon}_{r,eff}, \underline{\mu}_r = \underline{\mu}_{r,eff}, \quad (3.61)$$

where $\underline{\epsilon}_{r,eff}$ and $\underline{\mu}_{r,eff}$ are the complex-valued effective permittivity and permeability respectively. Therefore, the effective refractive index of the medium is

$$\underline{n}_{eff} = \sqrt{\underline{\epsilon}_{r,eff} \underline{\mu}_{r,eff}}. \quad (3.62)$$

The question when metamaterials can be treated as homogeneous materials with effective internal properties is, however, controversial since not all metamaterials possess subwavelength unit cells. In addition, the limit between acting as a photonic crystal or as a metamaterial with bulk properties cannot be determined easily. In this case, it is more convenient to study the response of the entire system using simulation tools rather than retrieving the characteristics of a single unit cell and assigning them to the whole material.

It should also be noted that the periodicity may be changed for both cases, for example by building gradient or apodized profiles in order to achieve certain functionality or to optimize the overall system response [74], [75].

4. Negative index metamaterials

In this chapter, the first coupling method based on metamaterials having an effective negative refractive index is presented. After an introduction on the theory behind negative refraction, the salient focusing ability using perfect NIM lenses is demonstrated. The adopted fishnet design for the realization of NIM multilayers at radio frequencies is then described and numerically investigated. Finally, measurement results of the fabricated samples are shown, and the limiting factors when scaling the dimensions down to optical wavelengths are emphasized.

4.1. Theory of metamaterials

Metamaterials can be defined as artificially engineered materials that possess properties not found in nature [73]. This general definition indicates that the designed material may exhibit arbitrary values of permittivity ϵ_r and permeability μ_r , and hence can initiate novel effects that are not observed in daily life. Figure 4.1 shows all possible combinations of $Re(\epsilon_r)$ and $Re(\mu_r)$ and the resulting electromagnetic wave behavior in the corresponding medium.

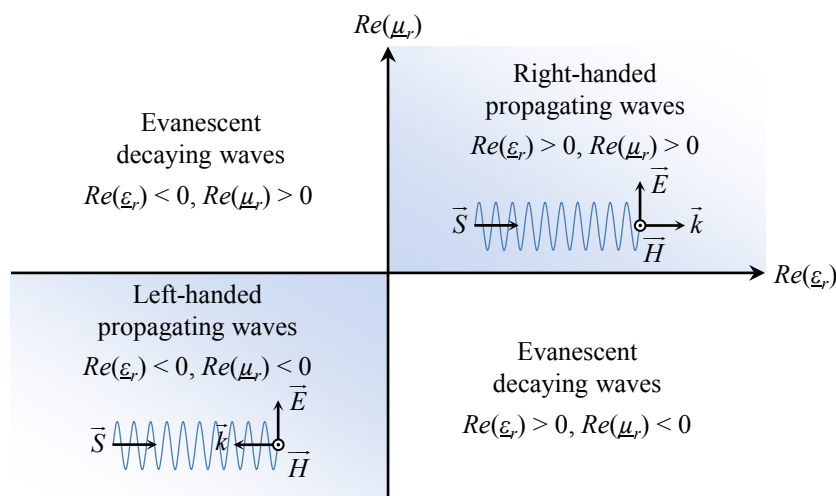


Figure 4.1: Classification of the materials according to the sign of their permittivity and permeability real part [76].

While most ordinary materials, such as dielectrics, are summarized in the first quadrant with forward propagating waves, the second and fourth quadrants, representing electric and magnetic plasma, comprehend evanescent waves due to the imaginary nature of the resulting refractive index. These behaviors have been discussed for the most part in the previous chapter taking the example of propagating waves in lossless dielectrics and attenuated waves in metals. However, no natural materials are known to feature the properties of the third quadrant, i.e. with $Re(\underline{\epsilon}_r) < 0$ and $Re(\underline{\mu}_r) < 0$.

4.1.1. The negative refractive index

According to (3.17), a hypothetical material with simultaneously negative permittivity $\underline{\epsilon}_r = -|\underline{\epsilon}_r|$ and permeability $\underline{\mu}_r = -|\underline{\mu}_r|$ interestingly delivers a negative refractive index

$$\underline{n} = \sqrt{\underline{\epsilon}_r} \sqrt{\underline{\mu}_r} = \sqrt{|\underline{\epsilon}_r|} e^{j\frac{\pi}{2}} \sqrt{|\underline{\mu}_r|} e^{j\frac{\pi}{2}} = -\sqrt{|\underline{\epsilon}_r| |\underline{\mu}_r|}, \quad (4.1)$$

which evokes in turn a propagating wave without violating any physical laws. When incident at the interface of two different materials with positive and negative refractive indices, light is refracted in the wrong direction while still obeying Snell's law as illustrated in Figure 4.2(a). In addition, the phase velocity is negative and the wave vector is directed against the energy flow, building a left-handed system. Starting from these simple reflections, it is clear that a flat medium with a negative refractive index is able to focus a diverging beam of a point source as shown in Figure 4.2(b). In this case, not only propagating waves, but evanescent waves carrying fine-structure information too, can be reproduced to enable subwavelength imaging [28].

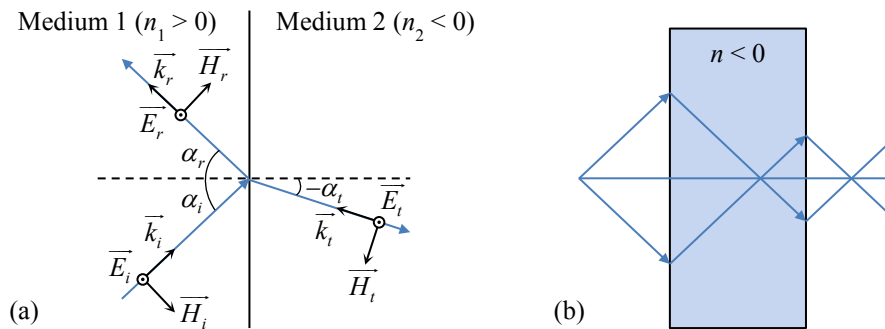


Figure 4.2: (a) Reflection and refraction at the interface of two materials with $n_1 > 0$ and $n_2 < 0$ for a TE wave. (b) Focusing by a negative index slab.

Due to the lack of negative index materials in nature, these attractive effects remained unexplored until the pioneering work of Pendry in which he proposed to achieve arbitrary values of permittivity and permeability by engineering thin metallic wires and split rings [77], [78]. In fact, by arranging thin metallic structures periodically, the average electron concentration is diluted and the electric plasma frequency can be reduced from UV down to microwaves so that negative permittivity can be designed at an arbitrary frequency.

On the other hand, structured thin metallic sheets can be designed to generate virtual current loops, which induce a magnetic field opposite to the incident one and give rise to a resonant inductive-capacitive (LC) behavior as demonstrated in appendix B. Hence, negative permeabilities become accessible at frequencies between the magnetic resonance and the so-called magnetic plasma frequency [78]. These antiparallel currents originate from the propagation of SPPs at the dielectric-metallic interfaces when the phase matching condition between the incident light and the SPPs is met [79], and thus the LC resonances are also known as SPP resonances.

When combining both effects so that the magnetic resonance takes place below the electric plasma frequency, the artificial material exhibits an effective negative refractive index.

4.1.2. Homogenization and retrieval procedure

As previously mentioned, metamaterials are composed of periodically patterned structures whose parameters can be tuned to achieve any electromagnetic properties at the desired frequency. In order to treat the overall composition as an effective material, there are several conditions that have to be fulfilled [80]. First, the periodicity in propagation direction has to be much smaller than the wavelength; otherwise Bragg diffraction may take place and the arrangement is seen as a photonic crystal. Second, the lateral periodicity has also to be smaller than half the wavelength so that only the 0th diffraction order can take place. Finally, since an infinite number of Bloch modes are able to propagate in the periodic composition, the incident wave has to couple predominantly to the fundamental Bloch mode with the lowest propagation loss.

In general, the resulting macroscopic response of a material to incident light is given by the scattering parameters (S-parameters), which relate the incoming and outgoing waves based on their complex amplitudes as follows

$$\begin{pmatrix} \underline{a}_{out,1} \\ \underline{a}_{out,2} \end{pmatrix} = \begin{pmatrix} \underline{S}_{11} & \underline{S}_{12} \\ \underline{S}_{21} & \underline{S}_{22} \end{pmatrix} \begin{pmatrix} \underline{a}_{in,1} \\ \underline{a}_{in,2} \end{pmatrix}. \quad (4.2)$$

$\underline{a}_{in,1}$ and $\underline{a}_{in,2}$ are the amplitudes of the incoming waves at ports 1 and 2, whereas $\underline{a}_{out,1}$ and $\underline{a}_{out,2}$ represent the amplitudes of the outgoing waves at ports 1 and 2. As the S-parameters are also used to express power transmission and reflection, it is common to take the square of the above mentioned coefficients, i.e.

$$|\underline{S}_{ip}| = |\underline{s}_{ip}|^2 \quad \text{with } i, p \in (1, 2). \quad (4.3)$$

In order to determine the internal properties of a metamaterial from its macroscopic response, the retrieval procedure from [81] has to be applied. It should be verified first, however, that the aforementioned homogenization requirements are met before retrieving the internal properties; otherwise unphysical interpretations can be obtained.

Figure 4.3 shows the graphical representation of a normally incident wave at port 1 on a homogeneous and passive material of a thickness d . Because of symmetry, the internal properties can be determined from the S-parameters $\underline{S}_{11} = \underline{S}_{22}$ and $\underline{S}_{21} = \underline{S}_{12}$. These are

$$\begin{aligned} \underline{\varepsilon}_r &= Re(\underline{\varepsilon}_r) - j Im(\underline{\varepsilon}_r), \\ \underline{\mu}_r &= Re(\underline{\mu}_r) - j Im(\underline{\mu}_r), \\ \underline{z} &= \underline{Z} / Z_0 = Re(\underline{z}) - j Im(\underline{z}), \\ \text{and } \underline{n} &= Re(\underline{n}) - j Im(\underline{n}). \end{aligned} \quad (4.4)$$

$\underline{\varepsilon}_r$, $\underline{\mu}_r$, \underline{n} , and \underline{z} are the effective permittivity, permeability, refractive index, and relative impedance respectively. In literature, the minus signs are often replaced by plus signs when the propagating wave is defined by $\vec{\xi}(\vec{r}) = \vec{\xi}_0 e^{-j\omega t} e^{j\vec{k}\vec{r}}$, where $\vec{\xi}$ denotes the corresponding electric or magnetic field vector.

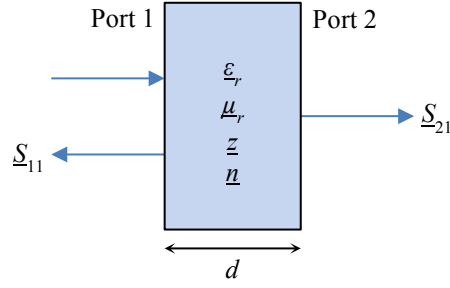


Figure 4.3: Determination of the internal properties of a passive and homogeneous material by retrieving the macroscopic S-parameters.

Assuming normal incidence from free space onto the medium, the S-parameters \underline{S}_{11} and \underline{S}_{21} are given by [82], [83]

$$\underline{S}_{11} = \frac{\Gamma(1 - e^{-j2nk_0d})}{1 - \Gamma^2 e^{-j2nk_0d}} \quad \text{and} \quad \underline{S}_{21} = \frac{(1 - \Gamma^2)e^{-jnk_0d}}{1 - \Gamma^2 e^{-j2nk_0d}}, \quad (4.5)$$

$$\text{with } \Gamma = \frac{\underline{z} - 1}{\underline{z} + 1}. \quad (4.6)$$

Hence, the effective relative impedance is retrieved as follows

$$\underline{z} = \pm \sqrt{\frac{(1 + \underline{S}_{11})^2 - \underline{S}_{21}^2}{(1 - \underline{S}_{11})^2 - \underline{S}_{21}^2}}, \quad (4.7)$$

while the effective refractive index is

$$\underline{n} = \frac{1}{k_0d} \left[\text{Im} \left(\ln \left(e^{-jnk_0d} \right) \right) + 2m\pi + j \text{Re} \left(\ln \left(e^{-jnk_0d} \right) \right) \right], \quad (4.8)$$

$$\text{with } e^{-jnk_0d} = \frac{\underline{S}_{21}}{1 - \underline{S}_{11}\Gamma}. \quad (4.9)$$

The effective permittivity and permeability can then be derived according to

$$\underline{\epsilon}_r = \underline{n} / \underline{z} \quad \text{and} \quad \underline{\mu}_r = \underline{n} \cdot \underline{z}. \quad (4.10)$$

It is clear that the results are not unique due to the square roots of the impedance and the m possible branches originating from the logarithmic term of the refractive index. However, the first ambiguity can be solved by following conditions

$$\text{Re}(\underline{z}) \geq 0 \text{ and } \text{Im}(\underline{n}) \geq 0, \quad (4.11)$$

which are dictated by the material passivity as the energy cannot increase in the medium and the wave has to be damped by the existing losses. Furthermore, the correct branch of $\text{Re}(\underline{n})$ at frequencies well below the resonance can be determined by the requirements $\text{Im}(\underline{\mu}_r) \geq 0$ and $\text{Im}(\underline{\epsilon}_r) \geq 0$, which yield

$$|\text{Re}(\underline{n}) \text{Im}(\underline{z})| \leq \text{Im}(\underline{n}) \text{Re}(\underline{z}). \quad (4.12)$$

This condition is particularly useful in the lower frequency limit when $\text{Im}(\underline{n})\text{Re}(\underline{z}) \approx 0$ and $\text{Im}(\underline{z}) > 0$, which leads to $\text{Re}(\underline{n}) \approx 0$ [82]. Due to the continuity of the material properties, the subsequent branches can then be determined adequately.

4.2. Negative index lenses as nanocouplers

It has been stated that a flat slab of a material with a negative refractive index is able to reproduce subwavelength dimensions which cannot be afforded by diffraction-limited lensing systems [28]. In fact, scattered light at an object comprehends both propagating and evanescent parts with different wave vectors, and hence only the propagating part can attain the focal plane, whereas the evanescent part is damped and lost before reaching the focus [84]. However, negative index materials are able to amplify these decaying waves and restore the image including its fine details. Figure 4.4 illustrates an example of subwavelength focusing using a lossless material slab with $n_2 = -1$ and $d = 2 \mu\text{m}$. The simulation is done using the commercial software RSoft FullWAVE based on the finite-difference time domain (FDTD) method.

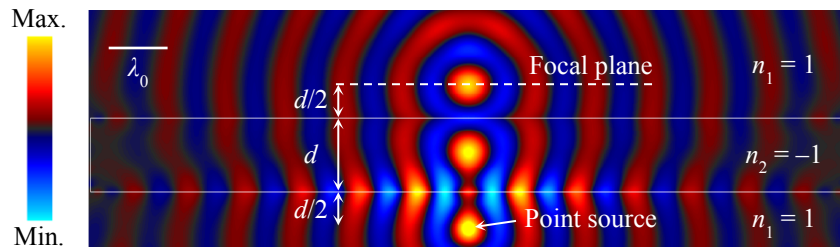


Figure 4.4: Electric field distribution of the perfect negative index material slab at a wavelength $\lambda_0 = 1550 \text{ nm}$.

It is clear that the point source, placed at $d/2$ in front of the slab, is focused at first inside this slab and then perfectly reproduced at the focal plane. The subwavelength focus lies at $d/2$ behind the superlens. However, as focusing using negative index lenses relies on the amplification of evanescent waves inside the slab, these waves suffer again an exponential decay after leaving the material, and hence the effect is limited only to the near field. This is certainly disadvantageous for applications where the focus must not be in the vicinity of the lens such as in real-time microscopy. Therefore, these superlenses are called near-sighted [85] and can only be used in some niche applications such as near field scanning optical microscopes (NSOMs).

In order to focus plane waves into tighter spots, flat lenses are not convenient since negative refraction takes place only at oblique incidence. Thus, a concave shape has to be introduced to the flat negative index material, in contrast to convex lenses made by conventional positive index dielectrics. In general, the focal length F of both configurations with only one shaped face of a curvature radius R_a can be determined by [86]

$$F \approx \left| \frac{R_a}{n-1} \right|. \quad (4.13)$$

Indeed, no subdiffraction focusing of distant sources can be achieved by negative index plano-concave lenses, though sharper foci at lower distances than those using conventional lenses are feasible [29], and this is, therefore, more favorable for compact coupling. It can be seen from (4.13) that for $n > 1$ following relationship is obtained

$$\frac{F(-n)}{F(n)} = 1 - \frac{2}{n+1}, \quad (4.14)$$

i.e. the focal length of a hypothetical medium having a refractive index $-n$ is always smaller than for the positive value case. As dielectric lenses with $n \rightarrow \infty$ may still achieve very compact focusing, the resulting strong reflections certainly prohibit any applicability. Conversely, a negative index lens can be designed to exhibit any index of refraction while being impedance-matched to the surrounding medium, and therefore without any reflections. Since the relative permittivity and permeability can be tuned separately, a lossless negative index material can be matched e.g. to free space by adjusting $\epsilon_r = \mu_r < 0$, which yields $\underline{z} = 1$.

Figure 4.5 shows the focusing ability of a dielectric plano-convex lens having a refractive index $n_+ = 1.5$ versus a plano-concave lens with $\epsilon_r = \mu_r = -1.5$, i.e. a negative index $n_- = -1.5$. Both lenses have a spherical curvature radius $|R_d| = 15 \mu\text{m}$ and a width $w_L = 15 \mu\text{m}$ to focus a fiber Gaussian beam with MFD = $10.4 \mu\text{m}$ at $\lambda_0 = 1550 \text{ nm}$. The simulations are done using RSoft FullWAVE.

In the case of a positive index lens, the focal length is around $22 \mu\text{m}$, whereas it is reduced to only $6 \mu\text{m}$ using a negative index lens, offering more compact focusing as predicted by (4.14). In addition, the beam waist (BW) at the focus, i.e. the beam width where the intensity falls to $1/e^2$ of the maximum value, is decreased from $5 \mu\text{m}$ in the case of the dielectric lens to $1.7 \mu\text{m}$, and hence the beam can be better coupled to integrated waveguides. The reason for this behavior is that the dielectric lens does not focus all rays at the same point and the spot suffers strong elongation, whereas a negative index lens decreases these spherical aberrations and offers a tighter spot [87], [29].

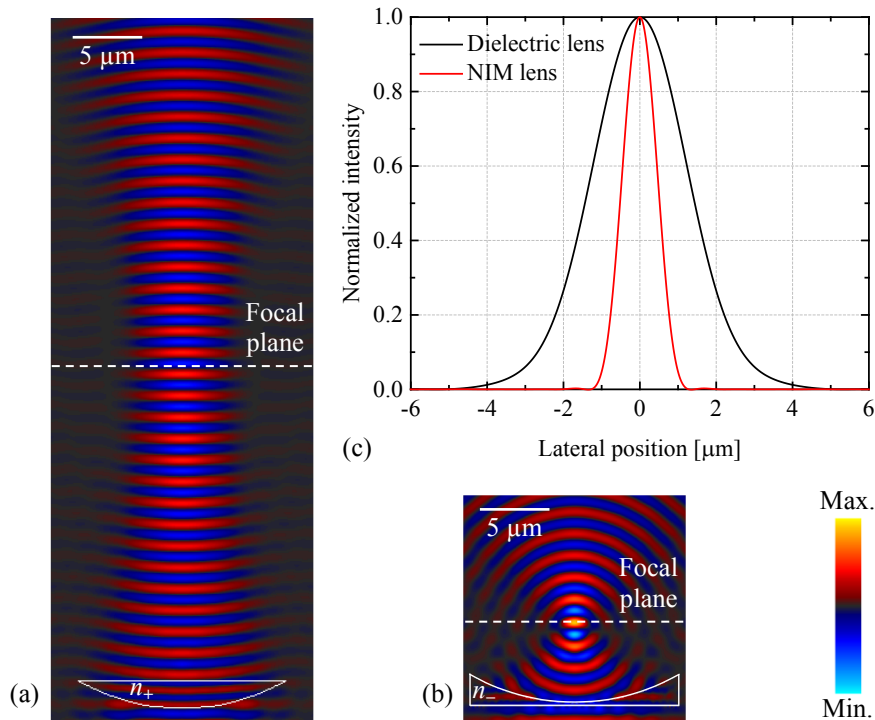


Figure 4.5: Electric field distribution of (a) a plano-convex dielectric lens with $n_+ = 1.5$ and (b) a perfect plano-concave NIM lens with $n_- = -1.5$. Both lenses are placed in free space. (c) Normalized intensity profiles at the corresponding focal plane.

It should be noted that in order to minimize coupling losses, a first-stage waveguide of a width $w \approx \text{BW}$ has to be implemented at the focal plane and then tapered down to the single-mode nanowaveguide. Thus, the smaller the first-stage width is, the more compact the taper length is. This configuration is illustrated in Figure 4.6(a), and the overall coupling efficiency from the fiber to the nanowaveguide, defined as the ratio of the output to the input optical power $\eta = P_{out}/P_{in}$, is given by

$$\eta = T_{\text{NIM}} \cdot \eta_O \cdot T_{\text{WG}} \cdot \eta_T. \quad (4.15)$$

T_{NIM} is the transmission efficiency through the negative index lens, which is affected by the reflection R_{NIM} and absorption losses A_{NIM} of the material as follows

$$T_{\text{NIM}} = 1 - R_{\text{NIM}} - A_{\text{NIM}}. \quad (4.16)$$

η_O is the overlap integral between the electric field profile of the beam at the focal plane E_p and the electric field profile of the guided mode in the first-stage waveguide E_w [62]

$$\eta_O = \frac{\left| \int_A E_p E_w^* dA \right|^2}{\int_A |E_p|^2 dA \int_A |E_w|^2 dA}. \quad (4.17)$$

T_{WG} is the transmission from free space to the waveguide, dictated by the difference of the waveguide refractive index n_{WG} to the free space index n_{air} , which is given for normal incidence by the Fresnel equation

$$T_{\text{WG}} = 1 - \left(\frac{n_{\text{WG}} - n_{\text{air}}}{n_{\text{WG}} + n_{\text{air}}} \right)^2. \quad (4.18)$$

The term η_T is the mode conversion efficiency of the taper that can be approximated by 1 for sufficiently long structures as previously shown. The 2D simulation of the overall coupling efficiency using a lossless negative index lens at 1550 nm is estimated to 64%, which is mainly limited by the Fresnel reflections at the taper interface. Thus, in order to minimize the coupling losses, an antireflection coating (ARC) that eliminates reflection by destructive interference is applied. Using an ARC of a refractive index n_{ARC} and a thickness $d_{\text{ARC}} = \lambda_0/(4n_{\text{ARC}})$, T_{WG} is modified to [25]

$$T_{WG} = 1 - \left(\frac{n_{WG}n_{air} - n_{ARC}^2}{n_{WG}n_{air} + n_{ARC}^2} \right)^2. \quad (4.19)$$

The transmission is then maximized when

$$n_{ARC} = \sqrt{n_{WG}n_{air}}. \quad (4.20)$$

Figure 4.6(b) shows the simulated electric field distribution of the nanocoupling configuration including the previously described lossless negative index plano-concave lens, an ARC layer on the chip interface, and an adiabatic taper. As the configuration is investigated using a simplified 2D simulation, the refractive indices of the taper and the waveguide are changed by their effective values, which are obtained by calculations based on RSoft BeamPROP.

The total length of the coupler between the fiber and the nanowaveguide is only 15 μm , and the overall coupling efficiency reaches 92%. This value, however, is the upper limit that can be achieved since the modal overlap in the third dimension is not considered in addition to the assumption of an ideal plano-concave lens.

It should also be noted that the transmission efficiency is often expressed in dB as

$$\eta_{\text{dB}} = 10 \log_{10}(\eta). \quad (4.21)$$

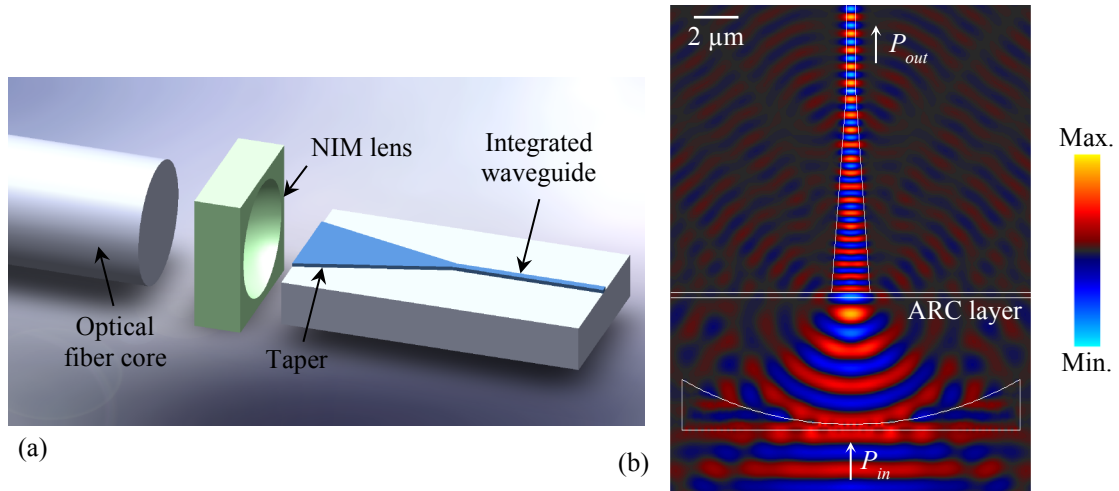


Figure 4.6: (a) Coupling configuration using a NIM lens and an adiabatic taper. (b) 2D simulation of the presented structure with an additional ARC layer on the chip edge.

4.3. Design of negative index metamaterials

In the previous simulations, perfect negative index plano-concave lenses are assumed in order to show their focusing performance and their potential for nanocoupling purposes. The subsequent part deals with the realization of such kind of structures based on concrete negative index materials with the target to achieve high transmission in a broadband frequency range.

The realization of a NIM begins with the design of its primitive constituent: the unit cell. In order to obtain a homogeneous medium with an effective negative refractive index, the unit cells have to feature dimensions in the subwavelength domain. Thus, as the material has to be fabricated for light coupling at a wavelength of 1550 nm, these dimensions have to be a few tens of nanometers. Indeed, the technological process can be challenging and has to be optimized separately to fabricate such structures, but this must not prohibit the investigation of NIMs at higher orders of magnitude. In fact, by scaling up the wavelength by a factor of e.g. 5×10^3 , which corresponds to a value of 7.75 mm, the unit cell dimensions become manageable and the fabrication effort is lessened considerably. Obviously the material properties are not the same in both frequency ranges, and no one-to-one similarities can be assumed, but meaningful deductions can be drawn in the optics from investigations at radio frequencies.

The first task is to design high-performance NIM layers in the Q-band, i.e. at frequencies between 33 GHz and 50 GHz. Afterwards, the single layers are stacked in order to achieve a bulk material, and the focusing performance of the lens is investigated. Thereafter, the structures are fabricated, and the measurement results are compared to the theoretical calculations. Finally, the dimensions are scaled down in order to analyze the resulting behavior at telecommunication wavelengths.

4.3.1. Single layer

There exists a number of unit cell designs starting from the split ring resonators [88] to the cut-wire pairs [89], and fishnet structures [90]. The common feature of all arrangements is the creation of a virtual current loop to produce a magnetic resonance for the negative permeability and making use of the negative permittivity of metallic wires.

Hence, when designing the parameters adequately, a negative refractive index can take place in the overlapping frequency range. The adopted design is based on the polarization-independent fishnet structure proven to exhibit a double-negative behavior, i.e. $Re(\underline{\epsilon}_r) < 0$ and $Re(\underline{\mu}_r) < 0$ simultaneously, with relatively low losses at optical frequencies [91], [92]. The fishnet is slightly modified by introducing an additional parameter in order to optimize its properties with respect to transmission and bandwidth. This special design exhibits a superior performance to standard cross-structures [93] and is graphically represented in Figure 4.7.

The functional layer is composed of 2D periodically arranged unit cells with a period Λ and comprises two thin metallic layers of a thickness d_m separated by a substrate of a thickness d_s . The metallic wires have a width w_m and are arranged perpendicularly to each other, allowing for a polarization-independent behavior. The cylinder of a radius R_m represents an additional degree of freedom in order to tune the impedance of the overall structure. For $R_m \leq w_m / \sqrt{2}$, the effect of the additional cylinder disappears, and the design turns into the well-known fishnet cross-structure.

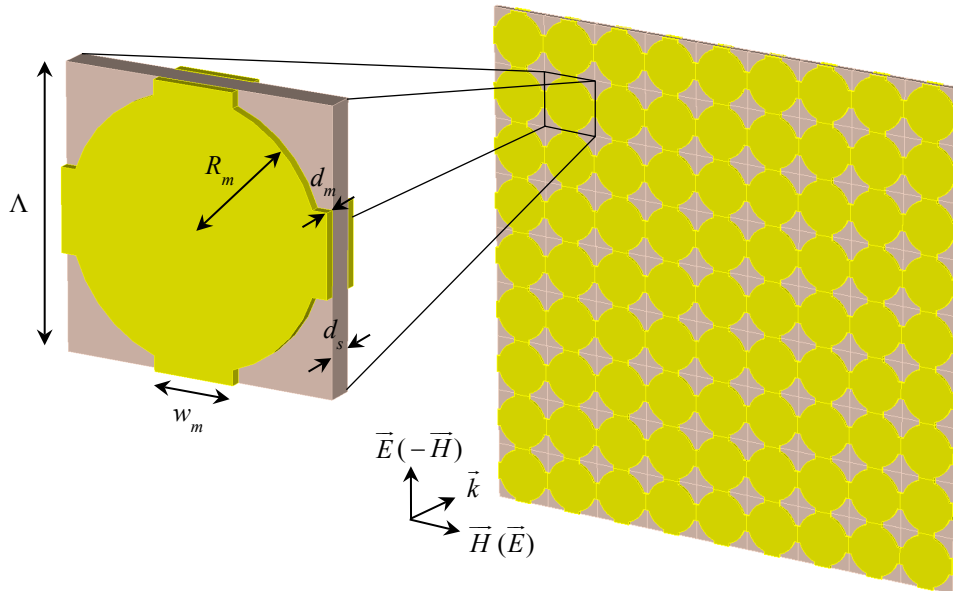


Figure 4.7: Schematic illustration of the functional NIM layer and the elementary cell. Due to symmetry, the design works for arbitrary linear polarizations.

The dielectric material used is RT/duroid 5880 with a thickness $d_s = 250 \mu\text{m}$ and a relative permittivity $\underline{\epsilon}_r = 2.2 \cdot (1 - j0.0009)$ at 10 GHz [94]. The choice of this substrate is based on its low loss at radio frequencies, which plays a major role for designing highly transmissive metamaterials. In addition, the material is laminated with two copper layers with a thickness of $17.5 \mu\text{m}$ each, and thus can be processed by conventional etching techniques.

In order to achieve a magnetic resonance below the plasma frequency of the periodic structure, and hence a negative refractive index in the Q-band, the missing geometrical parameters are determined using the frequency domain solver of the commercial software Computer Simulation Technology (CST) Microwave Studio (MWS). The simulation tool discretizes the geometry using a tetrahedral mesh, solves Maxwell's equations at the corresponding nodes for a given frequency value, and delivers the S-parameters as well as the field distribution of the structure [95]. The corresponding power transmission and reflection coefficients are expressed as $T_{\text{NIM}} = |\underline{S}_{21}|$ and $R_{\text{NIM}} = |\underline{S}_{11}|$ respectively. Computing time is reduced by simulating only a quarter of the unit cell including input and output hollow waveguides with appropriate symmetric boundary conditions [93]. The surrounding walls, furthermore, are set as perfect electric and magnetic conductors, whereas the front and back faces are set as open boundaries for wave excitation. Both waveguides have a length of around λ_0 so that the unit cell is placed in the far field of the excitation ports.

The optimization of the geometrical parameters is based on a set of criterions to limit the number of simulation steps. First, the operating frequency is chosen at 38.5 GHz, around a factor 5×10^3 lower than the telecommunication frequency of 193.55 THz. Second, the retrieved refractive index has to exhibit a value $\underline{n} = -1$ with simultaneously $Re(\underline{\epsilon}_r) < 0$ and $Re(\underline{\mu}_r) < 0$. Finally, high transmission and low reflection properties have to be achieved by impedance matching to free space, i.e. $\underline{z} = 1$. In general, due to the absorption losses in the NIM, which are described by the imaginary part of the refractive index, there exists an additional definition that can be taken into account, called the figure of merit (FOM) [91]. This is defined as

$$\text{FOM} = \frac{|Re(\underline{n})|}{|Im(\underline{n})|}. \quad (4.22)$$

For transmissive applications such as lenses, it is better to extend the expression by multiplying the FOM by the total transmission efficiency since the latter definition quantifies only the absorption and does not deliver any information about the reflection losses [96].

Indeed, there may be several combinations that fulfill the previous conditions. For example, using the parameters $\Lambda = 4.8$ mm, $R_m = 1.8$ mm, and $w_m = 0.3$ mm, the simulated S-parameters show high transmission and low reflection properties with a phase slope change, alluding to a negative refractive index. The amplitude and phase spectra of the S-parameters are depicted in Figure 4.8. At the operating frequency, the transmission is $|\underline{S}_{21}| = -0.05$ dB and the reflection is $|\underline{S}_{11}| = -53.7$ dB, which indicates that the impedance is well matched to free space and that low absorption losses are existent.

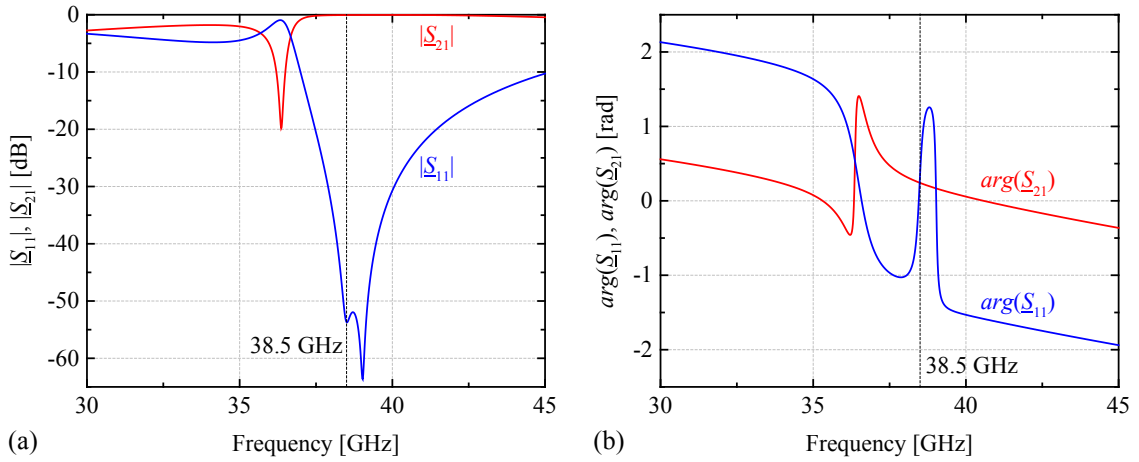


Figure 4.8: Simulated (a) amplitude and (b) phase spectra of the S-parameters of the designed NIM single layer.

The internal properties are determined using the retrieval method previously described and are shown in Figure 4.9. The plasma frequency takes place at 40.19 GHz, whereas the magnetic resonance frequency is 36.45 GHz and the magnetic plasma frequency is 42.18 GHz. Hence, the structure exhibits a double-negative behavior in a large bandwidth of 3.74 GHz. The effective permittivity and permeability are $\underline{\epsilon}_r = -1.04 - j0.017$ and $\underline{\mu}_r = -1.04 - j0.035$ at the operating frequency, and hence the resulting refractive index is $\underline{n} = -1.04 - j0.026$, giving a high FOM of 40.

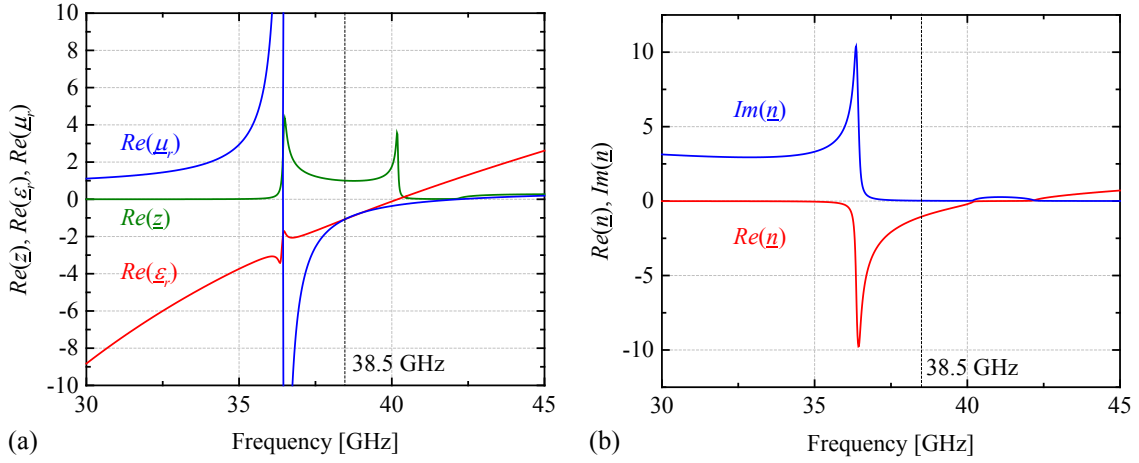


Figure 4.9: Retrieved (a) real part of the relative impedance, permittivity, permeability, and (b) complex refractive index.

While the total thickness of the functional NIM layer $d = d_s + 2d_m$ is in the order of $\lambda_0/27$, the lateral period is much larger and exceeds the value of $\lambda_0/2$; hence, the homogeneity conditions may not be fulfilled to build a bulk material due to possible diffraction effects. By reducing the period, this problem persists since the resonance suffers a shift to higher frequencies so that the requirement $\lambda_0/\Lambda \gg 1$ can never be met using simple fishnet structures. Therefore, the design of simple layers is not sufficient to build a negative index lens, and 3D configurations have to be investigated.

4.3.2. Multilayer

In general, a 3D fishnet NIM can be realized by stacking N functional layers with a spacer separating each two consecutive layers. Using the previously presented structure, a NIM stack with $N = 10$, including air spacers of a thickness $d_{sp} = 0.5$ mm each, is simulated. Figure 4.10(a) illustrates the retrieved refractive index of the multilayer.

It is clear that the behavior is completely different from that of a single layer, and instead of a negative refractive index, positive values are obtained. In fact, the additional spacers cause the decrease of the plasma frequency well below the magnetic resonance such that no overlapping range exists to constitute a negative index. While retrieving the multilayer properties is not trivial due to the several possible solutions of $Re(\underline{n})$, the phase advance inside the metamaterial can indicate whether the wave is forward or backward propagating. The electric field distribution at the stack cross section at the

operating frequency is shown in Figure 4.10(b). In this case, the phase velocity and the energy flow propagate in the same direction, and thus the metamaterial is right-handed and exhibits a positive index of refraction.

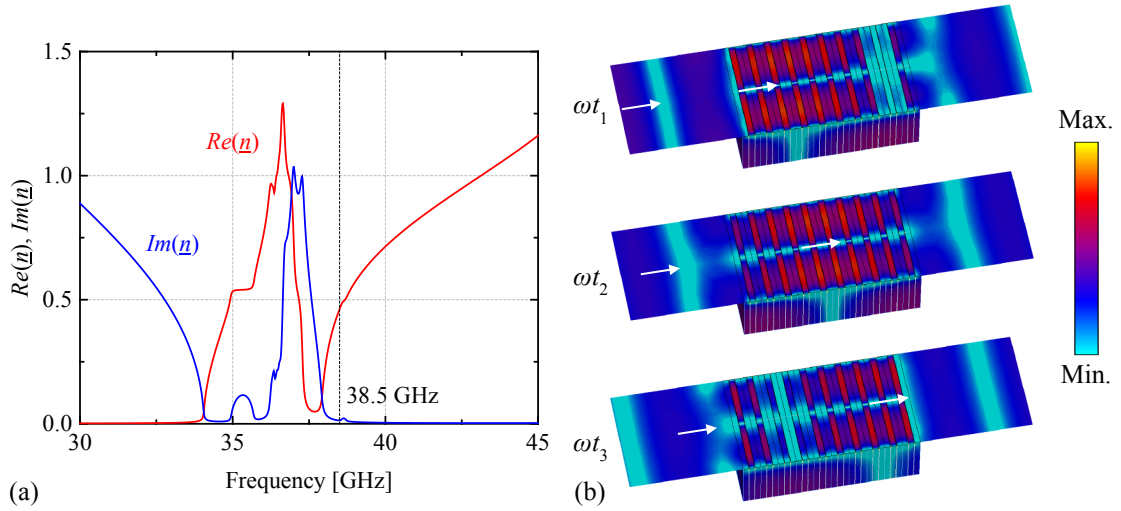


Figure 4.10: (a) Retrieved refractive index of the simulated multilayer. (b) Electric field distribution at 38.5 GHz at three consecutive phase values $\omega t_1 < \omega t_2 < \omega t_3$.

The conclusion that can be drawn from the latter results is that a multilayer does not necessarily behave like a single layer, and hence it is better to optimize the 3D stack despite the considerable computing expenses. Alternatively, the complete system, i.e. the plano-concave NIM lens, can be optimized rather than the flat design; however, this requires even more computational effort. This is in general a trade-off between the available resources and the required properties. The reason for the large difference between $N = 1$ and $N = 10$ is that additional coupling between the functional layers influences the overall response of the structure. Furthermore, the presence of several propagating Bloch modes in the periodic stack may make the retrieval of the internal properties meaningless since no effective parameters may be assigned to the material [96].

The optimization of the ten-layer structure, including the air spacers, is realized in a similar way to the single layer using the procedure described in the previous subsection. The stack obtained has the parameters $\Lambda = 5$ mm, $R_m = 2.2$ mm, and $w_m = 1.8$ mm and is illustrated in Figure 4.11(a). However, the transmission is low and attains -4.5 dB at

38.5 GHz with a 1 dB bandwidth smaller than 0.2 GHz due to the impedance mismatch as shown in Figures 4.11(b) and 4.11(c). In fact, the spacer produces a weak coupling between the individual layers, and the wave is predominantly absorbed or reflected. In addition, the magnetic resonance is relatively weak, and the retrieved permeability is negative in a narrow bandwidth of 1 GHz, reaching $\underline{\mu}_r = -0.54 - j0.39$ at the operating frequency, whereas the permittivity is $\underline{\epsilon}_r = -1.04 + j0.47$. Hence, the refractive index, shown in Figure 4.11(d), is $\underline{n} = -0.87 - j0.087$, giving a low FOM of 10.

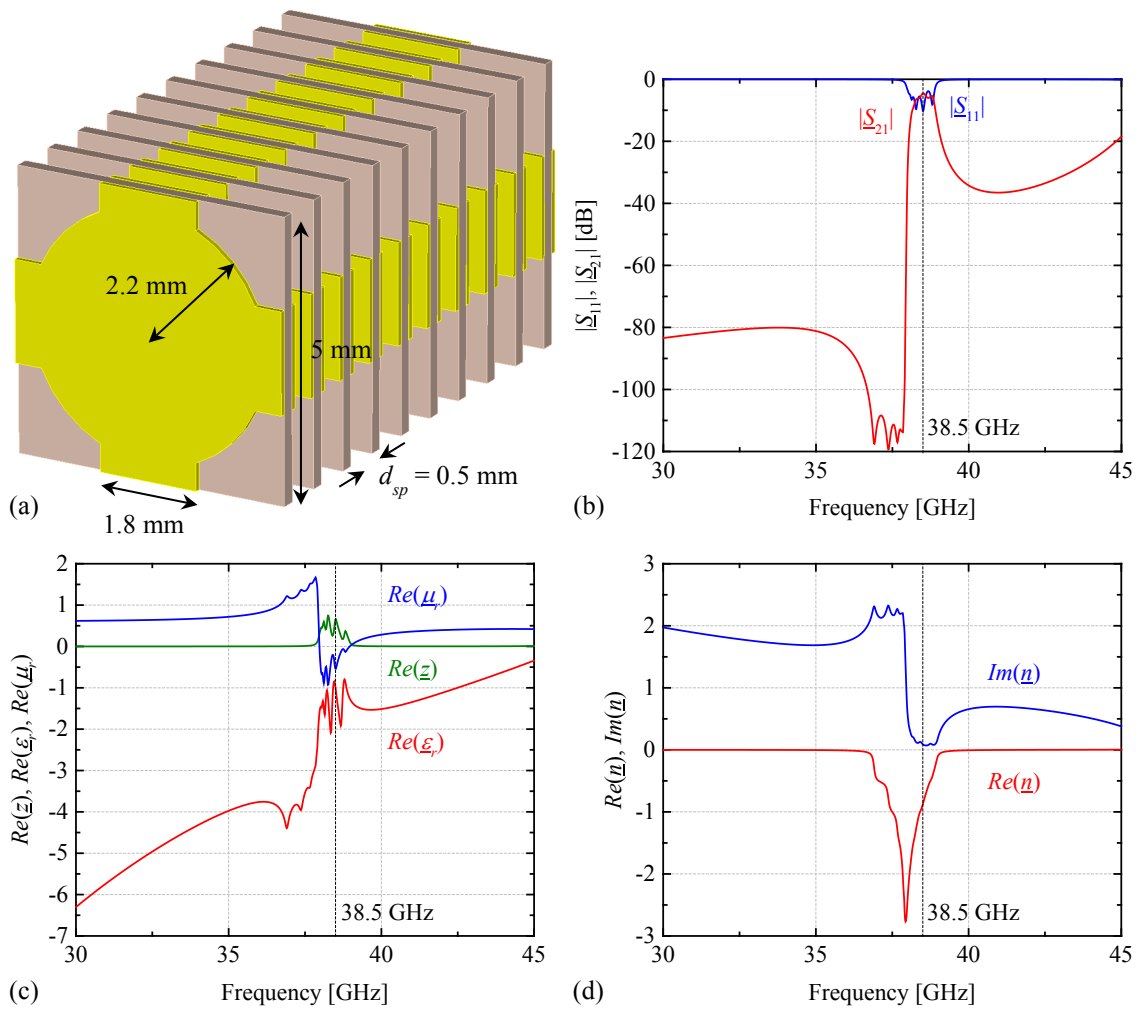


Figure 4.11: (a) Unit cell of the weakly coupled multilayer. (b) Simulated S-parameters of the stack. Retrieved (c) real part of the relative impedance, permittivity, permeability, and (d) complex refractive index.

In order to achieve a strong coupling between the layers and a higher transmission, the spacer is removed and the stack is optimized again. The parameters of the obtained

structure are $\Lambda = 4.9$ mm, $R_m = 2.3$ mm, and $w_m = 1.45$ mm. Figure 4.12 shows the simulated ten-layer stack and the corresponding properties. In this case, as a consequence of the good impedance matching, the transmission and reflection at 38.5 GHz are $|\underline{S}_{21}| = -0.56$ dB and $|\underline{S}_{11}| = -26.77$ dB, and the 1 dB bandwidth is increased to more than 0.8 GHz. Furthermore, the permittivity and permeability are $\underline{\epsilon}_r = -1.04 + j0.025$ and $\underline{\mu}_r = -0.96 - j0.077$, giving rise to a refractive index $\underline{n} = -0.997 - j0.0275$. Additionally, the structure is double-negative in a bandwidth larger than 3.5 GHz, and the resulting FOM is higher than 36 at the target frequency, which reflects the high performance of the NIM stack. Therefore, this structure is used for further investigations and for the realization of the plano-concave lens.

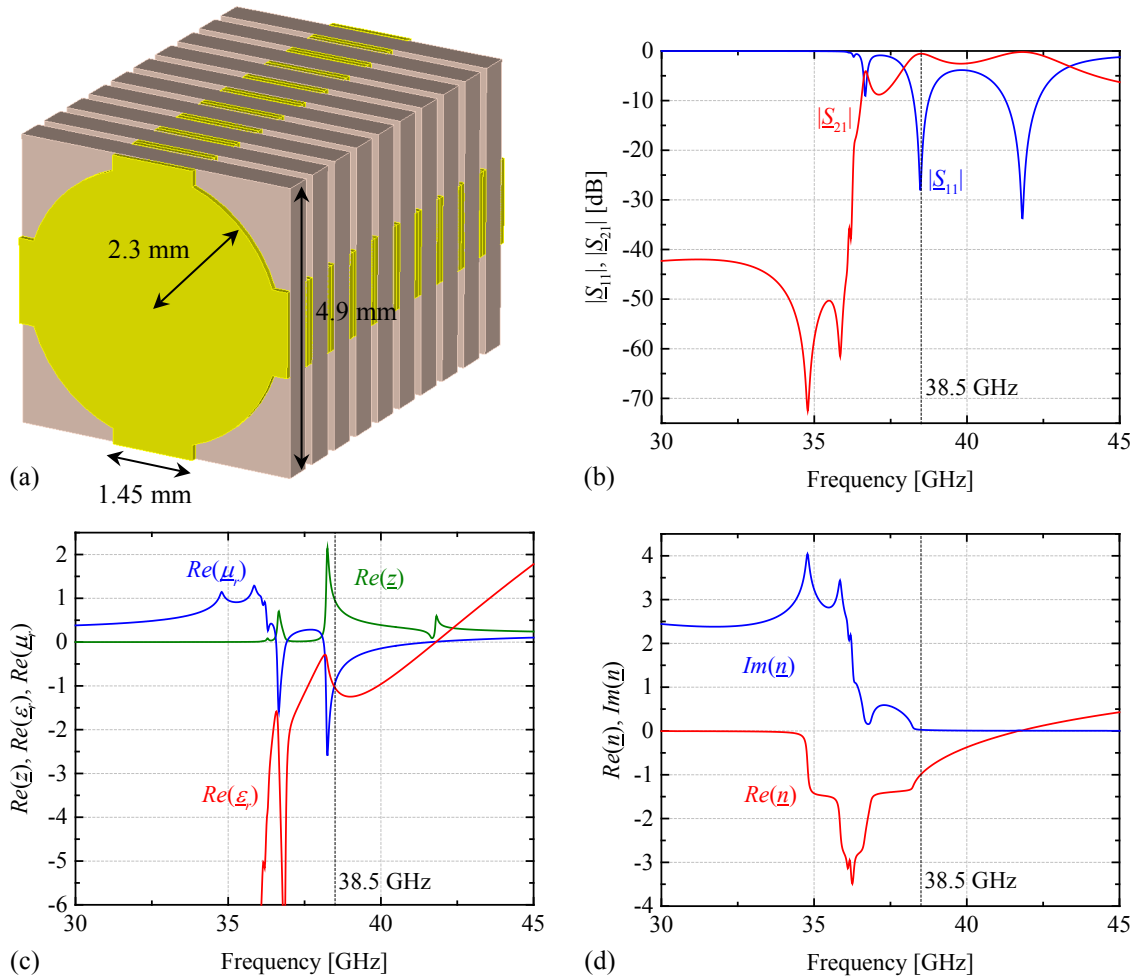


Figure 4.12: (a) Unit cell of the strongly coupled multilayer. (b) Simulated S-parameters of the stack. Retrieved (c) real part of the relative impedance, permittivity, permeability, and (d) complex refractive index.

It should be noted that the transmission of the stack can be further increased by reducing the metal width as in the case of a single layer, but unphysical discontinuities in the retrieved parameters appear, alluding to the propagation of more than one Bloch-mode [96]. These higher-order modes can certainly be damped by introducing more losses to the structure; however, this affects the fundamental mode as well. Thus, there is also a trade-off between the homogeneity principle and the required transmission.

The phase advance inside the metamaterial is also investigated to verify the wave propagation behavior. The corresponding electric field distribution across the stack is shown in Figure 4.13(a). It is clear that there is a backward propagating wave with a phase advance opposing the energy flow, and hence the structure exhibits a negative refractive index. Furthermore, the effect of stacking more layers is inspected since the NIM lens requires the variation of N to obtain the plano-concave shape. Figure 4.13(b) shows the retrieved $Re(\underline{n})$ obtained by the frequency domain solver for $N = 1$ up to $N = 20$ and by the eigenmode solver of CST MWS corresponding to $N \rightarrow \infty$. Due to the strong coupling between the functional layers, the convergence is slow, and hence the behavior depends on N in contrast to the weakly coupled case [97]. At 38.5 GHz, the value of $Re(\underline{n})$ decreases from -1 for $N = 10$ to -0.68 for $N = 20$, which may shift away the focus of the plano-concave lens in contrast to conventional NIM GRIN lenses where the refractive index is radially increased [74], [87].

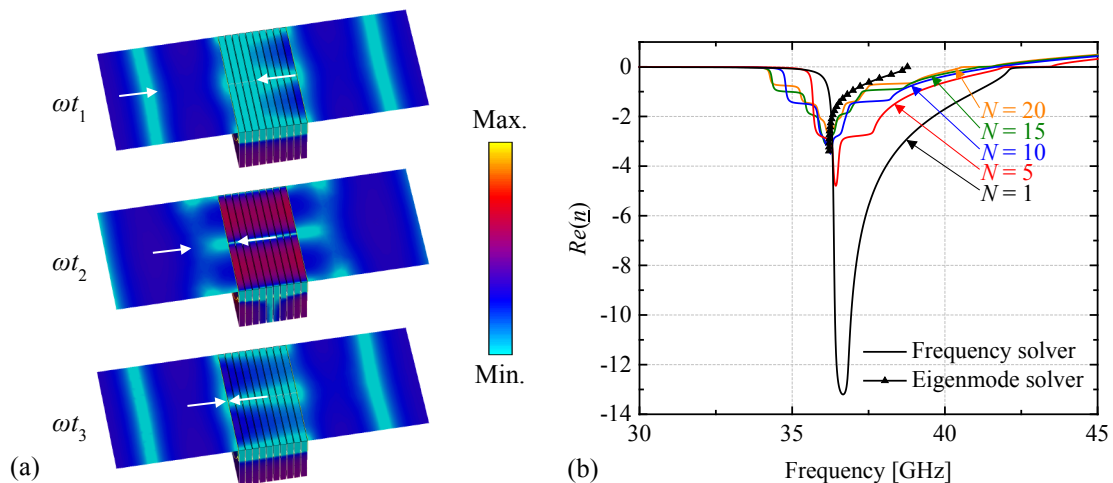


Figure 4.13: (a) Electric field distribution of the strongly coupled multilayer at 38.5 GHz at three consecutive phase values $\omega t_1 < \omega t_2 < \omega t_3$. (b) Retrieved $Re(\underline{n})$ of the NIM for different numbers of layers.

4.3.3. Focusing ability of the designed metamaterial

In order to verify the focusing ability of the plano-concave lens based on the designed NIM, the shape of one side is modified by varying the number of layers from $N = 10$ to $N = 21$ following a spherical surface of a radius $R_a = 75$ mm. This represents a magnification of the analyzed perfect negative index lens in chapter 4.2 by a factor of 5×10^3 . Figure 4.14 shows the approximated step form of the lens and the simulation setup. The concrete sample to be fabricated represents a rotational symmetry of this elementary section around the y -axis. To reduce the computational effort, only a quarter of the design is simulated with appropriate symmetric boundary conditions as previously discussed. A waveguide port of a width 11Λ with a BW of around $5 \lambda_0$ is used to launch a plane wave at 38.5 GHz at a distance of $2 \lambda_0$ from the NIM flat surface. The electric field distribution is obtained using CST MWS.

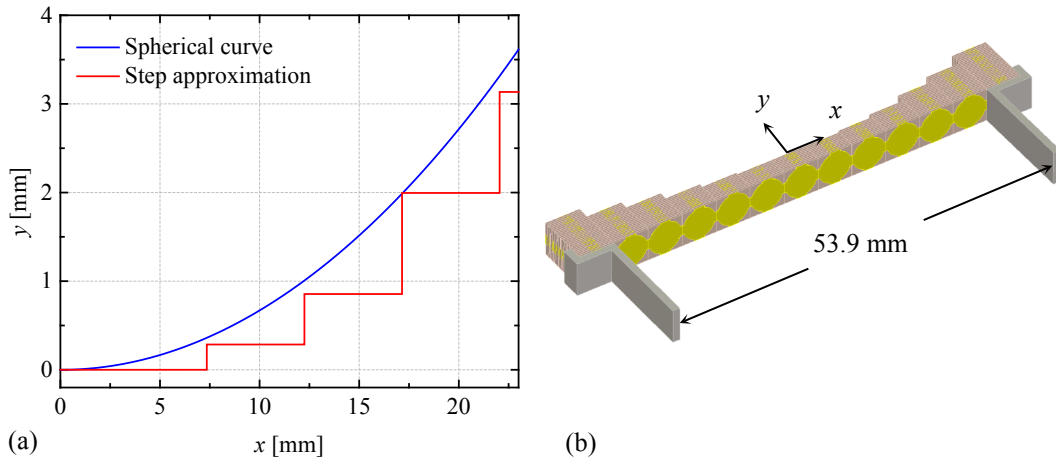


Figure 4.14: (a) Spherical curve using a radius $R_a = 75$ mm and approximated concave shape of the designed NIM lens. (b) Schematic illustration of the simulation setup including the input waveguide port.

The electric field distribution of the simulated NIM lens versus free space is depicted in Figure 4.15. The front focal length (FFL), i.e. the distance between the focus and the vertex of the lens at $x = y = 0$ mm, is 44.8 mm, and the transmission at the focal point is 4.2 dB better than in free space. The slightly higher focal length than predicted is due to the dependence of the refractive index on the number of layers in each section as previ-

ously discussed. The BW of the focused spot is 14 mm, which corresponds to a reduction of the launched beam width by a factor of 2.8.

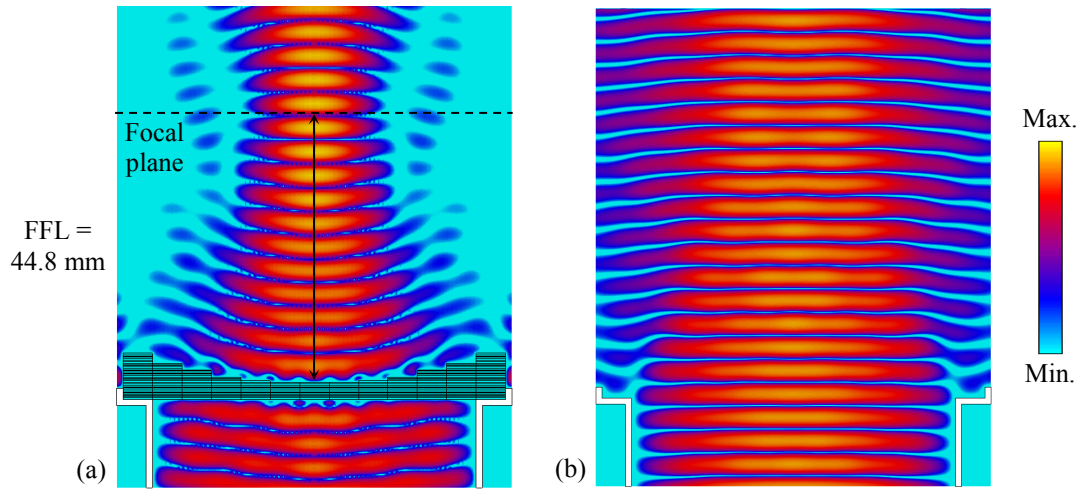


Figure 4.15: Electric field distribution (a) of the NIM lens and (b) in free space at 38.5 GHz.

4.4. Characterization of the internal properties

In order to realize the plano-concave NIM lens, the functional layers with the parameters $\Lambda = 4.9$ mm, $R_m = 2.3$ mm, and $w_m = 1.45$ mm are fabricated based on conventional etching techniques at Elekonta. The samples, with dimensions of 20×20 unit cells, are then characterized individually to verify the reproducibility of the functional layer response. Thereafter, the layers are stacked on top of each other without spacers to form a strongly coupled NIM as illustrated in Figure 4.16, and the stack is characterized to determine the internal properties.

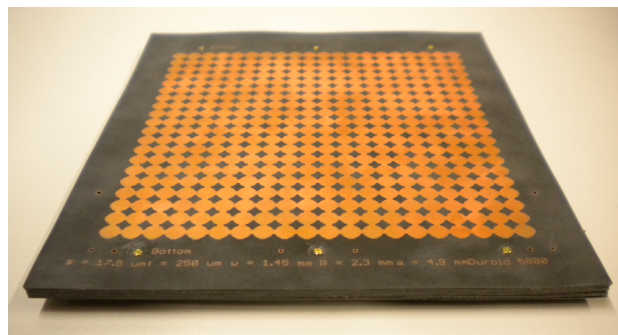


Figure 4.16: Picture of the fabricated strongly coupled fishnet NIM stack.

4.4.1. Measurement setup

Similar to the simulations, the internal properties of the fabricated NIM structures are determined from the macroscopic response by retrieving the complex S-parameters. For this purpose, a measurement setup based on a vector network analyzer and two Q-band horn antennas is used as shown in Figure 4.17.

To eliminate the additional losses of the high-frequency cables, adapters, and antennas, the setup is calibrated using the thru-reflect-match (TRM) method. The calibration is also important to measure the correct phase behavior of the S-parameters. The “thru” standard represents the free space distance without any sample between the antennas, whereas the “reflect” is operated by placing a metal plate between the space separating the antennas. The “match” standard is done by isolating the antennas from the surrounding environment using absorber materials so that neither reflection nor transmission takes place [93].

After calibrating the setup, the NIM sample is positioned in the middle between the antennas, and the S-parameters are measured at frequencies from 30 GHz to 45 GHz. It should be noted that the measured phases must subsequently be deembedded since the wave encounters an additional phase shift of π after being reflected at the metal plate during calibration, whereas the phase of the transmission coefficient includes a value of k_0d , corresponding to the sample thickness in free space.

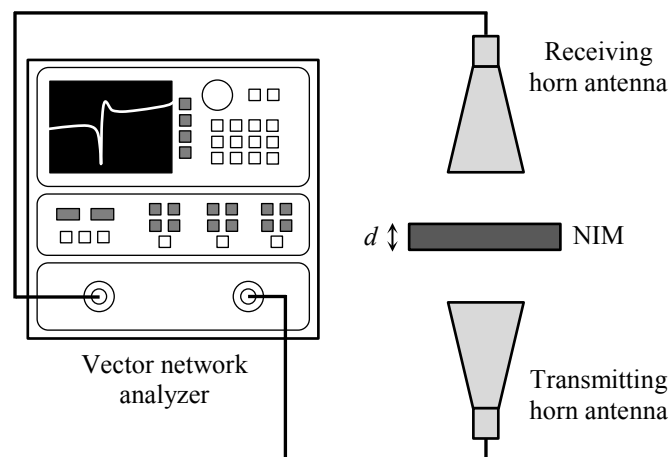


Figure 4.17: Graphical representation of the used measurement setup to determine the S-parameters of the fabricated NIM samples.

4.4.2. Measured S-parameters and retrieved properties

Figure 4.18(a) shows a comparison between the simulated and measured amplitude of the S-parameters of a single layer. Both results are in good agreement, except for the ripples caused by resonant Fabry-Pérot reflections. The FSR amounts to 0.4 GHz and yields a resonator length of 37.5 cm, which corresponds to the distance between the horn antennas. At 37 GHz, a clear passband with a transmission peak of -1.47 dB is observed and originates from the negative index behavior of the fishnet layer. This value is slightly higher than in the simulation and can be attributed to the lower substrate losses than assumed. The second passband takes place at frequencies higher than 45 GHz where the refractive index tends toward positive values.

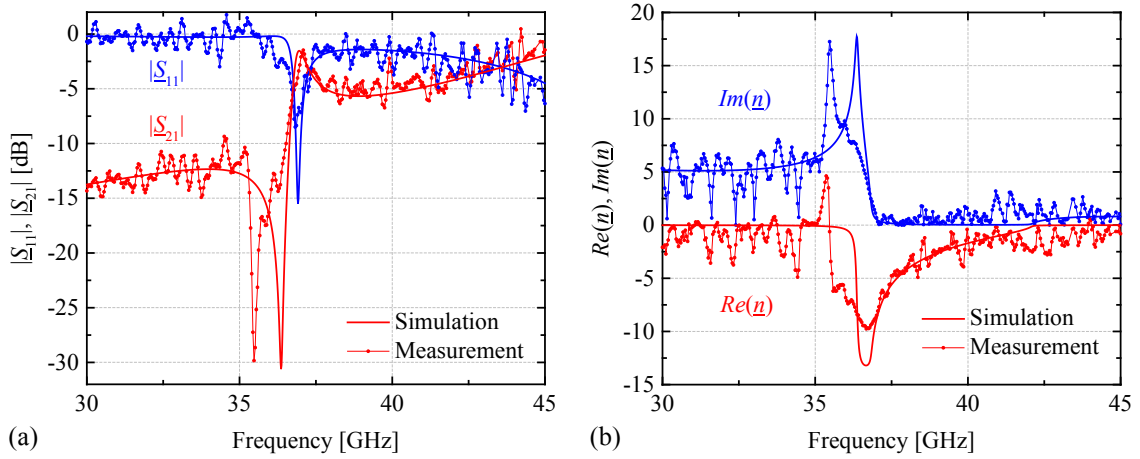


Figure 4.18: (a) Simulated and measured amplitude of the S-parameters of a single layer with $\Lambda = 4.9$ mm, $R_m = 2.3$ mm, and $w_m = 1.45$ mm. (b) Retrieved refractive index of the structure.

As the impedance matching condition is optimized for $N = 10$, the single layer does not exhibit optimal performance with regard to transmission and reflection characteristics. The retrieved refractive index illustrated in Figure 4.18(b) also agrees with the simulation and shows a large bandwidth where $Re(\underline{n}) < 0$. It should be noted that the structure is not double-negative between 35.5 GHz and 36.6 GHz despite $Re(\underline{n}) < 0$. In fact, the condition $Re(\underline{\epsilon}_r) < 0$ and $Re(\underline{\mu}_r) < 0$ is sufficient but not necessary to obtain a negative refractive index. According to [98], the strict requirement for $Re(\underline{n}) < 0$ is

$$\text{Re}(\underline{\epsilon}_r) \text{Im}(\underline{\mu}_r) + \text{Re}(\underline{\mu}_r) \text{Im}(\underline{\epsilon}_r) < 0, \quad (4.23)$$

and thus a negative permittivity with high permeability losses can deliver a negative index of refraction. The strongly absorptive characteristic of the structure in the corresponding frequency range, however, limits its use for transmissive applications.

Figure 4.19(a) depicts a comparison between the simulated and measured amplitude of the S-parameters of the ten-layer stack. The transmission reaches -0.47 dB at 38.5 GHz and is also slightly higher than the simulated value of -0.56 dB, whereas the reflection is -10.5 dB. The 1 dB bandwidth is evidently lower than the theoretical value of 0.8 GHz but cannot be adequately determined due to the additional Fabry-Pérot resonances.

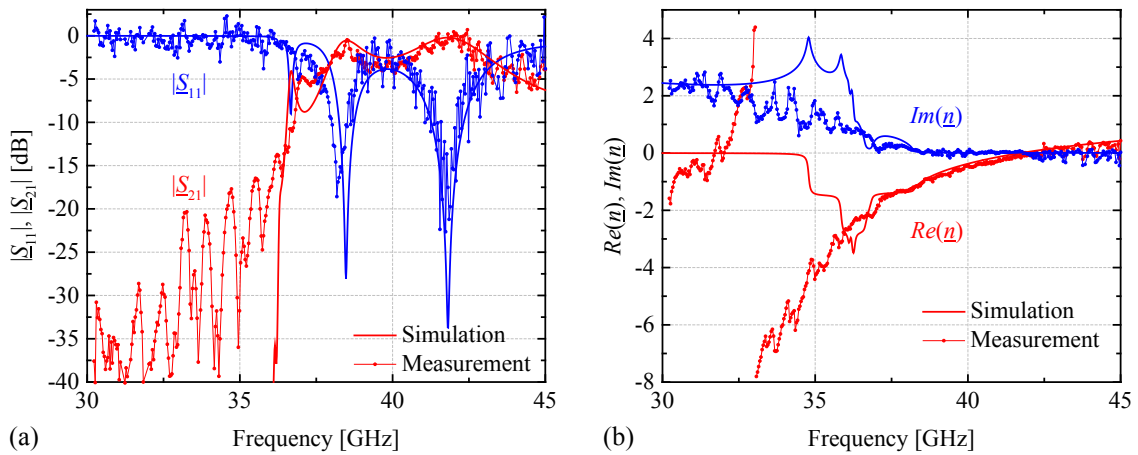


Figure 4.19: (a) Simulated and measured results of the amplitude spectra of the S-parameters and (b) corresponding retrieved refractive index of the multilayer.

Interestingly, the retrieved refractive index illustrated in Figure 4.19(b) shows a discontinuity at around 33 GHz in contrast to the theoretical calculations. The discrepancy may originate from the propagation of higher-order Bloch modes, which are not sufficiently damped in the fabricated multilayer due to the lower losses than assumed as it can also be observed from the retrieved $\text{Im}(\underline{n})$. In this case, the homogeneity condition in the corresponding frequency range is violated, and no effective parameters can be assigned to the material; hence, the internal properties are not meaningfully retrieved from the macroscopic response. By introducing more losses, for example using a larger

metal width, the higher-order Bloch modes may degenerate and the discontinuity can then be eliminated; however, the fundamental mode is affected as well, and the overall transmission is reduced. At the operating frequency, the measured refractive index is $Re(\underline{n}) = -1.03$ and the imaginary part is lower than 0.01. The latter value cannot be determined adequately as well due to the ripples around zero produced by the Fabry-Pérot resonances.

In order to verify the negative index behavior of the designed metamaterial, especially at the operating frequency, another method based on the phase-thickness relationship is used. As the phase of the transmission coefficient is $arg(\underline{S}_{21}) = -kd$, the real part of the refractive index can be determined from

$$Re(\underline{n}) = -\frac{1}{k_0} \frac{\partial arg(\underline{S}_{21})}{\partial d}, \quad (4.24)$$

with k_0 the wave number in free space. Indeed, the exact value of $Re(\underline{n})$ for a strongly coupled stack cannot be calculated from the latter equation since it depends on the number of layers, but the sign of the refractive index can be estimated. Figure 4.20 shows the phase spectrum of three structures with different numbers of layers. It is clear that $arg(\underline{S}_{21})$ increases with increased thickness at frequencies up to nearly 40.5 GHz, alluding to $Re(\underline{n}) < 0$, whereas the behavior is inverted at higher frequencies with $Re(\underline{n}) > 0$. Hence, the fabricated metamaterial exhibits a negative refractive index at the operating frequency 38.5 GHz.

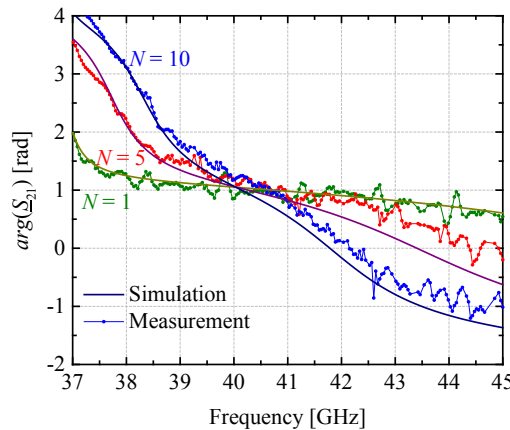


Figure 4.20: Simulated and measured phase spectra of \underline{S}_{21} of the strongly coupled NIM structure with different numbers of layers.

4.5. Focusing ability of the fabricated metamaterial

The fabricated metamaterial stack is extended by eleven layers of different aperture sizes to form a plano-concave lens as described in subsection 4.3.3. The number of layers varies from $N = 10$ in the middle of the lens to $N = 21$ at the edge following an approximate spherical curvature of a radius $R_a = 75$ mm. The realized structure is depicted in Figure 4.21.

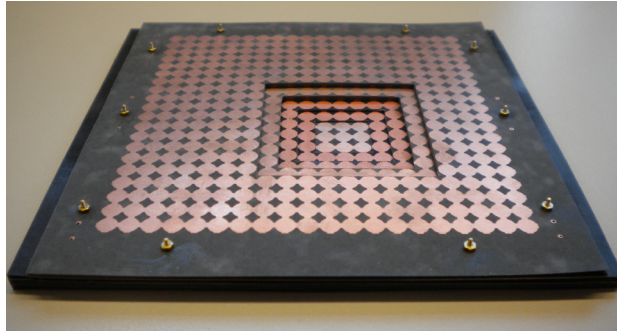


Figure 4.21: Picture of the fabricated plano-concave NIM lens. The smallest and largest apertures have the dimensions $3 \Lambda \times 3 \Lambda$ and $9 \Lambda \times 9 \Lambda$ respectively.

4.5.1. Measurement setup

In order to scan the transmitted field distribution of the plano-concave NIM lens and to verify its focusing ability, the measurement setup presented in 4.4.1 is modified accordingly. The receiving horn antenna is replaced by an open-ended waveguide (OEWG) antenna with the cross-sectional dimensions of $5.7 \text{ mm} \times 2.85 \text{ mm}$ and a length of 100 mm . The chosen width and height correspond to the dimensions of a standard Q-band rectangular waveguide [99]. This antenna is mounted on an xy -table composed of two microstep linear stages, which are operated by an automated motion controller, and serve to scan the field with a resolution of $\Delta x = \Delta y = 0.5 \text{ mm}$. At the sender side, the horn antenna with the cross-sectional dimensions of $55 \text{ mm} \times 41 \text{ mm}$ is positioned at $4 \lambda_0$ from the flat face of the plano-concave lens. The transmitted beam from the horn antenna can be approximated by a Gaussian function with a BW broadening of the form [100]

$$BW(y) = 2w_0 \sqrt{1 + \left(\frac{\lambda_0 y}{\pi n w_0^2} \right)^2}, \quad (4.25)$$

where $2w_0 \approx 40$ mm is the measured beam diameter at the initial position $y = 0$ mm, λ_0 is the wavelength in free space, and n is the refractive index of the surrounding medium – in this case air. Thus, the input beam width at the NIM interface amounts to nearly 41 mm and corresponds to the core diameter of an SMF when scaling the dimensions down by a factor of 5×10^3 . Figure 4.22 illustrates the used measurement setup.

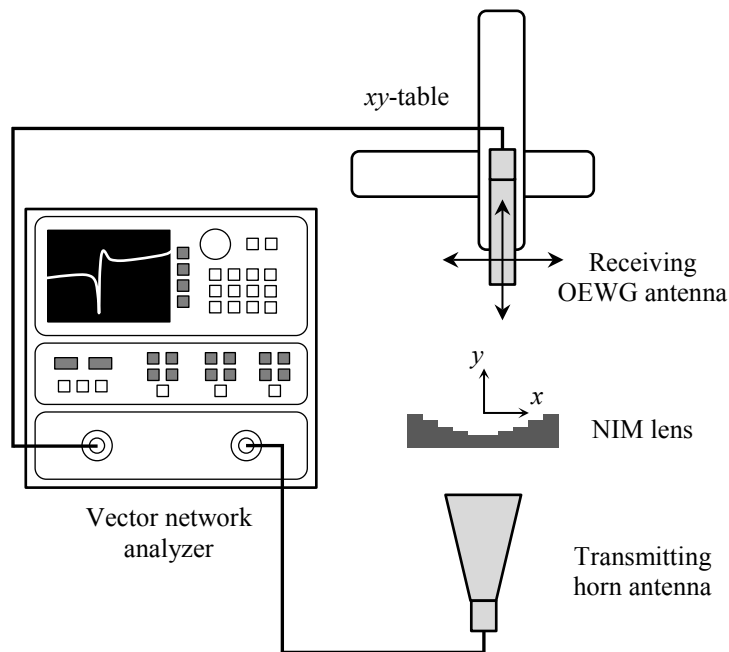


Figure 4.22: Graphical representation of the measurement setup to scan the transmitted field distribution of the fabricated NIM lens.

4.5.2. Measured field distribution and focus position

The measured values of $|S_{21}|$ at different positions behind the NIM lens are mapped in Figure 4.23(a). The plane $y = 0$ mm lies in the vicinity of the concave interface. The highest transmission takes place at $y = 44$ mm and is in perfect agreement with the simulation results. The relatively weak side lobes originate from diffraction at the periodic unit cells and do not considerably limit the focusing ability of the NIM. When the lens is removed, the beam diverges as shown in Figure 4.23(b), and the transmission at the focus position deteriorates by around 7 dB.

The normalized NIM transmission profile at the focal plane is illustrated in Figure 4.23(c) and shows good agreement with the simulated result as well. The BW of the measured focus is 18.3 mm, which corresponds to a reduction of the launched beam width by a factor of 2.2. Hence, the fabricated structure exhibits a clear focusing ability and high transmission characteristics, which can exceed the performance of conventional lenses.

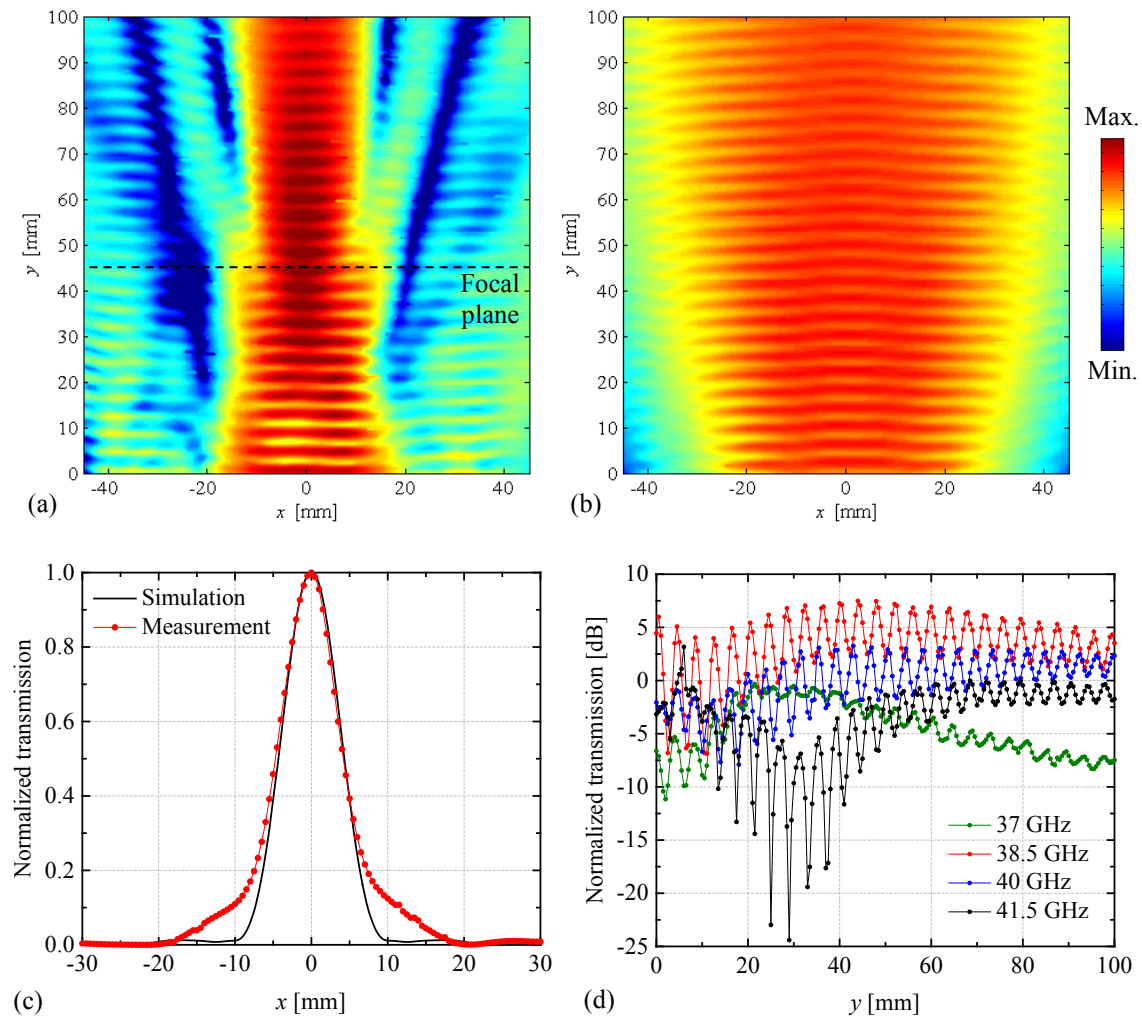


Figure 4.23: Measured transmission distribution at 38.5 GHz (a) using the fabricated plano-concave NIM lens and (b) in free space. (c) Comparison between the simulated and measured NIM intensity profiles at the focal plane. (d) Measured NIM transmission along the y -direction at $x = 0$ mm with respect to free space at different frequencies.

The focusing behavior of the NIM along the y -direction is also investigated at different frequencies as can be seen in Figure 4.23(d). Here the transmission at $x = 0$ mm is normalized to free space for each considered frequency. At 37 GHz, the lens shows a clear focus at $y = 21.5$ mm owing to the large negative refractive index, but with a low transmission, due to the high absorption losses as previously described. At the target frequency 38.5 GHz, the structure exhibits a gain larger than 7 dB with an increased focal plane distance, and at 40 GHz the transmission decreases again with a still apparent focus. At around 41.5 GHz, the focusing ability of the NIM vanishes as the refractive index tends toward zero, while at higher frequencies the beam is diverged by the plano-concave configuration since the metamaterial exhibits an effective positive index of refraction.

In order to emphasize the advantages of the investigated NIM structure, a standard dielectric plano-convex lens is also designed, fabricated, and characterized. This lens is based on a Teflon substrate of a relative permittivity $\epsilon_r = 2.1 \cdot (1 - j0.0002)$ at 10 GHz [101] and has a hyperbolic surface – described in appendix C – in order to eliminate any spherical aberrations. The fabricated dielectric lens has a diameter $D = 72$ mm and is illustrated in Figure 4.24(a).

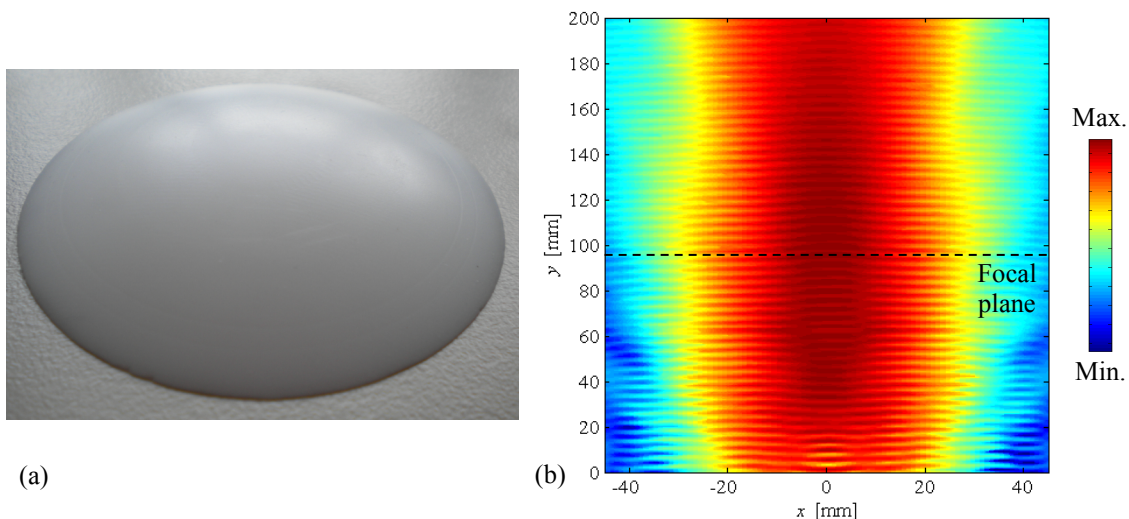


Figure 4.24: (a) Picture of the fabricated plano-convex dielectric lens. (b) Measured transmission distribution of the lens at 38.5 GHz.

The transmission distribution of the lens is recorded using the above described measurement setup and is depicted in Figure 4.24(b). The focus takes place at nearly 95 mm from the lens interface with 0.4 dB lower transmission and a much larger width than using the NIM structure. In fact, the BW at the focal plane amounts to 38.6 mm and is twice larger than in the case of the NIM lens. Hence, the fabricated plano-concave NIM lens exhibits better focusing characteristics than its dielectric counterpart with a tighter beam spot at the focal plane and an FFL reduced by a factor of two.

4.6. Negative index metamaterials at optical frequencies

The outperforming properties of the fabricated NIM and the promising focusing ability of the plano-concave lens at radio frequencies are demonstrated in the previous sub-chapter. As the coupling issue between optical fibers and integrated nanowaveguides occurs at telecommunication wavelengths, it is essential to investigate the behavior of the proposed fishnet design at optical frequencies. Hence, the dimensions of the unit cell are downsized by a factor of 5×10^3 to operate at a frequency of 193.55 THz.

While the choice of the dielectric substrate does not represent a major difficulty, the metallic material may be decisive for the behavior of the whole structure. In fact, metals exhibit high losses at optical frequencies and can limit the practicability of metamaterials, especially in the case of transmissive applications such as lensing systems. It is known that silver (Ag) has the lowest losses compared to the other conventional metals, e.g. gold or copper, and has the strongest magnetic resonance when using fishnet metamaterials [102]. It is hence chosen for further investigations.

Following the simulation approach adopted in the previous section, a multilayer based on the modified fishnet design with $N = 5$ is optimized. The unit cell is composed of two metallic layers of a thickness $d_m = 60$ nm each separated by a substrate of a thickness $d_s = 40$ nm. The dielectric is assumed as lossless and has a relative permittivity $\epsilon_r = 2.2$, whereas the frequency-dependent behavior of Ag is described by the Drude model with the plasma angular frequency $\omega_p = 1.37 \times 10^{16}$ rad/s and the damping coefficient $\gamma = 8.5 \times 10^{13}$ /s [103]. The geometrical parameters of the obtained unit cell are $\Lambda = 640$ nm, $R_m = 224$ nm, and $w_m = 30$ nm. As the retrieved properties show unphysi-

cal discontinuities in the case of strong coupling, an additional spacer of an optimal thickness of 80 nm is introduced.

The amplitude of the simulated S-parameters and the retrieved $Re(\underline{n})$ of the structure in comparison with a fewer number of layers are shown in Figure 4.25. At the operating frequency, the transmission of the stack with $N = 5$ is -11.6 dB, which is 9.6 dB lower than in the case of a single layer. While the transmission is not limited at frequencies higher than 193.55 THz, it drastically decreases at lower values. The retrieved refractive index of the multilayer and the single layer is $\underline{n} = -0.32 - j0.31$ and $\underline{n} = -0.94 - j0.39$, which corresponds to a FOM of 1 and 2.4 respectively.

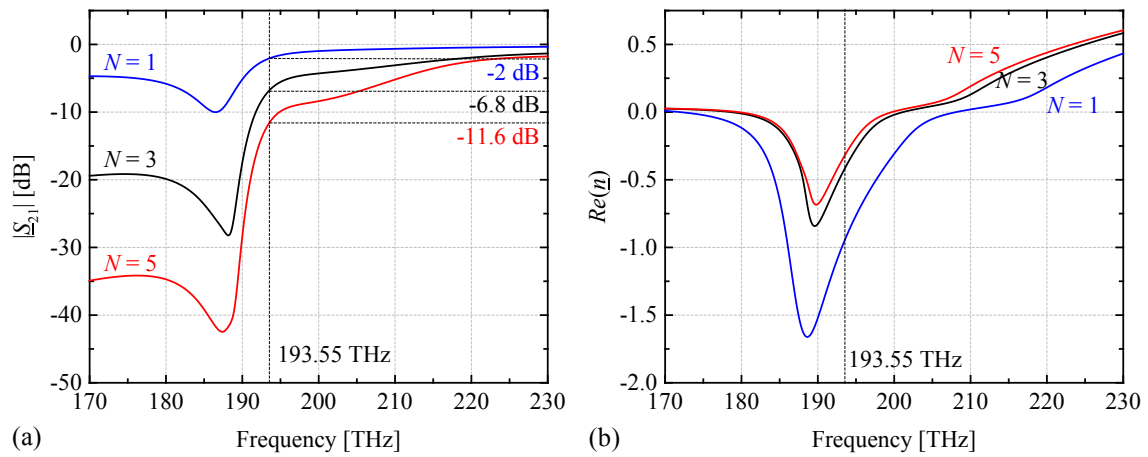


Figure 4.25: (a) Simulated transmission spectra and (b) retrieved real part of the refractive index using $\Lambda = 640$ nm, $R_m = 224$ nm, and $w_m = 30$ nm for different numbers of layers.

Since the single layer shows a negative refractive index with far fewer losses than the multilayer, it is meaningful to design the plano-concave lens using $N = 1$ in the middle while slightly increasing the thickness at the edges. Using a plane wave launch of a width around $12 \mu\text{m}$, the plano-concave configuration with a spherical curvature radius $R_a = 15 \mu\text{m}$ shows good focusing ability and a tight focus with $\text{BW} = 3.2 \mu\text{m}$ at an FFL of $13.5 \mu\text{m}$ as depicted in Figure 4.26. However, due to the large refractive index difference between the layer sections with $N = 1$ and $N > 1$, the focal length tends toward higher values than in the case of a plano-concave NIM lens having a homogeneous effective refractive index of -1 .

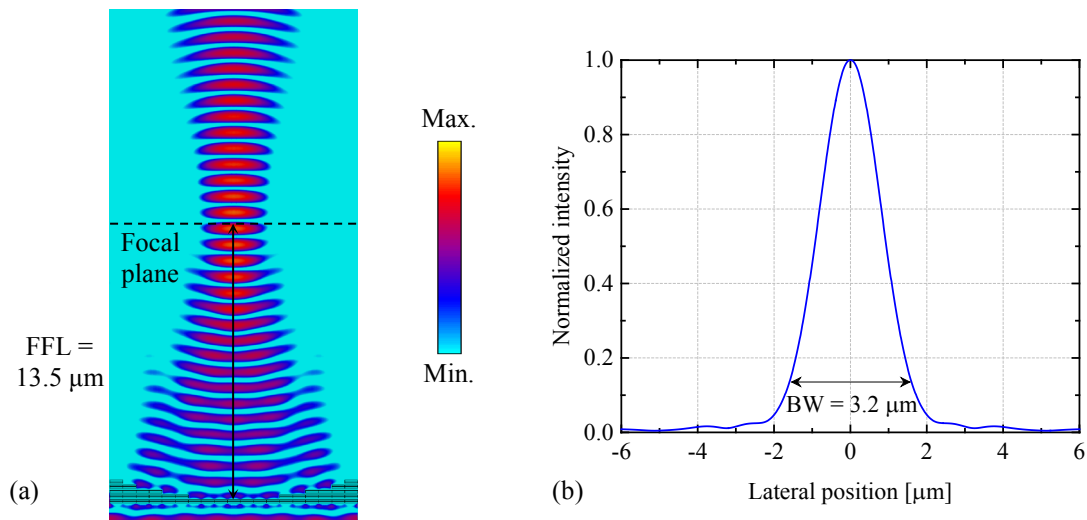


Figure 4.26: (a) Electric field distribution of the NIM lens and (b) the corresponding normalized intensity profile at the focal plane at 193.55 THz.

Indeed, the presented plano-concave NIM lens exhibits an acceptable transmission efficiency of nearly -2 dB with a double-negative behavior in a large bandwidth of 13.5 THz, which corresponds to a wavelength range exceeding 100 nm, though the structure has some critical dimensions that may not be easily fabricated. In fact, the metal wires designed have a width of only 30 nm and can be challenging to the technological process. Increasing this width to a value of e.g. 100 nm, which can be realized by means of electron beam lithography, reduces the transmission of the single layer to -2.8 dB at a much larger period of $\Lambda = 750$ nm.

4.7. Conclusion

The exciting field of metamaterials allows the flexible control of the electromagnetic response with properties that cannot be seen in nature such as the effect of negative refraction. This phenomenon can be used to realize compact lensing systems with more advantages than their dielectric counterparts. In fact, the investigations on fishnet plano-concave NIMs in the radio frequency range reveal a considerable reduction of the focal length with even better transmission properties than standard plano-convex lenses.

The realization of highly efficient 3D NIMs necessitates the reduction of reflection and absorption losses. This is done first by choosing the appropriate materials and the optimization of the unit cell parameters in order to achieve perfect impedance matching to

the surrounding environment and low attenuation inside the metamaterial. Furthermore, enhancing the coupling between the functional layers guarantees high transmissivity with a strong magnetic resonance. However, decreasing the metamaterial losses gives rise to possible propagating higher-order modes, which may violate the homogeneity principle, and a trade-off between both behaviors has to be made.

The fabricated metamaterial stack exhibits a high transmissivity of -0.5 dB with a negative refractive index of -1 at the operating frequency 38.5 GHz. In addition, the plano-concave configuration has good focusing ability with a reduction of the launched beam width by a factor of 2.2 at an FFL of $6 \lambda_0$. A comparison between the simulated and measured results of the designed NIM lens versus the aspheric dielectric lens is illustrated in Figure 4.27.

Indeed, scaling the dimensions of the NIM lens to THz frequencies enables compact and tight focusing, which is advantageous for nanocoupling between optical fibers and integrated waveguides. However, the considerable metal losses decrease the total efficiency significantly and limit the applicability of metamaterials in real applications. Hence, alternative solutions, for example based on gain media [104] or low loss conducting oxides [105], have to be used in order to compensate for these absorption losses at optical frequencies.

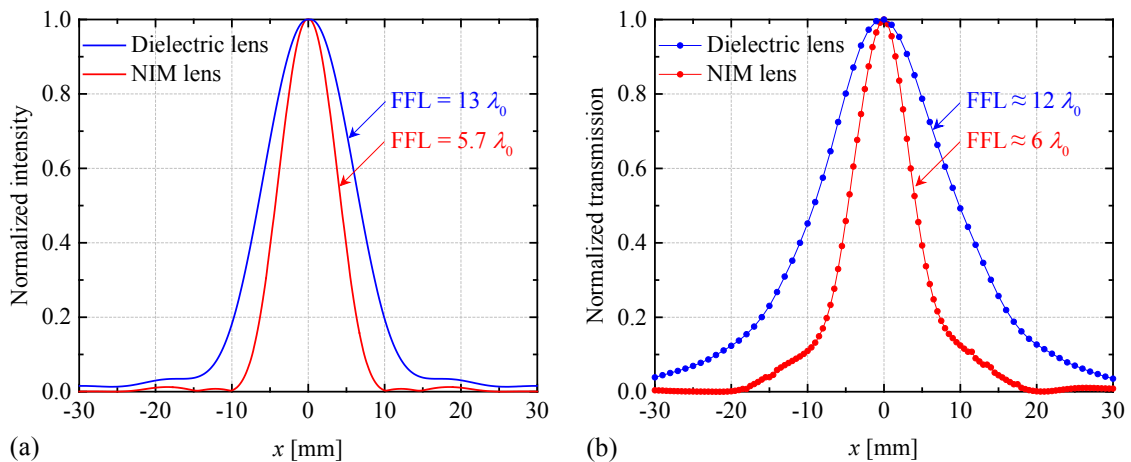


Figure 4.27: Normalized (a) simulated intensity and (b) measured transmission profiles of the designed NIM plano-concave lens versus a dielectric plano-convex lens at the corresponding focal plane.

5. Bragg diffraction gratings

In this chapter, the second coupling method based on Bragg diffraction gratings is discussed. First, the operating principle of grating couplers and a theoretical estimation of the achievable coupling efficiency are introduced. Afterwards, the adopted designs are numerically investigated, and a rigorous optimization procedure is described. Finally, measurement results of the fabricated uniform and nonuniform gratings are shown.

5.1. Theory of grating couplers

The phenomenon of diffraction based on single- and multi-slit apertures is elaborated in section 3.2.3. It is shown that a plane wave impinging on periodically arranged slits is diffracted at these individual scatterers and leads to an angle-dependent interference pattern. When the scattered components interfere constructively, i.e. add up in phase, intensity maxima take place at the corresponding angles, defining the diffraction orders. The relationship between the wavelength, the period, the incident angle, and these diffraction orders is described by Bragg's law.

Another way to illustrate the behavior of Bragg diffraction gratings is based on the k -space analysis as shown in the example of Figure 5.1. Here the 1D grating of a period Λ along the z -direction is assumed to be at the interface between two media of refractive indices $n_c < n_s$. An incident wave vector \vec{k}_i from medium 1 is scattered at the grating and produces a set of diffracted waves. Due to the conservation of momentum law, the sum of the horizontal component of the incident wave $k_{i,z}$ and the m -fold of the grating reciprocal lattice $K = 2\pi/\Lambda$ has to equal the diffracted wave component $k_{m,z}$ according to [106], [107]

$$k_{i,z} + mK = k_{m,z}, \quad (5.1)$$

where m is an integer. Using $k_{i,z} = k_i \sin \alpha_i$ and $k_{m,z} = k_m \sin \alpha_m$, with α_i and α_m are the incident and diffraction angles respectively, it can be seen that the latter equation is identical to (3.46). When no grating is existent, (5.1) turns into Snell's law.

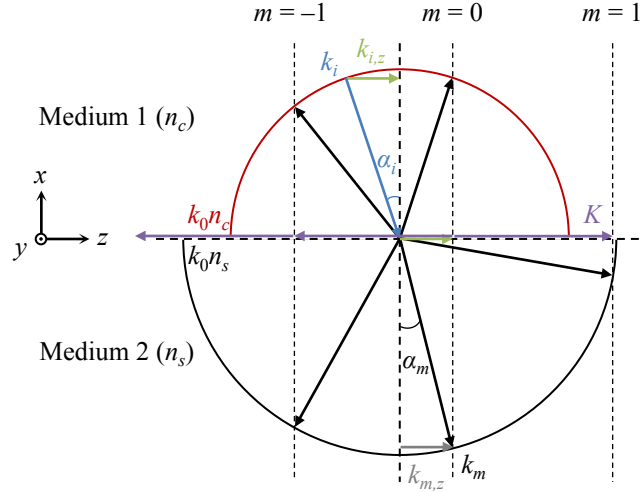


Figure 5.1: k -space diagram of a diffracted wave at a grating separating two media with $n_c < n_s$ and the corresponding possible solutions [106].

Similarly, a surface grating coupler is composed of a corrugated layer, which diffracts the input beam of a vertical fiber to the horizontal waveguide. The simplest configuration of such a structure is realized by etching periodically arranged 1D rectangular grooves of a certain depth into the waveguide film layer. Taking into account the propagation constant in the waveguide $\beta_m = k_0 n_{eff}$, the grating period can be adjusted to match the incident wave exactly to the waveguide mode. In this case, the master equation for surface grating couplers is given as

$$k_i \sin \alpha_i + m \frac{2\pi}{\Lambda} = \beta_m. \quad (5.2)$$

The difference between this coupling method and other lateral coupling techniques, such as described in the previous chapter, is that light has to change its direction from the vertically mounted fiber to horizontally lying waveguides. Indeed, out-of-plane coupling carries several advantages owing to the possibility of wafer-scale testing without the need for post-processing steps such as cleaving and edge polishing; however, it also necessitates a more complex design that enables matching the mode of the fiber to the waveguide.

Figure 5.2 illustrates the cross section of a simple grating coupler in the SOI platform and the corresponding wave vector diagrams for an incident angle $\alpha_i = 0$ and $\alpha_i > 0$ re-

spectively. Assuming that the Si film layer is sandwiched between two SiO₂ layers, both semicircles in the diagrams have the same radius. In the case of a vertically incident wave, it is clear that there is more than one solution to the Bragg equation. In addition to the 0th diffraction order, the input power is symmetrically coupled to the right and left parts of the waveguide, which correspond to $m = 1$ and $m = -1$ respectively. Indeed, both portions can subsequently be added up using a power combiner, but with additional footprint and optical losses. In the case of a tilt angle $\alpha_i \neq 0$, it is possible to fulfill the former phase-matching condition for only the 1st diffraction order so that most of the input light is directed to the integrated waveguide on the right hand side without additional design effort. For a given n_{eff} , the latter structure requires a lower K value to satisfy the phase matching condition, and hence a larger period. For both configurations, the 0th diffraction order is always present and constitutes the main loss source for this coupling method. In fact, one part is reflected upwards to the cladding layer, whereas the other part is transmitted downwards to the substrate. Thus, in order to increase the coupling efficiency from the fiber to the waveguide, these components have to be eliminated or recycled.

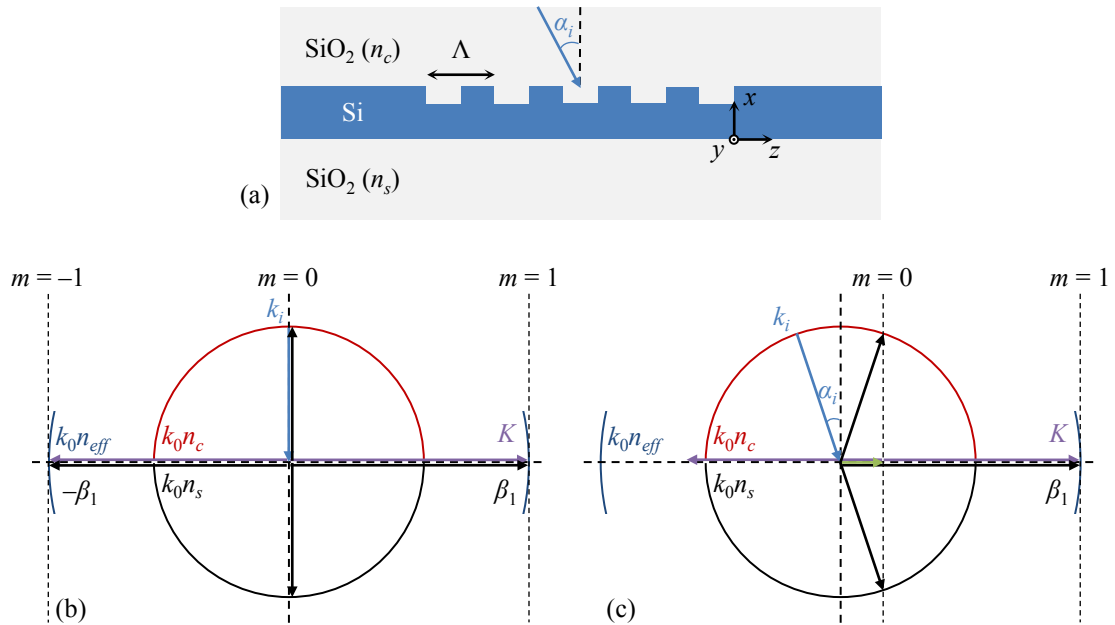


Figure 5.2: (a) Cross section of a 1D grating in the SOI platform with $n_c = n_s$ and the corresponding k -space diagram for (b) $\alpha_i = 0$ and (c) $\alpha_i \neq 0$.

The required grating period Λ to couple light at a certain wavelength can be determined from the master equation and is expressed as

$$\Lambda = \frac{\lambda_0}{n_{eff} - n_c \sin \alpha_i}. \quad (5.3)$$

In the simplest case where the fiber is vertically placed on the structure, the period is

$$\Lambda = \frac{\lambda_0}{n_{eff}}. \quad (5.4)$$

According to the coupled mode theory, n_{eff} can be approximated by the average of the fundamental mode effective indices in the unetched and etched waveguide regions $n_{eff,0}$ and $n_{eff,1}$ respectively since the wave in the grating film layer propagates in the fundamental mode [107]. Assuming that both regions have the same length, it follows

$$n_{eff} = \frac{n_{eff,0} + n_{eff,1}}{2}. \quad (5.5)$$

Using a symmetric Si film layer of thicknesses 250 nm and 180 nm, which correspond to an etch depth of 70 nm, the effective indices of the fundamental mode for TE polarization at $\lambda_0 = 1550$ nm, i.e. with the electric field along the y -direction, can be determined from equations (3.51) and (3.52) in the third chapter. For sufficiently thick SiO_2 cladding and substrate layers, the effective indices are $n_{eff,0} = 2.93$ and $n_{eff,1} = 2.69$. Hence, the period is nearly 550 nm for $\alpha_i = 0^\circ$, whereas it amounts to 600 nm for an off-vertical angle $\alpha_i = 9^\circ$. As tilting the fiber prevents coupling to diffraction orders other than $m = 1$, regardless of the omnipresent 0th order, it is reasonable to investigate off-vertical angles $\alpha_i > 0$.

It should also be noted that since the effective refractive index of TE is larger than that of TM, the corresponding period has to be smaller, and hence a grating of a given period cannot couple both polarizations efficiently. Therefore, these structures are generally polarization-dependent. In order to tackle this problem, there are some methods that can be used e.g. by coupling the TM state into the -1^{st} diffraction order in 1D gratings [36] or also by designing 2D configurations that split the beam into two TE polarized parts without the need for an additional polarization rotator [50]. In the following sections, only coupling based on the TE polarization is considered.

5.2. Diffraction gratings as nanocouplers

Using Bragg's law it is possible to determine the exact period value to couple light at a certain wavelength and angle. In addition, the k -space diagram offers an insight into the possible loss sources such as upward reflection and downward transmission to the substrate. Nevertheless, no information on the amount of these loss factors or on the achievable coupling efficiency is given. Hence, it is necessary to analyze the coupling procedure starting from the fiber to the waveguide so as to accurately determine the total efficiency.

Figure 5.3 illustrates an optical fiber core placed in free space over a linear grating in the SOI platform. The grating is composed of a finite number of grooves periodically etched in the Si film layer, which is sandwiched between two sufficiently thick SiO₂ layers. Since the grating must have dimensions in the order of the core diameter to couple most of the light, the width has to be tapered down to match the dimensions of the nanowaveguide. Similarly to the last chapter, the overall coupling efficiency from the fiber to the waveguide, defined as the ratio of the output to the input optical power $\eta = P_{out}/P_{in}$, is given by

$$\eta = T_C \cdot \eta_O \cdot \eta_D \cdot \eta_T. \quad (5.6)$$

T_C is the transmission from free space to the cladding, dictated by the difference of the SiO₂ refractive index $n_c = 1.444$ to the free space index $n_{air} = 1$, which is given for the TE polarization by the Fresnel equation

$$T_C = 1 - \left(\frac{n_{air} \cos \alpha_i - \sqrt{n_c^2 - n_{air}^2 \sin^2 \alpha_i}}{n_{air} \cos \alpha_i + \sqrt{n_c^2 - n_{air}^2 \sin^2 \alpha_i}} \right)^2. \quad (5.7)$$

η_O is the overlap integral between the electric field profile of the fiber mode E_f and the electric field profile of the grating E_g along the longitudinal and lateral directions

$$\eta_O = \eta_{O,z} \cdot \eta_{O,y} = \frac{\left| \int_A E_f E_g^* dA \right|^2}{\int_A |E_f|^2 dA \int_A |E_g|^2 dA}. \quad (5.8)$$

η_D is defined as the directionality [106] and describes the ratio of the diffracted optical power from the fiber into the waveguide P_w to the total scattered power P_s

$$\eta_D = \frac{P_w}{P_s} = \frac{P_w}{P_{up} + P_{down} + P_w}. \quad (5.9)$$

P_{up} and P_{down} are the upward- and downward-diffracted optical powers respectively. Again, η_T represents the mode conversion efficiency of the taper and can be approximated to 1 for sufficiently long structures.

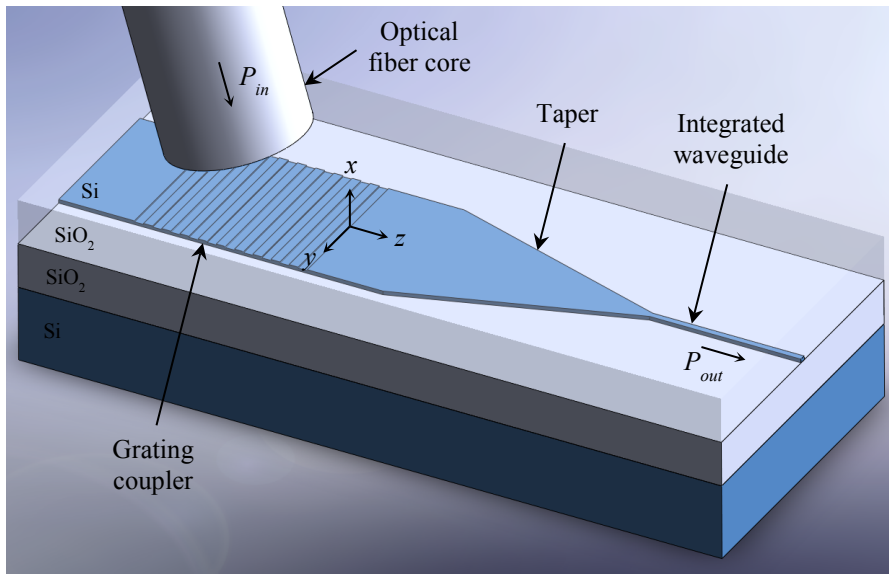


Figure 5.3: Coupling configuration from the optical fiber core to the waveguide using an integrated surface diffraction grating and an adiabatic taper.

In order to achieve a high total efficiency, the latter terms have to be optimized separately. First, the Fresnel reflections can be eliminated by introducing a matching index material between the fiber and the SiO_2 cladding layer using, for example, matching index liquids (MILs) of a refractive index $n_{\text{MIL}} \approx 1.45$. In this case,

$$T_C = 1 - \left(\frac{n_{\text{MIL}} \cos \alpha_i - \sqrt{n_c^2 - n_{\text{MIL}}^2 \sin^2 \alpha_i}}{n_{\text{MIL}} \cos \alpha_i + \sqrt{n_c^2 - n_{\text{MIL}}^2 \sin^2 \alpha_i}} \right)^2 \approx 1. \quad (5.10)$$

Second, the overlap integral can be maximized by matching the Gaussian beam form of the SMF to the grating field profile. For this purpose, the integral is separated into two

terms for lateral and longitudinal matching. While the former factor is optimized by calculating the required grating width, the optimization step of the latter parameter is not trivial. In fact, the power in a periodic grating does not have a Gaussian-like shape in the longitudinal direction but an exponentially decaying form expressed as [106]

$$P(z) = P_0 e^{\kappa_{GC} z} \text{ for } z \leq 0, \quad (5.11)$$

where κ_{GC} denotes the coupling strength of the grating. The position $z = 0$ corresponds to the grating edge, which faces the waveguide where the optical power is to be coupled out. The latter equation means that light in the middle of the grating is less coupled than in the proximity of the waveguide and is predominantly reflected upwards. Hence, to have a high overlap along the z -direction, the coupling strength has to be designed so that the grating profile exhibits a Gaussian-like form. This is possible by adapting the length of each groove and rib, and therefore the grating is called aperiodic or apodized. Finally, in order to enhance the directionality, the diffracted optical power to the Si substrate has to be redirected back to the waveguide using e.g. a high-reflective mirror at an adequate distance from the film layer. Certainly, the lower Si/SiO₂ interface represents a mirror with a reflectivity of 17%, but it is more meaningful to use for example a metal layer to recycle all downward optical power. The distance between the mirror and the film is of major importance since destructive interference may take place and minimize the coupling efficiency if the value is not adequately calculated.

As previously mentioned, the grating width has to be in the order of the fiber core diameter to couple most of the input power into the film layer. Thus, reducing the width from e.g. 10 μm to 400 nm requires a taper with a length of at least 100 μm to achieve a high mode conversion efficiency $\eta_T > 95\%$ as demonstrated in the third chapter. That means that the advantage of grating compactness is deteriorated by the large taper dimensions. The grating coupler can also be designed as a focusing structure so that the taper length is dramatically reduced [39]. This is realized by shaping the lines of the grooves and ribs to elliptical curves according to

$$\frac{(z - z_0)^2}{R_z^2} + \frac{(y - y_0)^2}{R_y^2} = 1, \quad (5.12)$$

$$\text{with } z_0 = \frac{q\lambda_0 n_c \sin \alpha_i}{n_{\text{eff}}^2 - n_c^2 \sin^2 \alpha_i}, y_0 = 0, \quad (5.13)$$

$$R_z = \frac{q\lambda_0 n_{\text{eff}}}{n_{\text{eff}}^2 - n_c^2 \sin^2 \alpha_i}, \text{ and } R_y = \frac{q\lambda_0}{\sqrt{n_{\text{eff}}^2 - n_c^2 \sin^2 \alpha_i}}. \quad (5.14)$$

q is a positive integer and corresponds to the line number. It is clear that one of the two focal points of these ellipses with the coordinates (z_f, y_f) coincides with the origin as

$$\forall q, z_f = z_0 - \sqrt{R_z^2 - R_y^2} = 0 \text{ and } y_f = y_0 = 0. \quad (5.15)$$

Thus, all grating lines are confocal, and light diffracted to the film layer can be focused into a small spot size. In this case, the length of the taper connecting the grating and the nanowaveguide can be reduced to only a few micrometers [39].

5.3. Design of periodic gratings

At first view, the design of grating couplers may be tedious due to the large number of variables to be calculated; however, the simulation can be simplified by fixing some parameters without loss penalty. First, to reduce the computing effort, the 3D problem is reduced to a 2D domain as only structures with uniaxial periodicity are investigated. The extension into the third dimension can be done afterwards by using an adequate width in the case of a linear grating or by shaping the lines of the grooves and ribs to elliptical curves when a focusing configuration is needed. Second, the Si guiding layer thickness is fixed based on commercially available SOI wafers, whereas the shallow etch depth of the grooves is chosen based on standard values used in photonic technological processes [108], [109]. These two parameters are 250 nm and 70 nm respectively, and hence the obtained effective refractive index at a certain polarization and wavelength is fully defined. According to (5.3), the required period can then be determined for the off-vertical tilt angle α_i . Third, the fill factor (FF), defined as

$$\text{FF} = \frac{b}{b+g} = \frac{b}{\Lambda}, \quad (5.16)$$

with b and g the rib and groove lengths respectively, is assumed for instance to be 0.5. Finally, the length of the simulation domain is delimited by fixing the number of periods. This is done by calculating the minimum longitudinal size of the grating, which is required to couple most of the input power to the film layer. The determined length is $15\ \mu\text{m}$ and corresponds to $N = 25$ periods for $\Lambda = 600\ \text{nm}$ [110].

A cross-sectional illustration of the structure to be simulated and the used parameters are depicted in Figure 5.4(a). Furthermore, the tilt angle is fixed to 9° and the launch field MFD to $10.4\ \mu\text{m}$. The top cladding layer is assumed to be $1\ \mu\text{m}$ thick, whereas the buried oxide (BOX) thickness d_{BOX} has to be calculated in order to guarantee constructive interference between the reflected field at the lower Si/SiO₂ interface and the diffracted field toward the waveguide. The 2D simulation in the xz -plane is done using RSoft FullWAVE. As the overlap between the fiber mode and the grating field profile depends on the position of the input beam, this parameter is swept in a first step along the z -direction. Afterwards, the launch field is fixed at the optimal value, and the total coupling efficiency is simulated over the BOX thickness as shown in Figure 5.4(b).

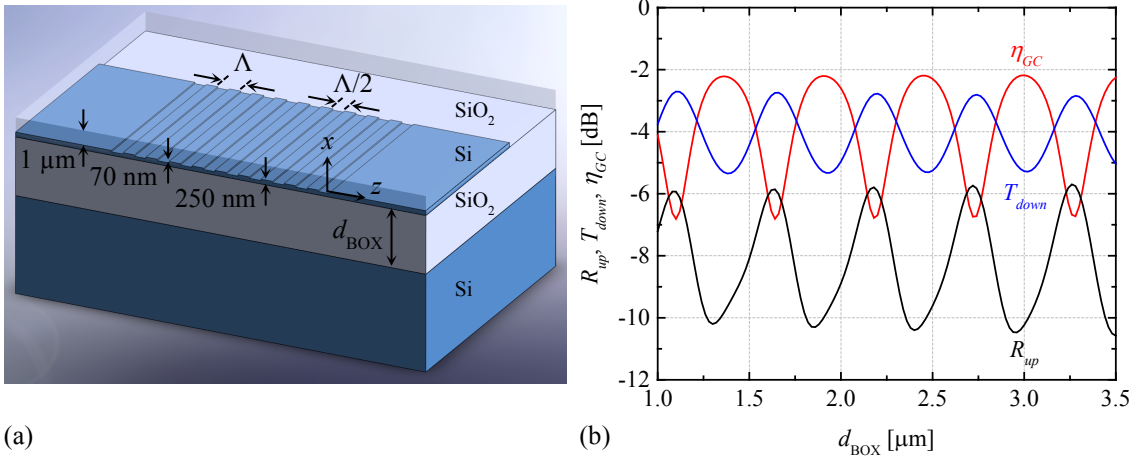


Figure 5.4: (a) 3D cross section of the investigated grating structure. (b) Simulated upward reflection R_{up} , downward transmission T_{down} , and coupling efficiency η_{GC} versus the BOX thickness using $\Lambda = 600\ \text{nm}$ and $\alpha_i = 9^\circ$ at $1550\ \text{nm}$ for TE polarization. The used refractive indices of Si and SiO₂ are 3.476 and 1.444 respectively.

The Fresnel reflections and the mode conversion loss of the taper are not included in the simulation since they can be optimized separately. Hence, the coupling efficiency of the analyzed structure can mainly be described by the modal overlap along the z -direction and the directionality, i.e. $\eta_{GC} = \eta_{O,z} \cdot \eta_D$. That means that the main loss factors here are the upward reflection R_{up} and the transmission toward the substrate T_{down} . If the phase matching condition is not fulfilled for only the 0th and 1st diffraction orders, the transmission toward the left part of the waveguide has also to be considered.

It can be seen from Figure 5.4(b) that the coupling efficiency depends strongly on the BOX thickness with maxima at $d_{BOX} \approx (2q + 1) \cdot \lambda/4$ and minima at $d_{BOX} \approx 2q \cdot \lambda/4$, where q is a positive integer and λ is the wavelength in the SiO₂ layer. The highest achievable coupling efficiency attains only -2.17 dB due to the low directionality of this configuration with ± 0.13 μm variation tolerance for 1 dB loss penalty. As commercially available SOI wafers have predefined BOX thicknesses, a value of 3 μm is selected since it is located in the vicinity of a transmission peak. If other standard wafers with a thickness for example of 2 μm are chosen, the theoretical efficiency cannot exceed -2.6 dB. Hence, this parameter is of main importance when optimizing grating couplers.

Using $d_{BOX} = 3$ μm , the spectra of the coupling efficiency and the major loss factors are simulated. Figure 5.5 illustrates the electric field distribution at 1550 nm and the obtained wavelength-dependent behavior. When analyzing grating couplers, it is more common to plot the spectral efficiency against the wavelength than the frequency.

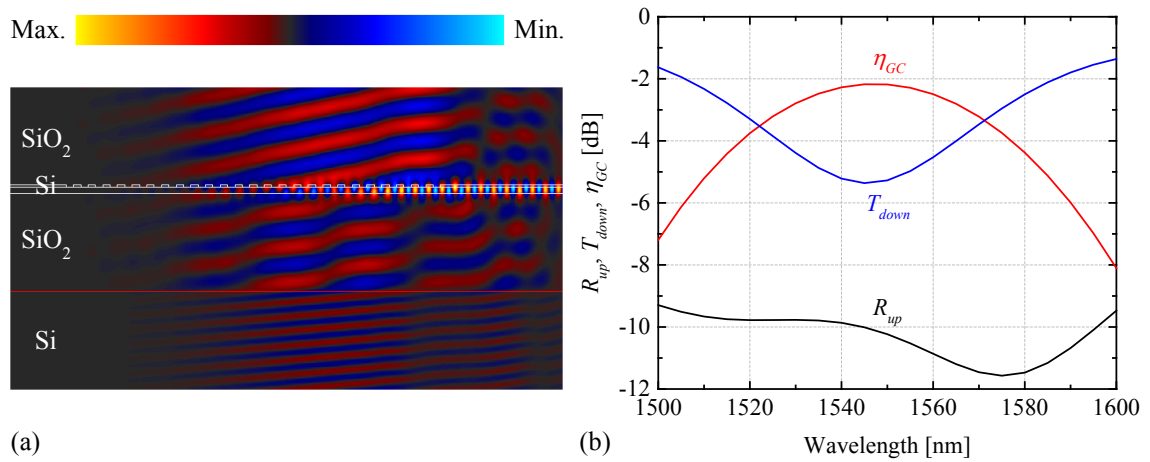


Figure 5.5: (a) Electric field distribution of the grating with $d_{BOX} = 3$ μm at 1550 nm. (b) Simulated spectral efficiency and the main loss factors.

At 1550 nm, the simulated efficiency is -2.18 dB with a large 1 dB bandwidth of more than 44 nm and a 3 dB bandwidth of 75 nm. While the upward-reflected part of power is relatively low and approaches -10 dB, the downward-transmitted part reaches -5 dB at the target wavelength. That means that around one-third of the input power is lost in the substrate, and hence it can contribute considerably to the coupling efficiency when recycled to the output waveguide. The transmitted part to the left side is nearly -50 dB and can be neglected.

5.4. Optimization procedure

In order to realize highly efficient grating couplers, two important factors have to be optimized: directionality and matching the grating field profile to the fiber mode. First, the directionality of periodic gratings is improved, while the second step deals with the optimization of each groove and rib length to adapt the grating field profile to the fiber mode.

5.4.1. Improvement of the directionality

As previously discussed, a considerable fraction of the input power is diffracted to the lower Si substrate of the wafer, and hence the coupling efficiency of a standard grating is usually limited. In order to enhance the directionality, there are two main different possibilities. The first approach relies on using an overlay that enforces constructive interference of the guided light without downward diffraction and makes the grating intrinsically directional [12]. The disadvantage of this technique is that it requires several additional processing steps, and the thickness of the overlay can be optimized for only one orthogonal polarization state. The second approach is based on reflecting back the field transmitted toward the substrate by means of an optical mirror such as a distributed Bragg reflector (DBR) or a metal layer. While the former solution needs multiple sequences composed of thin Si and SiO₂ layers with the exact thickness of a quarter wavelength each [111], the latter method is commonly realized using a gold metal mirror integrated with the help of wafer-to-wafer bonding [112], [113].

The best-known methods to increase the directionality have several drawbacks due to the complex realization or CMOS-incompatibility of the fabrication process. Hence,

there is a necessity to implement a more cost-effective solution with simple technological steps. When an aluminum (Al) layer for example is directly deposited underneath the BOX, the reflectivity can be enhanced and a significant power fraction is able to be directed toward the waveguide. The integration of the mirror can be realized by etching at first a membrane window from the backside through the Si substrate, where the BOX serves as an etch stop, and then by sputtering the metal inside these windows. Thus, the integration can still be achieved in a CMOS-compatible manner without the need for wafer bonding techniques [114].

Figure 5.6(a) illustrates a 3D cross-sectional representation of the proposed grating with an Al layer underneath. The corresponding coupling efficiency and the loss factors at different d_{BOX} values around the target thickness of $3 \mu\text{m}$ are simulated again and shown in Figure 5.6(b). This is important to investigate since the wafer thickness itself varies, and hence identical gratings at different positions on the wafer may behave differently depending on the variation interval. For the chosen SOI wafer, the variation of the BOX thickness amounts to $\pm 0.072 \mu\text{m}$ [115].

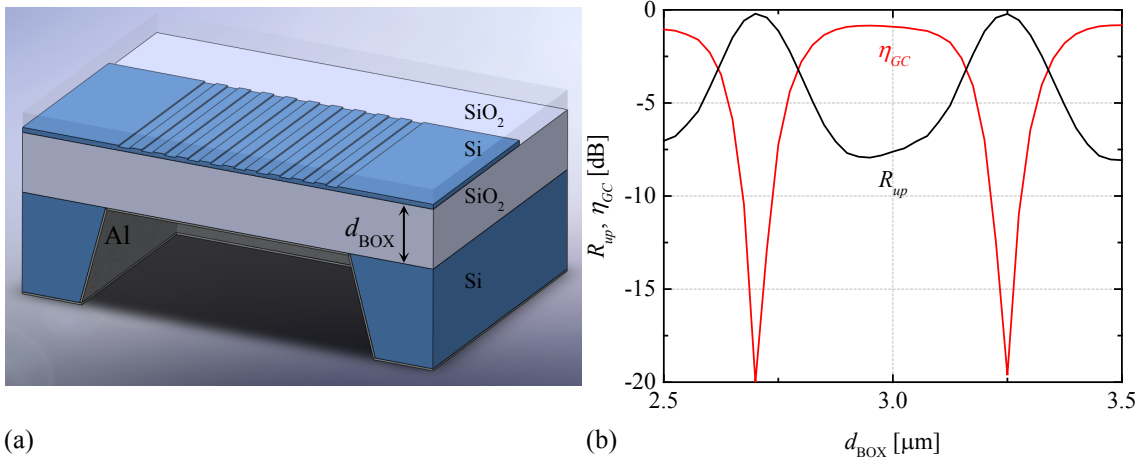


Figure 5.6: (a) 3D cross section of the grating structure with a mirror underneath the BOX. (b) Simulated efficiency and upward reflection versus d_{BOX} using $\Lambda = 600 \text{ nm}$ and $\alpha_i = 9^\circ$ at 1550 nm for TE polarization.

As all downward-diffracted power is reflected at the metal layer, no substrate losses take place and a considerable part is redirected to the film layer and then to the waveguide. The coupling efficiency increases to -0.84 dB at $d_{\text{BOX}} = 2.95 \mu\text{m}$ and reaches

−0.9 dB at the chosen value of 3 μm . Due to the stronger reflection ability than in the first case without a metal mirror, the constructive interference shows a flatter behavior with a higher variation tolerance of $\pm 0.15 \mu\text{m}$ for 1 dB loss penalty below the efficiency at the target thickness. This value is twice the BOX thickness variation on the wafer, and hence it can generate a high yield, which is an important requirement in industrial applications. Nevertheless, the destructive interference exhibits lower dips in the order of −20 dB, and thus an inadequate choice of the BOX thickness may dramatically deteriorate the coupling efficiency. For $d_{\text{BOX}} = 3 \mu\text{m}$, the electric field distribution of the structure at the target wavelength and the spectral behavior between 1500 nm and 1600 nm are depicted in Figure 5.7.

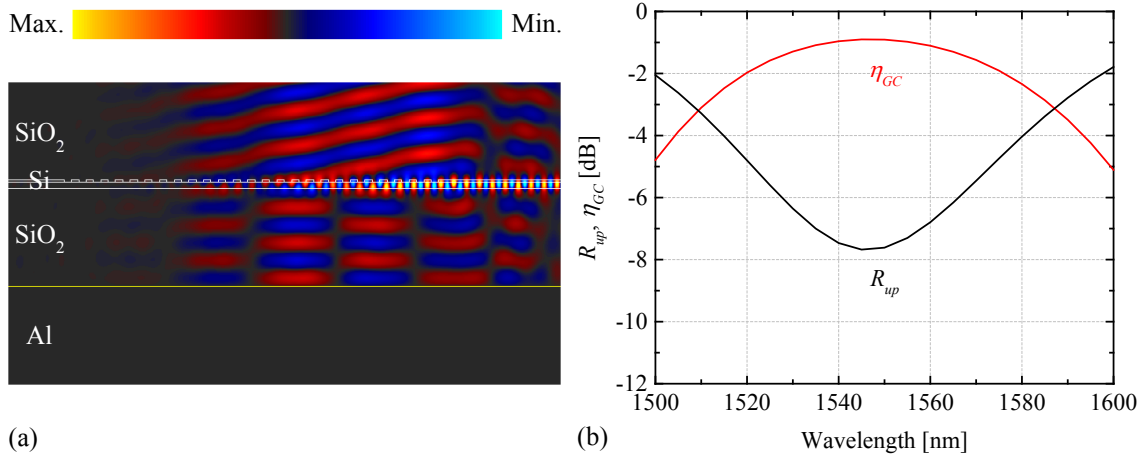


Figure 5.7: (a) Electric field distribution of the grating with $d_{\text{BOX}} = 3 \mu\text{m}$ and a metal mirror underneath at a wavelength of 1550 nm. (b) Simulated spectral efficiency and upward reflection.

As previously shown, the perfect metal mirror clearly improves the directionality, and the coupling efficiency is improved by around 1.3 dB at the wavelength 1550 nm, exceeding the benchmark of −1 dB. Furthermore, the 1 dB bandwidth is enlarged to more than 54 nm and the 3 dB bandwidth to 88 nm. However, since not all recycled optical power is redirected to the waveguide, the upward reflection is increased to −7.6 dB and remains a considerable loss factor if efficiencies of more than 90% are targeted. That means that the total reflected power is composed now of a part, which is produced by the mismatch between the fiber mode and the grating profile, and another part, which is generated from reflection at the metal mirror and not directed to the waveguide. Thus, in

order to reach higher efficiencies, the upward reflection has to be decreased by adjusting the coupling strength along the grating.

5.4.2. Enhancement of the modal overlap

Using a periodic grating without a mirror, around 10% of the input power is reflected back due to the mismatch between the SMF Gaussian mode and the grating field profile. When introducing a metal mirror to enhance the directionality, the upward reflection is increased to more than 17% as previously shown. Hence, the second optimization step relies on improving the longitudinal modal overlap and reducing the total reflection by adjusting the individual elements of the grating. In fact, by decreasing the groove dimensions in the proximity of the waveguide, only a small fraction of light can be diffracted, and hence the strong coupling is apodized. When the subsequent grooves and ribs are designed adequately, most diffraction can be driven to take place around the middle of the grating while diminishing toward the edges so that the field profile can have a Gaussian-like shape.

There exist several approaches to realizing nonuniform gratings. For example, by simultaneously varying the groove depth and length, the coupling strength or leakage distribution can be modified to mimic the fiber mode profile and achieve a high coupling efficiency [116]. However, the fabrication effort is clearly increased since several etching levels are required. A second approach is based on determining the coupling strength analytically while taking account of the minimum manufacturable dimensions [11]. Nevertheless, this method considers only the overlap to the fiber mode and neglects unrecycled power from the reflection at the mirror. It is, therefore, meaningful to implement an algorithm that optimizes each groove and rib length with the purpose of obtaining the highest coupling efficiency by improving the modal overlap and minimizing the total upward reflection.

The simplified flowchart of the adopted algorithm is illustrated in Figure 5.8(a) [110]. The starting point is a periodic grating with a metal mirror underneath and the above mentioned parameters $\Lambda = 600$ nm and $FF = 0.5$. All elements of the 25 periods have to be adjusted to ensure the highest achievable efficiency at the wavelength 1550 nm for TE polarization and 9° off-vertical tilt angle. The algorithm starts with optimizing the

first rib-groove pair in the proximity of the waveguide by sweeping the corresponding FF from 0.01 to 0.99 in steps of 0.02 for a set of periods from 520 nm to 660 nm in 20 nm steps and saving the dimensions for the best-calculated efficiency. The procedure is applied for all subsequent pairs and is defined as a generation. This routine is repeated for the whole grating again and again until the result converges. The number of iterations is defined as the product of the number of generations and rib-groove pairs. The second step of the algorithm serves to refine the obtained dimensions since only a predefined set of periods is used to ensure a short simulation time. Therefore, each element is optimized separately starting from a length variation of ± 10 nm down to ± 1 nm. Here a generation is defined when all elements are investigated within a single optimization cycle. This routine is also repeated for the whole grating until no higher coupling efficiency is obtained. The number of iterations during this step corresponds to the product of the number of generations and elements [117].

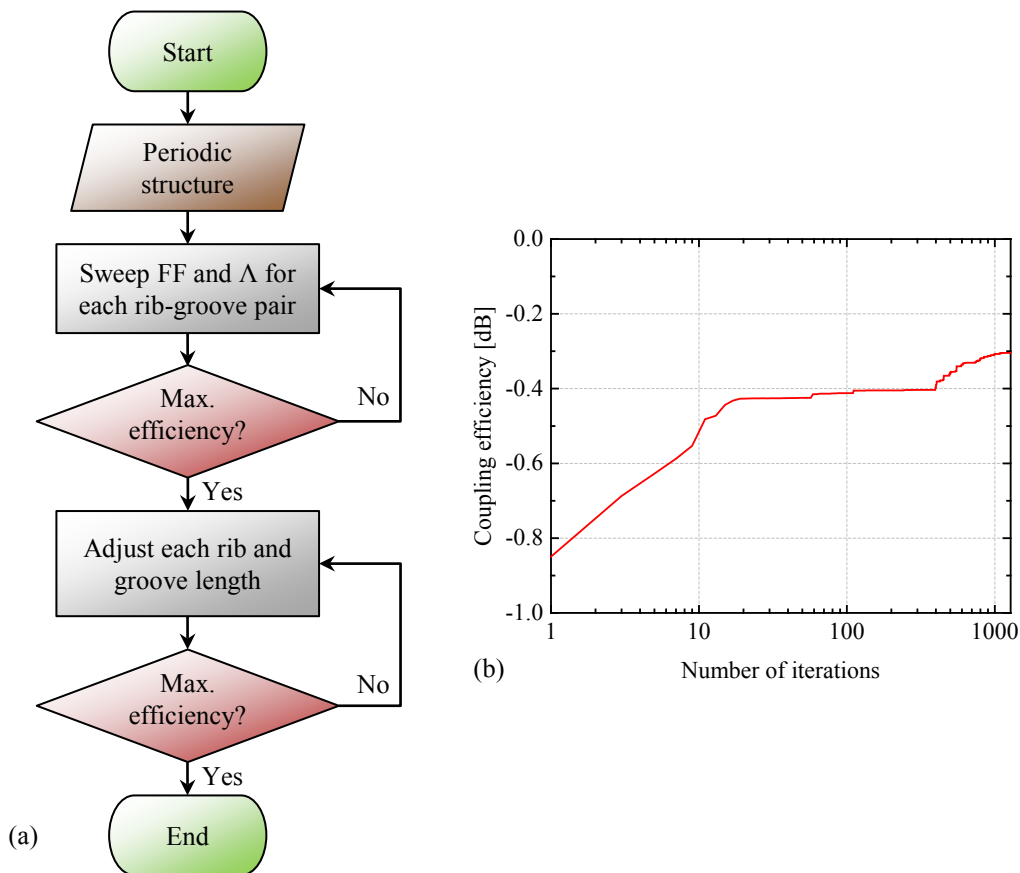


Figure 5.8: (a) Simplified algorithm flowchart for the optimization of the individual grating elements. (b) Typical coupling efficiency progression.

The optimization algorithm is implemented in MATLAB, and the 2D simulations are carried out by the open source software CAMFR based on the eigenmode expansion method. The advantage of this method in comparison to the FDTD tool previously used is that the simulation domain is not discretized into very fine grids but divided in regions of the same refractive index [118]. Hence, the computational effort is lessened and the optimization time is dramatically reduced. However, the final structure is simulated based on RSoft FullWAVE since it delivers a more accurate result.

It should also be noted that the field excitation in CAMFR occurs in the waveguide and not the fiber. Thus, the coupling efficiency is determined from the opposite direction as the ratio of the output power in the fiber to the waveguide input power. Owing to the reciprocity of the configuration, both directions have to deliver the same results [106].

Figure 5.8(b) represents the typical efficiency progression of the optimized structure as a function of the total iteration steps. The first iterations are responsible for the fast enhancement since it suffices to adapt the FF of the grating region in the proximity of the waveguide to decrease the coupling strength and approach the targeted Gaussian profile. While this step improves the efficiency by ~ 0.4 dB, the following refinement step yields ~ 0.1 dB enhancement.

In order to emphasize the origin of the coupling efficiency improvement, the diffracted field profiles of the starting periodic structure and the finally obtained aperiodic grating are compared to each other. Both profiles and the fiber Gaussian function are depicted in Figure 5.9. It is clear that the similarity of the scattered field at the aperiodic grating is much better than for the case of a periodic structure. Hence, the modal overlap between both profiles is larger, and the coupling efficiency is improved to more than -0.4 dB.

The dimensions of the optimized nonuniform structure, called GC₁, are shown in Table 5.1 where the lengths of the individual grooves and ribs are labeled g_i and b_i respectively. In order to obtain a more accurate result, the grating coupler is simulated using RSoft FullWAVE. Figure 5.10 depicts the corresponding electric field distribution at the target wavelength and the spectral efficiency between 1500 nm and 1600 nm.

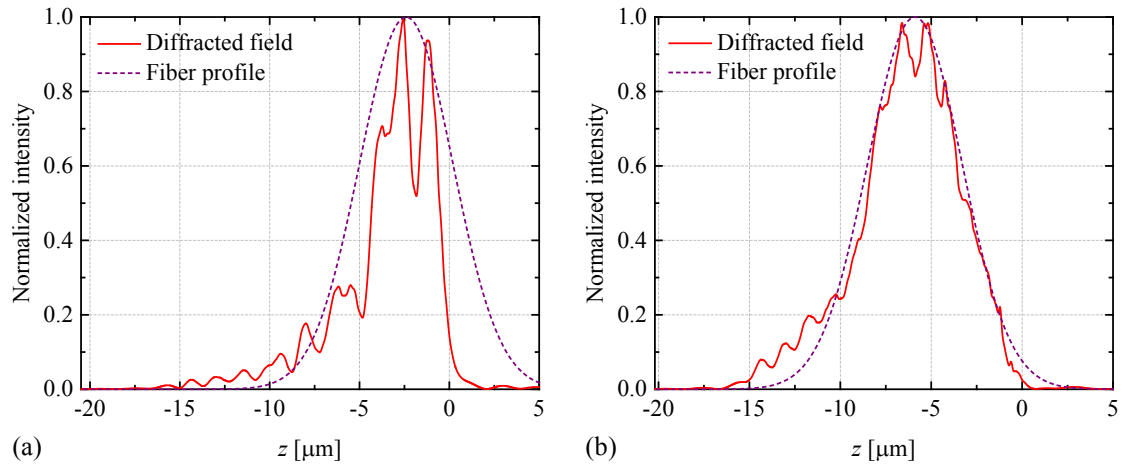


Figure 5.9: Fiber and diffracted field profiles of (a) the initial periodic structure and (b) the obtained aperiodic grating after the optimization procedure.

Table 5.1: Dimensions of the optimized nonuniform grating GC_1 in nm. g_1 corresponds to the length of the nearest groove to the output waveguide.

g_1	b_1	g_2	b_2	g_3	b_3	g_4	b_4	g_5	b_5	g_6	b_6	g_7	b_7	g_8	b_8	g_9
42	515	81	550	67	471	434	87	516	133	478	149	218	427	156	409	269
b_9	g_{10}	b_{10}	g_{11}	b_{11}	g_{12}	b_{12}	g_{13}	b_{13}	g_{14}	b_{14}	g_{15}	b_{15}	g_{16}	b_{16}	g_{17}	b_{17}
338	268	318	303	313	277	308	288	312	289	313	291	312	276	319	291	315
g_{18}	b_{18}	g_{19}	b_{19}	g_{20}	b_{20}	g_{21}	b_{21}	g_{22}	b_{22}	g_{23}	b_{23}	g_{24}	b_{24}	g_{25}	b_{25}	g_{26}
282	316	296	296	299	320	282	304	274	331	274	303	298	324	289	283	302

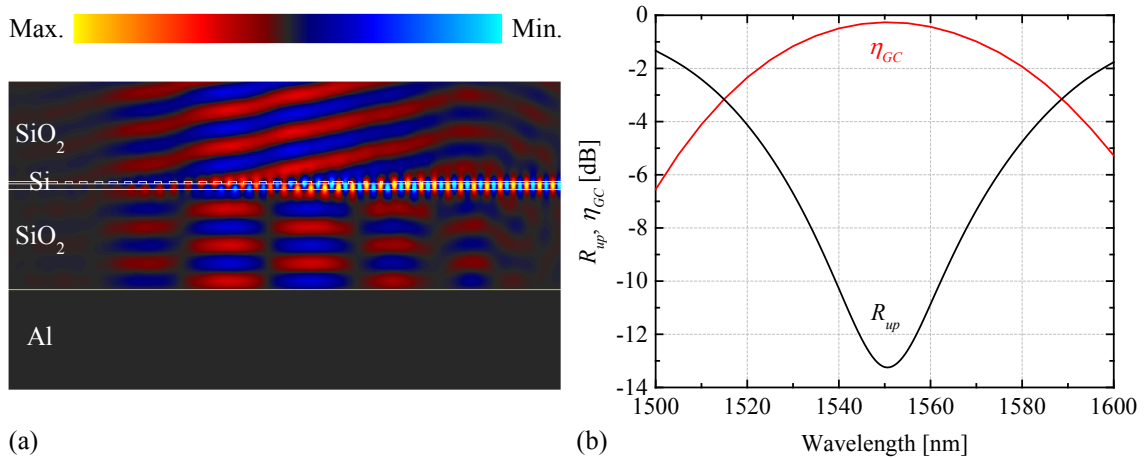


Figure 5.10: (a) Electric field distribution of the obtained nonuniform grating at 1550 nm. (b) Simulated spectral efficiency and upward reflection.

The electric field distribution shows that the power is less coupled at the waveguide edge due to the large FF, which corresponds to a narrow groove length, and the maximum coupling is shifted toward the middle of the grating. The improved modal overlap produces a very high coupling efficiency, which reaches -0.26 dB at 1550 nm, a 1 dB bandwidth larger than 43 nm, and a 3 dB bandwidth of 75 nm. In addition, the upward reflection is reduced to less than -13 dB. Thus, using a metal mirror and apodizing the grating based on the adapted algorithm significantly enhances the coupling efficiency while still retaining a large bandwidth.

The dimensions of the grating in Table 5.1 show that shaping the grating field profile to a Gaussian-like function necessitates very narrow grooves in the proximity of the output waveguide with lengths smaller than 100 nm in addition to some ribs with similar critical dimensions. g_1 and b_4 , with values of 42 nm and 87 nm respectively, may be especially technologically challenging. As these structures are aimed to be concretely fabricated, it is meaningful to carry out the optimization with more relaxed dimensions and compare the results with the ideal case. For this purpose, the algorithm is run again with different prerequisites. The second grating, called GC₂, has to exhibit a minimum rib and groove length of 100 nm and 60 nm respectively to be able to be realized by means of electron beam lithography. The third structure, meanwhile, called GC₃, has to be limited to nearly 120 nm for both parameters so that it can be fabricated using deep UV lithography for example.

The obtained structures are verified using RSoft FullWAVE, and the corresponding spectral efficiencies are shown in Figure 5.11. The critical dimensions of GC₂ are relaxed to $g_{min} = 60$ nm and $b_{min} = 115$ nm with a coupling efficiency of -0.33 dB at 1550 nm, whereas GC₃ with $g_{min} = 110$ nm and $b_{min} = 115$ nm still exhibits a high efficiency of -0.41 dB. The 1 dB bandwidth of all three structures is around 43 nm. Hence, it can be seen that relaxing the minimal lengths to values in the range of 100 nm does not degrade the performance dramatically, and the theoretically achievable coupling efficiency is still better than -0.5 dB. These dimensions are technologically manageable, and the resulting gratings can be fabricated using the aforementioned procedures. In this thesis, both structures GC₂ and GC₃ are realized based on the electron beam lithography, and the fabrication process is described in chapter 5.5.

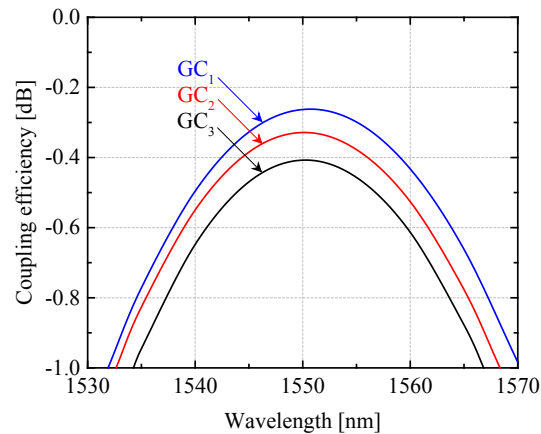


Figure 5.11: Simulated spectral efficiency of the three designed gratings with variable critical dimensions.

Finally, after optimizing the grating profile in the z -direction, the modal overlap has also to be maximized along the lateral direction. In fact, η_O is composed of two terms with $\eta_O = \eta_{O,z} \cdot \eta_{O,y}$, where $\eta_{O,y}$ is assumed to be 1 in 2D simulations. Thus, in order to obtain a high total efficiency using concrete 3D structures, the optimal grating width w_{GC} has to be determined. This is done by simulating the fundamental waveguide mode profile for different widths and calculating the lateral overlap with the fiber mode. The result is illustrated in Figure 5.12 and shows that the grating width has to range between 11 μm and 16 μm in order to reach an overlap higher than 90%. Values outside this interval yield a modal mismatch and decrease the total coupling efficiency [117].

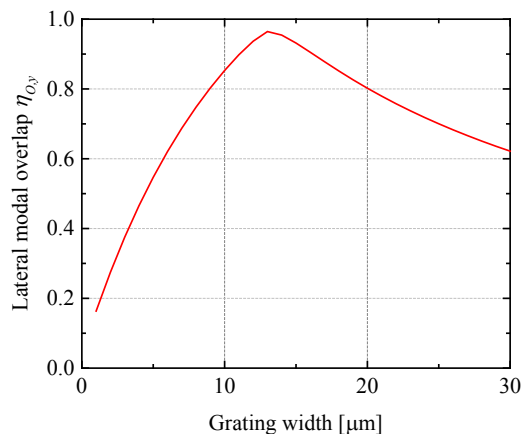


Figure 5.12: Calculated modal overlap along the lateral direction versus the grating width.

5.5. Fabrication process

The designed grating couplers are fabricated at IMS CHIPS using an SOI wafer flow process based on standard technological procedures [119]. The fabrication steps are schematically detailed in Figure 5.13, starting from the SOI wafer with a 3 μm thick BOX and a 250 nm top Si layer, up to the obtained grating with the Al mirror [120].

First, the wafer is coated with a positive tone photoresist, and the part of the grating to be recessed later is exposed by means of an electron beam writer. Thereafter, the pattern transfer into the top Si layer is done by time-controlled dry etching to a depth of 70 nm, defining the grating grooves as shown in Figure 5.13(c), and the remaining resist is removed. Then, the wafer is coated again with a positive tone photoresist, and the part that defines the waveguide structure is exposed. Using a dry etching process, a 250 nm etch step down to the BOX is performed, and the photoresist is stripped afterwards. Subsequently, a 1 μm thick SiO_2 passivation layer is deposited on the top of the wafer and serves as cladding for the film layer. Figure 5.13(f) illustrates the obtained structure, which represents a standard grating with a relatively low coupling efficiency as previously discussed.

In order to enhance the directionality, metal mirrors are to be added underneath the BOX below the gratings. For this purpose, an oxide hard mask is deposited and a positive tone photoresist is coated on the wafer backside. After defining the membrane windows by means of optical lithography, the hard mask is dry etched and the remaining resist is removed. These membrane windows are then wet etched through the 625 μm thick Si substrate down to the BOX. The mirror cavities just underneath the gratings have an area of 50 $\mu\text{m} \times 50 \mu\text{m}$ and can also be realized similarly using a dry etching process. When designing different gratings on the wafer, a sufficiently large distance between the individual mirrors have to be guaranteed in order to prevent the interconnection of the cavities and ensure the stability of the wafer. Finally, an Al layer is sputter-deposited in the membrane cavities as shown in Figure 5.13(k). Hence, the adopted fabrication procedure is CMOS-compatible, cost-effective, and is considerably simpler than other methods, which implement such metallic layers based on the extensive wafer-to-wafer bonding technique.

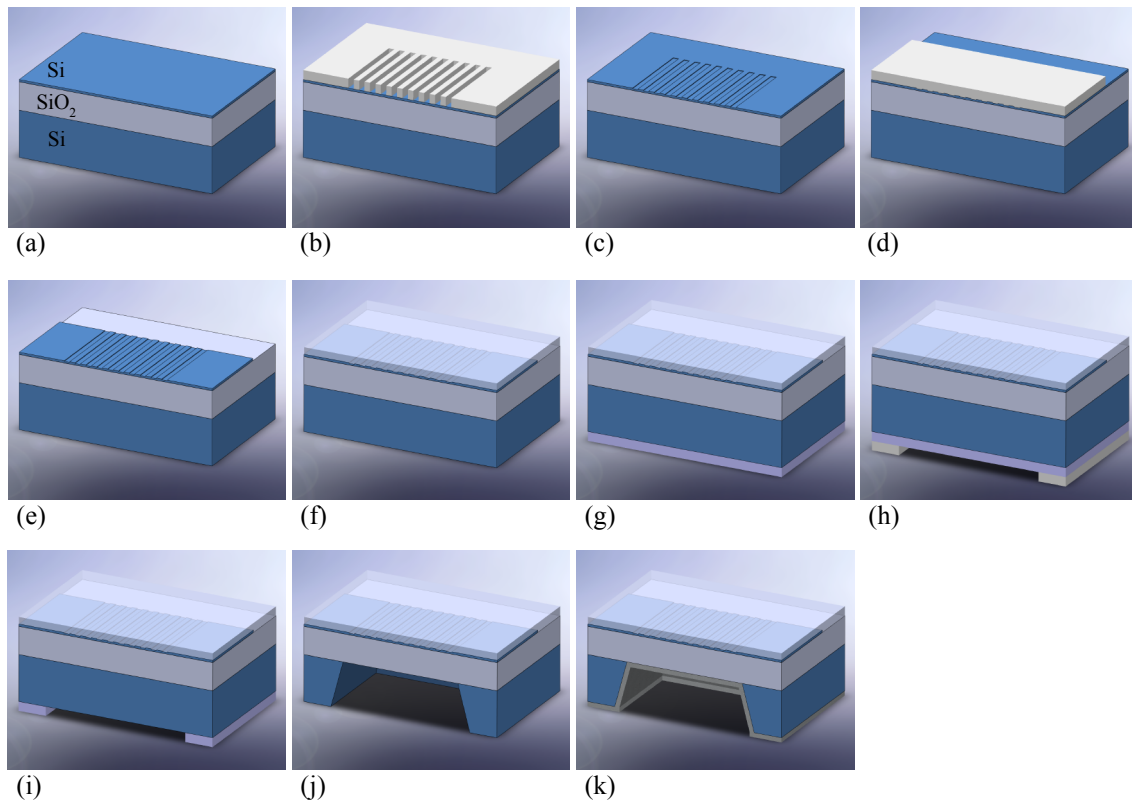


Figure 5.13: Cross-sectional 3D illustration of the technological process flow including the steps: (a) initial SOI wafer, (b) photoresist coating and exposure using an electron beam writer, (c) 70 nm depth etching, (d) second photoresist coating and exposure, (e) 250 nm depth etching, (f) top passivation, (g) hard mask backside deposition, (h) photoresist backside coating and exposure, (i) hard mask etching, (j) mirror cavity etching, and (k) metal deposition.

Figure 5.14 shows a microscopic picture of a fabricated structure including two identical grating couplers, which are connected by a 15 μm wide and 1 mm long waveguide and serve as input and output optical power interfaces. The insets represent a close-up of the mirrors front and backside. Due to reciprocity, coupling in from the fiber to the grating exhibits the same characteristics as coupling out from the grating to the fiber. In addition, the waveguide between both interfaces is designed with a large width so as to omit additional losses. Hence, this structure allows a simple determination of the grating efficiency by averaging the difference between the output and input power. When using thin waveguides to connect the gratings, the insertion loss of the tapers and these nano-

waveguides, especially caused by sidewall roughness, must also be taken into consideration as shown in appendix D.

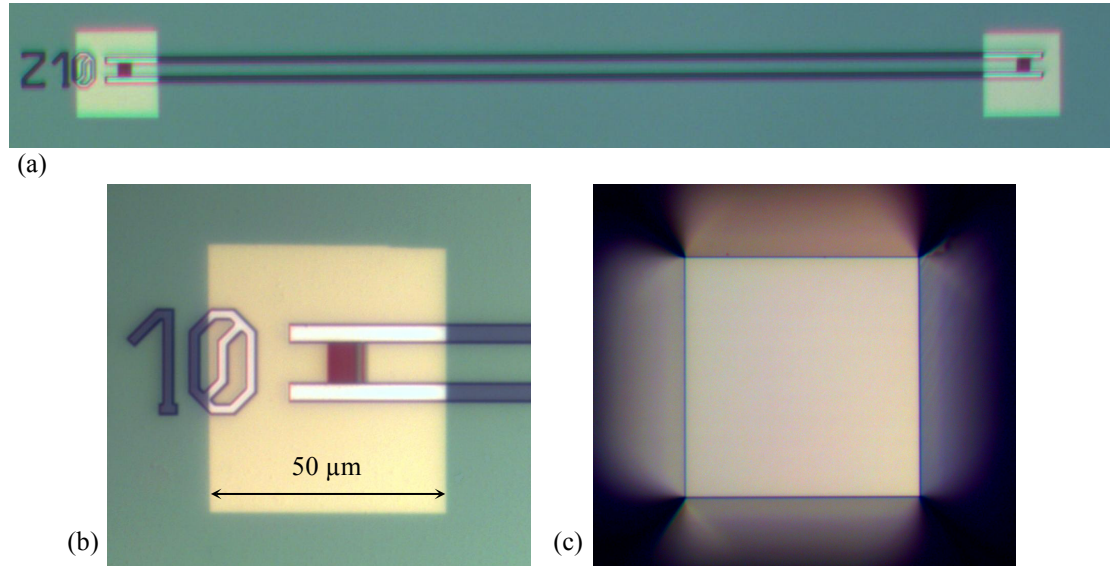


Figure 5.14: (a) Microscopic picture of a fabricated structure including two grating couplers with backside mirrors and linked by a waveguide. (b) Front and (c) backside view of the metal mirror.

5.6. Characterization of the structures

5.6.1. Measurement setup

In order to determine the coupling efficiency of the fabricated grating couplers, a measurement setup composed of a tunable laser source working in the wavelength range 1460 nm – 1580 nm, a polarization controller, and an optical power meter is used as depicted in Figure 5.15(a). The fibers are aligned on the input and output grating couplers in the three orthogonal directions by means of piezoelectric actuators. In order to prevent Fresnel reflections between the fibers and the gratings, a MIL with a refractive index of 1.4486 at 1550 nm is applied on the chip surface [121]. This nearly corresponds to the refractive index of the fiber and also of the cladding layer. Figure 5.15(b) illustrates the input and output fibers immersed in the MIL over the grating couplers. Using equation (4.25), it can be shown that the fiber MFD suffers an expansion of only 1% at a distance of 11 μm from the fiber end-face. Hence, the beam divergence can be

neglected as the fibers are positioned in the immediate vicinity of the 1 μm thick cladding.

As previously mentioned, the device under test (DUT) is composed of two identical gratings linked by a waveguide of the same width as these gratings with negligible insertion losses. Thus, the measured coupling efficiency in dB can be expressed as

$$\eta_{GC} = -\frac{1}{2}(P_{L,\text{dBm}} - P_{P,\text{dBm}} - a_S), \quad (5.17)$$

where $P_{L,\text{dBm}}$ is the laser optical input power in dBm, $P_{P,\text{dBm}}$ is the measured optical output power at the power meter in dBm, and a_S is the setup loss in dB including connectors and polarization controller losses. The latter factor is determined by directly connecting the laser source to the power meter through the polarization controller and calculating the average difference between the output and input power for each wavelength at different polarization states.

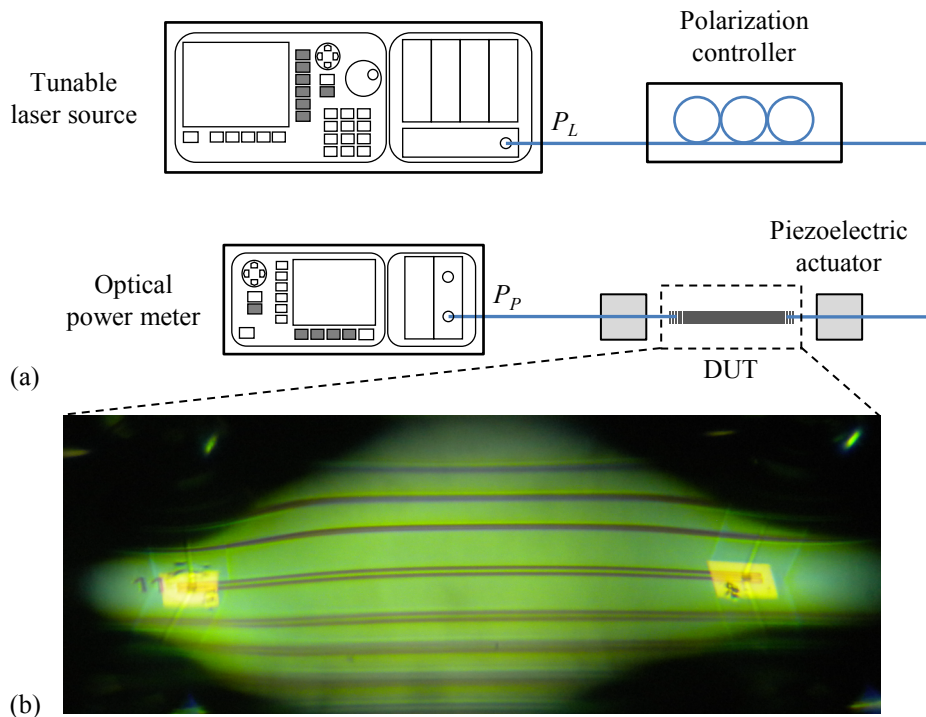


Figure 5.15: (a) Graphical representation of the measurement setup for the characterization of the fabricated grating couplers. (b) Microscopic picture of two fibers immersed in the MIL and positioned in the immediate vicinity of the grating couplers.

5.6.2. Periodic grating couplers

After calibrating the setup for the determination of the loss factor a_S , the measurement of the integrated structures is realized first by actively positioning the fibers on the gratings at the adjusted off-vertical tilt angle and the target wavelength. Afterwards, the TE polarization at the end-face of the input fiber is set up by using the polarization controller and monitoring the transmitted optical power through the structure to the power meter. In fact, since the designed 1D gratings serve as polarization filters with a rejection higher than 20 dB, the maximal coupling efficiency can only be achieved for the TE polarization. Coupling of the TM polarization to the 1st diffraction order can be realized using larger periods in the order of 860 nm for the operating wavelength 1550 nm or to the -1st order using larger tilt angles as shown in the appendices E.1 and E.2 respectively. It should be noted that both routines of adjusting the fiber position and the desired polarization state have to be repeated until no further increase of the received optical power is observed. Finally, the wavelength is swept over the specified range, and the coupling efficiency is calculated according to (5.17).

Figure 5.16(a) shows an SEM picture of a periodic grating on the chip after the removal of the top passivation layer. As previously mentioned, the theoretical coupling efficiency of uniform gratings with a backside mirror is around -0.9 dB; however, the highest experimentally achieved value in literature reaches only -1.6 dB [111], [113]. Thus, it is necessary to investigate the limit of these structures owing to their simple design and fabrication. Figure 5.16(b) illustrates the measured spectral efficiency of a periodic grating with $\Lambda = 600$ nm and $w_{GC} = 15$ μ m at different off-vertical tilt angles. At 9°, the efficiency reaches its maximum -1.08 dB at 1551 nm, which is in agreement with theoretical calculations. The difference to the simulation result is lower than 0.2 dB and demonstrates the high quality of the fabrication process. Furthermore, the 1 dB and 3 dB bandwidths achieved are larger than 42 nm and 73 nm respectively.

In the wavelength range considered, the efficiency maxima are identical within a margin of less than 0.1 dB, whereas the wavelength difference amounts to roughly 15 nm per degree. Hence, α_i represents an important parameter that can compensate for fabrication tolerances while covering a large wavelength range. The second important parameter when designing uniform gratings is Λ . Figure 5.16(c) illustrates the measured efficiency

behavior for different periods at $\alpha_i = 9^\circ$. The wavelength difference of the efficiency maxima is around 25 nm for $\Delta\Lambda = 10$ nm, which means that varying the period within less than 15 nm enables coupling in the whole C-band.

In both graphs, there are spectral ripples to be observed with an amplitude that depends on the investigated structure and the wavelength range, whereas the FSR is constant and amounts to 1.4 nm. Using equation (3.31), this value yields a resonator length of around 280 μm , which corresponds to the writing field size of the used electron beam system [122]. Hence, the Fabry-Pérot resonances do not originate from the designed gratings and are caused by reflections at stitching errors between adjacent exposure fields along the connecting waveguides.

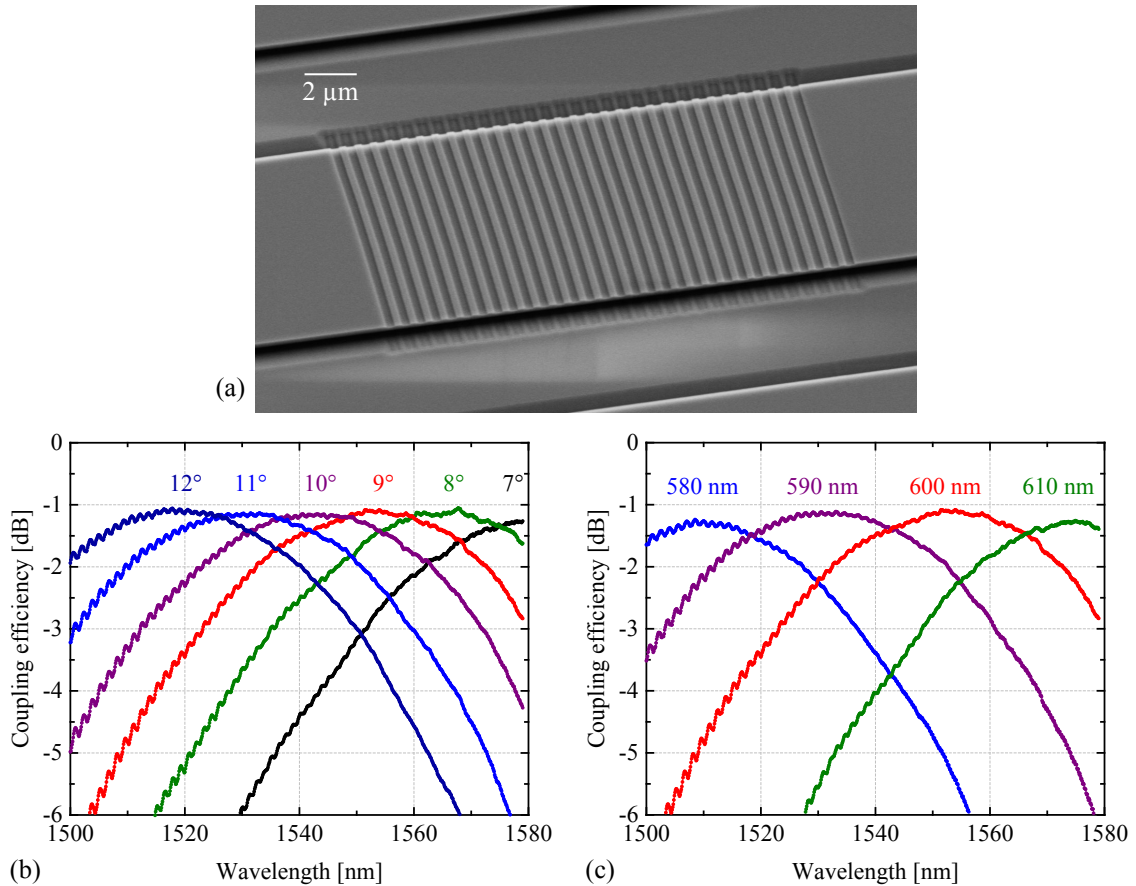


Figure 5.16: (a) SEM picture of a periodic grating on the chip. (b) Measured coupling efficiency of a grating with $\Lambda = 600$ nm and $w_{GC} = 15$ μm at different off-vertical tilt angles. (c) Measured coupling efficiency of grating couplers with different periods at $\alpha_i = 9^\circ$.

5.6.3. Aperiodic grating couplers

The aperiodic grating coupler GC_2 is fabricated on the same chip as the uniform structures previously investigated and is depicted in Figure 5.17. This grating has dimensions of $15\ \mu\text{m} \times 15.2\ \mu\text{m}$, which reveals the advantage of compactness in comparison to other coupling techniques such as SSCs. The critical groove and rib lengths amount to $g_{min} = 60\ \text{nm}$ and $b_{min} = 115\ \text{nm}$ respectively and are shown to be properly fabricated in the insets. The calculated theoretical coupling efficiency of this structure is $-0.33\ \text{dB}$ at the wavelength $1550\ \text{nm}$.

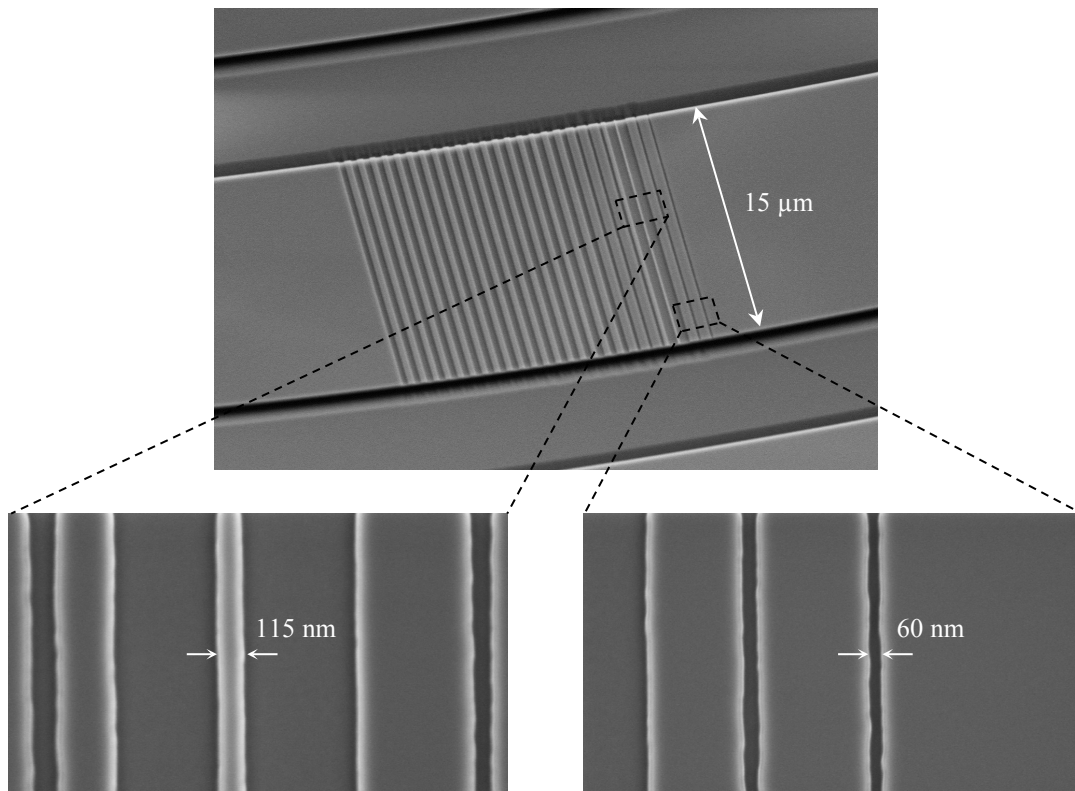


Figure 5.17: SEM picture of the designed grating coupler GC_2 . The insets show the corresponding critical dimensions with minimal rib and groove lengths of $115\ \text{nm}$ and $60\ \text{nm}$ respectively.

Figure 5.18(a) represents a comparison between the theoretical and experimental efficiency spectra of the designed grating coupler GC_2 at $\alpha_i = 9^\circ$. Both curves are in excellent agreement with a transmission peak in the proximity of the target wavelength, except for the $0.4\ \text{dB}$ lower measured efficiency. This difference, which is slightly larger

than in the case of uniform gratings, originates partly from the wafer properties variation and partly from some fabrication deviations, especially of the critical grooves and ribs. In addition, the simulations are based on 2D calculations, whereas the measured grating has a defined width of 15 μm in the lateral direction. Thus, the efficiency may be improved when the width value is optimized accordingly. Nevertheless, the measured efficiency at the adjusted angle of 9° still reaches a high value of -0.73 dB at 1552 nm with a 1 dB bandwidth larger than 38 nm.

In order to investigate the origin of the discrepancy, the wafer properties are analyzed. For this purpose, the thicknesses of the top Si layer and the BOX are characterized by means of spectroscopic ellipsometry and illustrated in Figures 5.18(b) and 5.18(c). While the thickness of the film layer shows values between 248 nm and 250 nm in a large area of the wafer, the BOX exhibits values around 2.96 μm , which are much smaller than the nominal thickness of 3 μm . Hence, the maximum efficiency tends to shift to smaller wavelengths, and therefore to larger angles.

The structure is measured at $\alpha_i > 9^\circ$, and the obtained curves are illustrated in Figure 5.18(d). In fact, the coupling efficiency increases to -0.67 dB at 1540 nm and 10° , whereas it attains its maximum of -0.62 dB at 1531 nm and 11° with a large bandwidth of $\Delta\lambda_{1\text{dB}} = 40$ nm and $\Delta\lambda_{3\text{dB}} = 67$ nm. At 12° the value decreases and reaches -0.65 dB at 1517 nm. This means that the behavior is blue-shifted by nearly 20 nm due the 40 nm lower actual BOX thickness than assumed. Hence, nonuniform structures are more sensitive to parameter deviations than periodic structures as the grating profile is optimized for specific properties that may not easily be compensated. Nevertheless, at the target angle and wavelength, the grating still exhibits a record efficiency with a large bandwidth.

It should be noted that the measurement accuracy is within close range of ± 0.02 dB owing to the high precision of the used setup and the simple designed configurations. When using structures with additional tapers and narrow waveguides with a width of 400 nm for example, extra attention must be given since more insertion loss factors have to be determined beforehand and may decrease the accuracy of the calculated grating coupler efficiency.

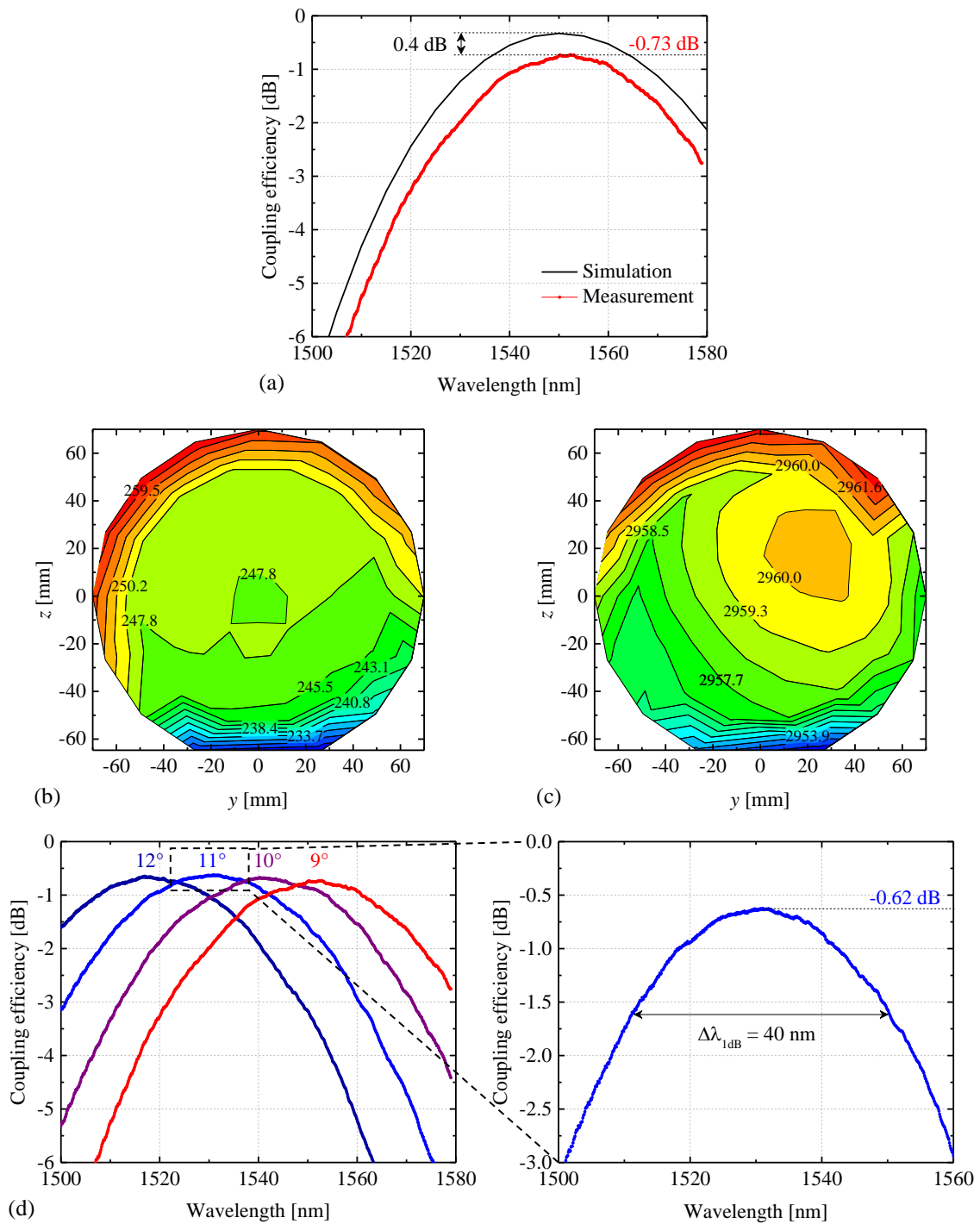


Figure 5.18: (a) Simulated and measured efficiency spectra of GC₂ at $\alpha_i = 9^\circ$. Characterized (b) top Si layer and (c) BOX thickness over the whole wafer in nm based on ellipsometric measurements. (d) Measured spectral efficiency of GC₂ at different angles. The inset is a zoom-in of the coupling efficiency spectrum at 11° .

Another wafer property that has to be investigated is the variation of the Si substrate thickness. According to [115], this parameter varies in a range of $625 \mu\text{m} \pm 15 \mu\text{m}$. Indeed, the fluctuation of the substrate thickness does not directly affect the grating as much as the BOX layer, but it can cause some constraints to the mirror fabrication, and hence to the reproducibility of the high efficiency over the whole wafer. For this purpose, the same configuration including the grating couplers GC₂ is placed on different positions on the wafer, and all 19 structures are characterized separately.

Figure 5.19 illustrates the measured spectral efficiencies and the corresponding microscopic pictures of some fabricated mirrors. It is clear that 14 gratings exhibit a high coupling efficiency of more than -0.75 dB , whereas the remaining 5 structures have an inferior performance, giving a yield of nearly 75%. The gratings with the lower efficiency possess poor quality mirrors as can be observed in the inset of Figure 5.19. In fact, due to the substrate thickness fluctuation, some residuals can persist in the cavity windows after the backside etching step, and thus the metal deposition is not realized properly. These remaining Si clusters increase the optical path above the mirrors and prevent the constructive interference of the reflected optical power part with the diffracted part toward the waveguide. This problem can be solved, however, by overetching the substrate without affecting the BOX layer.

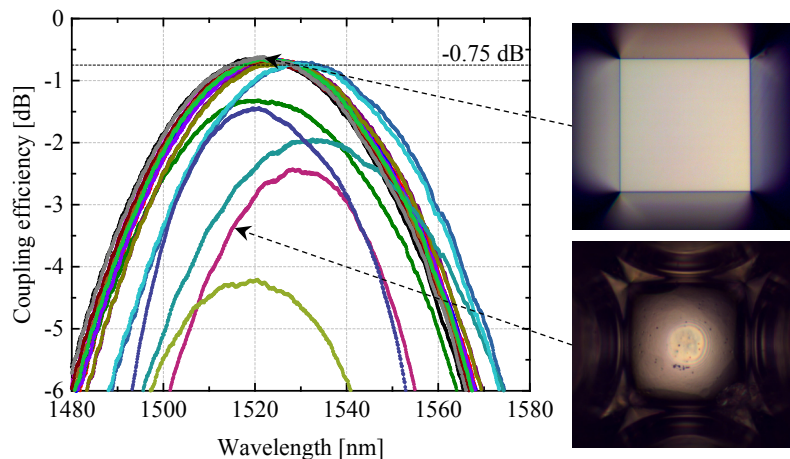


Figure 5.19: Measured spectral efficiency of the 19 fabricated grating couplers GC₂ on the whole wafer. The insets show a microscopic picture of two backside mirrors at different positions on the wafer. Top: membrane window with a perfect mirror; bottom: window with a defect mirror.

Finally, the grating coupler GC₃ with the relaxed minimal groove and rib lengths $g_{min} = 110$ nm and $b_{min} = 115$ nm respectively is characterized. This structure is fabricated on the same chip as the structures previously described with the help of an electron beam writer, but it can also be realized optically using deep UV lithography for example. Figure 5.20 represents the measured efficiency spectra of the grating for different w_{GC} values ranging from 10 μm to 40 μm . It is clear that even with a larger minimal rib width of 115 nm the grating still exhibits a high efficiency of -0.73 dB at 1531 nm with a 1 dB bandwidth of 37 nm. This value is measured using $w_{GC} = 15$ μm and decreases to -1.07 dB for a width of 10 μm and to -1.56 dB for 20 μm . Thus, optimizing the modal overlap in the lateral direction is an important parameter that cannot be neglected and has to be further investigated.

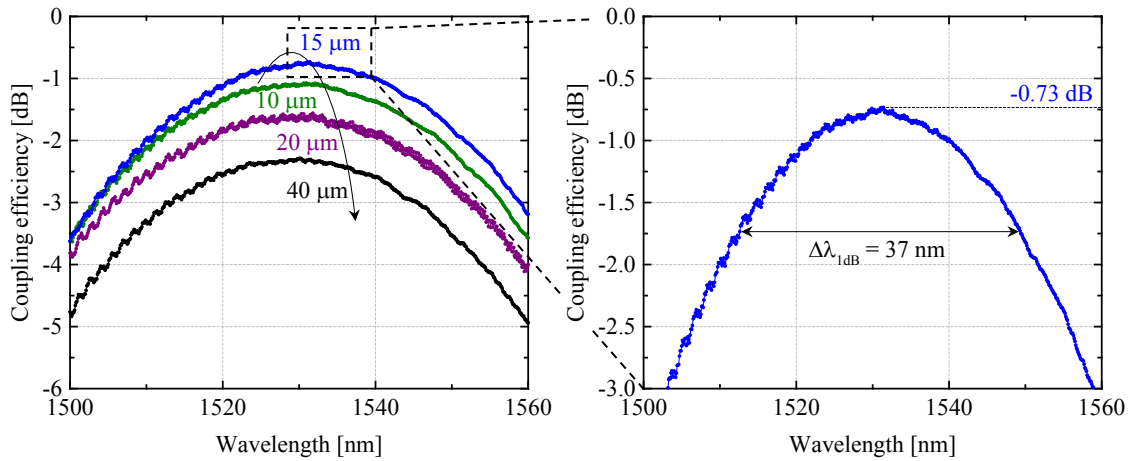


Figure 5.20: Measured efficiency spectra of the grating coupler GC₃ at $\alpha_i = 11^\circ$ for different width values. The inset is a zoom-in of the curve using $w_{GC} = 15$ μm .

5.7. Conclusion

The realization of highly efficient gratings to couple light between optical fibers and photonic integrated waveguides based on the Bragg diffraction effect necessitates a careful design of several parameters. Starting from standard periodic structures, the first optimization step deals with the choice of the adequate BOX thickness in order to guarantee constructive interference between the downward optical power part and the part diffracted to the waveguide. In fact, the coupling mechanism is unfortunately combined

with excitation of the 0th diffraction order, and hence there is a considerable amount of light transmitted to the substrate in addition to the upward reflection. The substrate losses then, secondly, have to be recycled, which is done by integrating backside mirrors underneath the gratings below the BOX layer. Finally, the upward reflection losses are minimized by improving the modal overlap between the grating and fiber profile along the lateral and longitudinal directions. This is realized by adjusting the grating width and by optimizing the individual groove and rib lengths while considering the minimal manufacturable dimensions.

The fabrication is achieved at IMS CHIPS according to a CMOS-compatible process, and the platform used is a standard SOITEC wafer with a BOX thickness that fulfills the requirements for high-performance grating couplers. A comparison between the simulated and measured results of the designed uniform and nonuniform grating couplers is illustrated in Figure 5.21. At the target telecommunication wavelength of 1550 nm, the optimized structure achieves a theoretical coupling efficiency of -0.33 dB and a measured value of -0.74 dB, representing an improvement of nearly 2 dB to standard grating couplers.

At a slightly larger angle and lower wavelength, the same structure also exhibits a record efficiency of -0.62 dB, which is the highest measured coupling efficiency between SMFs and PICs based on diffraction gratings up to date.

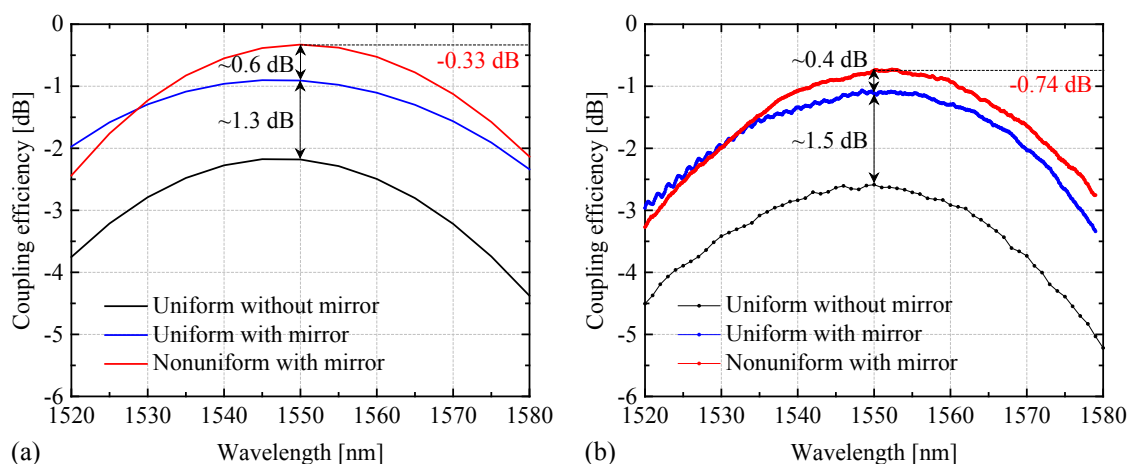


Figure 5.21: (a) Simulated versus (b) measured efficiency spectra of designed uniform and nonuniform grating couplers with and without a metal mirror underneath.

6. Summary and outlook

6.1. Summary

Coupling from optical fibers to photonic integrated circuits, especially in the SOI platform, is not a trivial task due to the large dimension mismatch between the fiber core and the nanowaveguides on the chip. There certainly exist several approaches to solve this issue based for example on 3D tapers or dielectric lenses, but with many disadvantages. The main requirements for the realization of efficient nanocouplers are high transmission from the fiber to the waveguide, large bandwidth, and compactness.

In this thesis, two different coupling techniques are adopted. The first method relies on the emerging field of metamaterials, whereas the second method is based on diffraction Bragg gratings. The main difference between both approaches depends on the interaction of the electromagnetic waves with the constituting unit cells. While metamaterials gain their properties from the overall response rather than from the subwavelength individual elements, Bragg gratings take advantage of diffraction since the period is in the order of the wavelength.

The investigation of focusing negative index metamaterials is done in the millimeter wave range owing to the simplicity of the fabrication and characterization. The implementation of such structures starts with the optimization of the unit cell parameters and the coupling between the functional layers to realize highly efficient planar structures. At a frequency of 38.5 GHz, the fabricated multilayer exhibits a high transmission of -0.5 dB and a negative refractive index of -1 . Second, the shape of the stack is modified following a spherical curvature, and a focusing negative index plano-concave lens is fabricated. This configuration shows a reduction of the launched beam width by a factor of more than 2 at a distance of only $6 \lambda_0$ from the metamaterial interface. Hence, very compact and highly efficient coupling is possible using the proposed NIM, which also outperforms standard dielectric lenses.

In order to verify the coupling behavior at telecommunication wavelengths, the dimensions of the NIM lens are scaled down by a factor of 5×10^3 . In this case, the absorption losses of the metal become considerable, and the transmission of the multilayer decreases significantly to lower than -10 dB. When reducing the number of layers further, the coupling efficiency can be improved and is estimated to around -2 dB, but this is still lower than the target value of -1 dB.

Indeed, the field of metamaterials offers the advantage of molding the flow of light in a flexible manner with numerous possible applications such as focusing and coupling. However, these benefits can only be meaningfully used at frequencies where the metal absorption is negligible, e.g. at radio frequencies. Thus, at infrared wavelengths focusing based on NIMs is not the adequate solution for the coupling issue due to these metal losses.

The second approach adopted in this thesis deals with the direct realization of coupling gratings to operate at telecommunication wavelengths. These structures have the advantage in comparison to the first investigated technique of being fabricated with the integrated waveguides on the chip, but they necessitate a higher optimization effort. The first step relies on improving the directionality by implementing a mirror at an adequate distance from the film layer. Furthermore, the modal overlap to the fiber profile is enhanced by calculating the exact length of the individual grooves and ribs.

The fabricated grating coupler with an Al mirror underneath exhibits unprecedented results with a record coupling efficiency of -0.62 dB at 1531 nm, which is the highest measured value so far, and a large 1 dB bandwidth of 40 nm. In addition, the grating has very compact dimensions as small as $15 \mu\text{m} \times 15.2 \mu\text{m}$ and can be connected to the nanowaveguides by means of adiabatic tapers or other focusing schemes. The structures are fabricated in a CMOS-compatible technological process, and the metal mirrors are integrated cost-effectively without the need for wafer bonding techniques.

Thus, in summary, Bragg gratings offer the possibility of highly efficient coupling, which exceeds the performance of focusing metamaterials. In addition, the compactness of these structures makes them more favorable than other standard coupling techniques such as SSCs despite the slightly lower efficiency. Nevertheless, the theoretical results

predict efficiencies even better than -0.3 dB, which can be certainly achieved when optimizing the fabrication process.

6.2. Outlook

Despite the notable losses in metamaterials due to the absorptive behavior of metals at optical frequencies, this field remains interesting as it enables the achievement of arbitrary electromagnetic properties that can initiate novel effects not found in nature. Thus, in order to make use of metamaterials in the infrared and visible range, the use of conventional metals has to be replaced by other alternative materials with lower losses such as transparent conducting oxides [105] or enhanced by loss-compensating active media [104].

For the application of nanocoupling between optical fibers and integrated waveguides, diffractive gratings have been proven to exhibit higher performance and more advantages than any other coupling technique. Indeed, the achievable bandwidth can cover the totality of one telecommunication band; however, covering more bands can be realized only by changing the fiber tilt angle or by implementing particular structures with larger loss penalty. Here the use of active media can also be advantageous as the fiber can be kept fixed while the transmission peak is tuned over the wavelength. This can be done for example by doping the grating region in order to achieve a refractive index change when applying an electric field, and hence a change of the operating wavelength.

Appendix

A. Diffraction at different slit apertures

The intensity distribution of a diffracted wave having a wavenumber k on an aperture of an area A is proportional to the Fraunhofer integral as follows

$$I = C \left| \int_A e^{-j\vec{k}\vec{r}} dA \right|^2, \quad (\text{A.1})$$

where C is a constant. Thus, the diffraction pattern depends solely on the aperture geometry and the wave properties. In the following subsections, the intensity distribution of three different configurations is shown.

A.1. Rectangular single-slit aperture

In the case of a sufficiently long, rectangular single-slit aperture with a width w and a length l , the intensity can be expressed as

$$I = C \left| \int_{-w/2}^{w/2} e^{-jk(r_0 + y \sin \alpha_m)} l dy \right|^2 = C \left| e^{-jkr_0} \int_{-w/2}^{w/2} u(y) l dy \right|^2 \quad \text{with } u(y) = e^{-jky \sin \alpha_m} \quad (\text{A.2})$$

$$= C' \left| e^{-jkr_0} \right|^2 \left| \frac{1}{-jk \sin \alpha_m} [u(y)]_{-w/2}^{w/2} \right|^2 = C' \left| \frac{1}{-jk \sin \alpha_m} (u(w/2) - u(-w/2)) \right|^2 \quad (\text{A.3})$$

$$= C' \left| \frac{-2j \sin \left(k \frac{w}{2} \sin \alpha_m \right)}{-jk \sin \alpha_m} \right|^2 = C' \left| \frac{w \sin \left(k \frac{w}{2} \sin \alpha_m \right)}{k \frac{w}{2} \sin \alpha_m} \right|^2 \quad (\text{A.4})$$

$$= C' w^2 \left(\frac{\sin \gamma_s}{\gamma_s} \right)^2 \quad \text{with } \gamma_s = \frac{1}{2} k w \sin \alpha_m \quad (\text{A.5})$$

$$\Rightarrow I = I_0 \left(\frac{\sin \gamma_s}{\gamma_s} \right)^2. \quad (\text{A.6})$$

A.2. Circular single-slit aperture

For a circular aperture of a diameter D , the intensity distribution is given as

$$I = C \left| \int_{-D/2}^{D/2} e^{-jk(r_0+y \sin \alpha_m)} 2\sqrt{\left(\frac{D}{2}\right)^2 - y^2} dy \right|^2 \quad (\text{A.7})$$

$$= C \left| -\frac{D^2}{2} e^{-jkr_0} \int_{-1}^1 e^{jk\frac{D}{2}Y \sin \alpha_m} \sqrt{1-Y^2} dY \right|^2 \quad \text{with } Y = -\frac{2}{D}y \quad (\text{A.8})$$

$$= C |e^{-jkr_0}|^2 \left| -\frac{D^2}{2} \int_{-1}^1 e^{j\gamma_c Y} \sqrt{1-Y^2} dY \right|^2 \quad \text{with } \gamma_c = k \frac{D}{2} \sin \alpha_m. \quad (\text{A.9})$$

Let $Y = \cos \theta \Rightarrow dY = -\sin \theta d\theta$. Then

$$I = C' \left| \int_0^\pi e^{j\gamma_c \cos \theta} \sqrt{1-\cos^2 \theta} \sin \theta d\theta \right|^2 = C' \left| \int_0^\pi e^{j\gamma_c \cos \theta} \sin^2 \theta d\theta \right|^2. \quad (\text{A.10})$$

$$\text{Let } u_1(\theta) = -\frac{1}{j\gamma_c} e^{j\gamma_c \cos \theta} \Rightarrow u_1'(\theta) = e^{j\gamma_c \cos \theta} \sin \theta,$$

$$\text{and } u_2(\theta) = \sin \theta \quad \Rightarrow u_2'(\theta) = \cos \theta.$$

Since $(u_1 u_2)' = u_1' u_2 + u_1 u_2'$, then $\int u_1' u_2 = u_1 u_2 - \int u_1 u_2'$. Thus,

$$\int e^{j\gamma_c \cos \theta} \sin^2 \theta d\theta = -\frac{1}{j\gamma_c} e^{j\gamma_c \cos \theta} \sin \theta - \int \left(-\frac{1}{j\gamma_c} e^{j\gamma_c \cos \theta} \right) \cos \theta d\theta, \quad (\text{A.11})$$

which yields

$$\begin{aligned} \int_0^\pi e^{j\gamma_c \cos \theta} \sin^2 \theta d\theta &= \underbrace{\left[\frac{-1}{j\gamma_c} e^{j\gamma_c \cos \theta} \sin \theta \right]_0^\pi}_{0} + \frac{1}{j\gamma_c} \int_0^\pi e^{j\gamma_c \cos \theta} \cos \theta d\theta \\ &= \frac{\pi - j}{\gamma_c \pi} \int_0^\pi e^{j\gamma_c \cos \theta} \cos \theta d\theta. \end{aligned} \quad (\text{A.12})$$

The expression $\frac{-j}{\pi} \int_0^\pi e^{j\gamma_c \cos\theta} \cos\theta d\theta$ is known as the Bessel function of the first kind of order 1 and is denoted by $J_1(\gamma_c)$ [123].

Hence,

$$\int_0^\pi e^{j\gamma_c \cos\theta} \sin^2\theta d\theta = \frac{\pi}{\gamma_c} J_1(\gamma_c), \quad (\text{A.13})$$

which yields

$$I = C' \pi^2 \left(\frac{J_1(\gamma_c)}{\gamma_c} \right)^2 \quad (\text{A.14})$$

$$\Rightarrow I = I_0 \left(\frac{J_1(\gamma_c)}{\gamma_c} \right)^2. \quad (\text{A.15})$$

A.3. N -slits aperture

The intensity distribution originating from diffraction of an incident wave at an angle α_i at N periodic, sufficiently long, rectangular slits of a width w each, a length l , and a period Λ is expressed as

$$I = C \left| \sum_{i=0}^{N-1} \int_{i\Lambda-w/2}^{i\Lambda+w/2} e^{-jk(r_0+y \sin \alpha_m - y \sin \alpha_i)} l dy \right|^2 \quad (\text{A.16})$$

$$= C \left| \sum_{i=0}^{N-1} e^{-jkr_0} \int_{i\Lambda-w/2}^{i\Lambda+w/2} u(y) l dy \right|^2 \quad \text{with } u(y) = e^{-jky(\sin \alpha_m - \sin \alpha_i)} \quad (\text{A.17})$$

$$= C' \left| e^{-jkr_0} \left(\int_{-w/2}^{w/2} u(y) dy + \int_{\Lambda-w/2}^{\Lambda+w/2} u(y) dy + \dots + \int_{(N-1)\Lambda-w/2}^{(N-1)\Lambda+w/2} u(y) dy \right) \right|^2 \quad (\text{A.18})$$

$$= C' \left| e^{-jkr_0} \right|^2 \left| \frac{1}{-jk(\sin \alpha_m - \sin \alpha_i)} \left([u(y)]_{-w/2}^{w/2} + [u(y)]_{\Lambda-w/2}^{\Lambda+w/2} + \dots + [u(y)]_{(N-1)\Lambda-w/2}^{(N-1)\Lambda+w/2} \right) \right|^2 \quad (\text{A.19})$$

$$= C' \left| \frac{1}{-jk(\sin \alpha_m - \sin \alpha_i)} \left(u\left(\frac{w}{2}\right) - u\left(-\frac{w}{2}\right) + u\left(\Lambda + \frac{w}{2}\right) - u\left(\Lambda - \frac{w}{2}\right) + \dots \right. \right. \quad (\text{A.20})$$

$$\left. \left. + u\left((N-1)\Lambda + \frac{w}{2}\right) - u\left((N-1)\Lambda - \frac{w}{2}\right) \right) \right|^2$$

$$= C' \left| \frac{1}{-jk(\sin \alpha_m - \sin \alpha_i)} \left(u\left(\frac{w}{2}\right) - u\left(-\frac{w}{2}\right) + u(\Lambda)u\left(\frac{w}{2}\right) - u(\Lambda)u\left(-\frac{w}{2}\right) + \dots \right. \right. \quad (\text{A.21})$$

$$\left. \left. + u\left((N-1)\Lambda\right)u\left(\frac{w}{2}\right) - u\left((N-1)\Lambda\right)u\left(-\frac{w}{2}\right) \right) \right|^2$$

$$= C' \left| \frac{1}{-jk(\sin \alpha_m - \sin \alpha_i)} \left(\left(u\left(\frac{w}{2}\right) - u\left(-\frac{w}{2}\right) \right) (1 + u(\Lambda) + \dots + u((N-1)\Lambda)) \right) \right|^2 \quad (\text{A.22})$$

$$= C' \left| \frac{-2j \sin \left(k \frac{w}{2} (\sin \alpha_m - \sin \alpha_i) \right)}{-jk(\sin \alpha_m - \sin \alpha_i)} \cdot \frac{1 - e^{-jNk\Lambda(\sin \alpha_m - \sin \alpha_i)}}{1 - e^{-jk\Lambda(\sin \alpha_m - \sin \alpha_i)}} \right|^2 \quad (\text{A.23})$$

$$= C' \left| \frac{w \sin \left(k \frac{w}{2} (\sin \alpha_m - \sin \alpha_i) \right)}{k \frac{w}{2} (\sin \alpha_m - \sin \alpha_i)} \right|^2 \cdot \left| \frac{e^{-jNk \frac{\Lambda}{2} (\sin \alpha_m - \sin \alpha_i)} \left(e^{jNk \frac{\Lambda}{2} (\sin \alpha_m - \sin \alpha_i)} - e^{-jNk \frac{\Lambda}{2} (\sin \alpha_m - \sin \alpha_i)} \right)}{e^{-jk \frac{\Lambda}{2} (\sin \alpha_m - \sin \alpha_i)} \left(e^{jk \frac{\Lambda}{2} (\sin \alpha_m - \sin \alpha_i)} - e^{-jk \frac{\Lambda}{2} (\sin \alpha_m - \sin \alpha_i)} \right)} \right|^2 \quad (\text{A.24})$$

$$= C' \left| \frac{w \sin \left(k \frac{w}{2} (\sin \alpha_m - \sin \alpha_i) \right)}{k \frac{w}{2} (\sin \alpha_m - \sin \alpha_i)} \right|^2 \cdot \underbrace{\left| \frac{e^{-jNk \frac{\Lambda}{2} (\sin \alpha_m - \sin \alpha_i)}}{e^{-jk \frac{\Lambda}{2} (\sin \alpha_m - \sin \alpha_i)}} \right|^2}_1 \quad (\text{A.25})$$

$$\left| \frac{2j \sin \left(Nk \frac{\Lambda}{2} (\sin \alpha_m - \sin \alpha_i) \right)}{2j \sin \left(k \frac{\Lambda}{2} (\sin \alpha_m - \sin \alpha_i) \right)} \right|^2$$

$$= C' w^2 \left(\frac{\sin \gamma_s}{\gamma_s} \right)^2 \left(\frac{\sin N \gamma_n}{\sin \gamma_n} \right)^2 \quad (\text{A.26})$$

with $\gamma_s = \frac{1}{2} k w (\sin \alpha_m - \sin \alpha_i)$ and $\gamma_n = \frac{1}{2} k \Lambda (\sin \alpha_m - \sin \alpha_i)$

$$\Rightarrow I = I_0 \left(\frac{\sin \gamma_s}{\gamma_s} \right)^2 \left(\frac{\sin N \gamma_n}{\sin \gamma_n} \right)^2 \quad (\text{A.27})$$

B. Equivalent LC circuit of a fishnet NIM

In order to obtain a metamaterial with a negative refractive index, the unit cell has to be designed so that $Re(\epsilon_r) < 0$ and $Re(\mu_r) < 0$ are in the same frequency range. While the negative permittivity is obtained using periodically structured metallic wires, the negative permeability is generated by exciting circular currents that produce a magnetic resonance. Using a single layer of the adopted fishnet structure in this thesis with the parameters $\Lambda = 4.9$ mm, $R_m = 2.3$ mm, and $w_m = 1.45$ mm, it is clear that the current density on the substrate surfaces reaches high values at a frequency of 36.8 GHz with three virtual loops as shown in Figure B.1(a). These loops in the upper, middle, and bottom part of the unit cell can be represented by the inductances L_u , L_m , and L_b , which depend on the geometrical parameters of the unit cell and can be summarized in a total inductance L . On the other hand, both metallic sheets separated by the substrate layer represent a capacitor C , and hence the overall response can be described by an inductive-capacitive behavior with a magnetic resonance $\omega_m = 1/\sqrt{LC}$ [124].

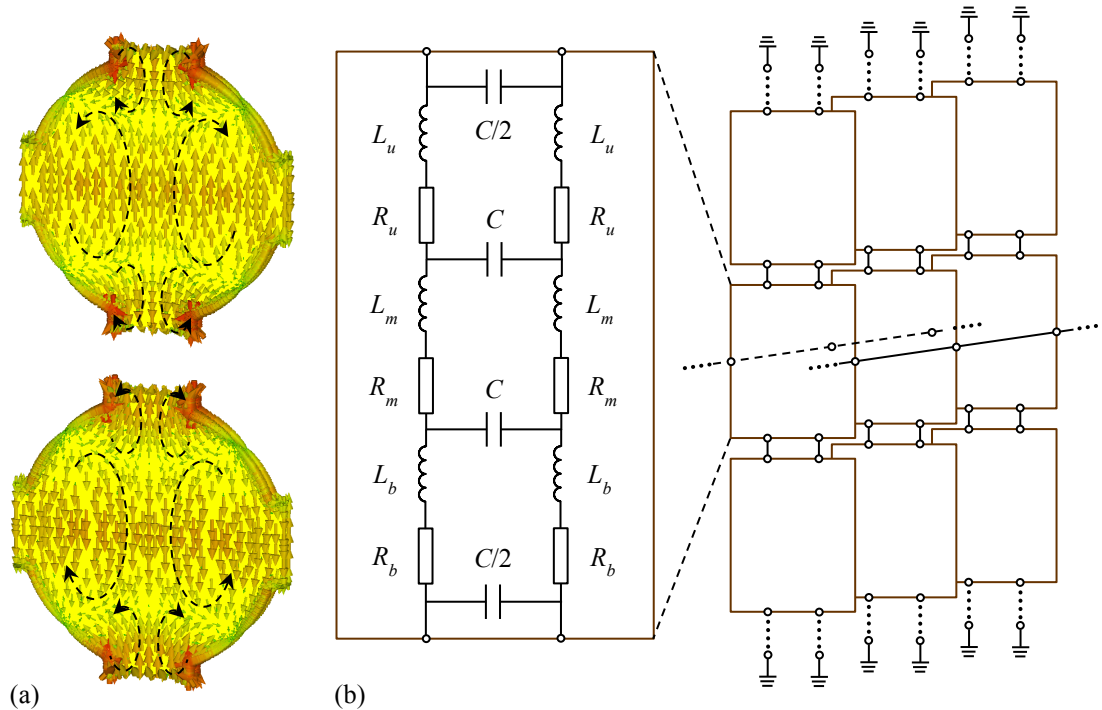


Figure B.1: (a) Current density distribution on the substrate surfaces of a unit cell with $\Lambda = 4.9$ mm, $R_m = 2.3$ mm, and $w_m = 1.45$ mm at 36.8 GHz.

(b) Corresponding equivalent circuit of the metamaterial.

Figure B.1(b) illustrates the equivalent circuit of the single layer with the parameters mentioned above. Due to the additional substrate and metal losses, the elementary LC circuit is extended by the resistances R_u , R_m , and R_b . Using the values $L_u = L_b = 0.1$ nH, $L_m = 0.212$ nH, $C = 0.06$ fF, and $R_u = R_m = R_b = 10$ Ω , the obtained amplitude and phase of the simulated S-parameters using the commercial software Agilent Advanced Design System (ADS) are illustrated in Figures B.2(a) and B.2(b). It is clear that the results agree well with the CST simulations and demonstrate the effect of the LC behavior on the overall metamaterial response to achieve a magnetic resonance. In addition, the retrieved internal properties are depicted in Figures B.2(c) and B.2(d) and show the presence of a common frequency range with $Re(\underline{\epsilon}_r) < 0$ and $Re(\underline{\mu}_r) < 0$, and hence $Re(\underline{n}) < 0$.

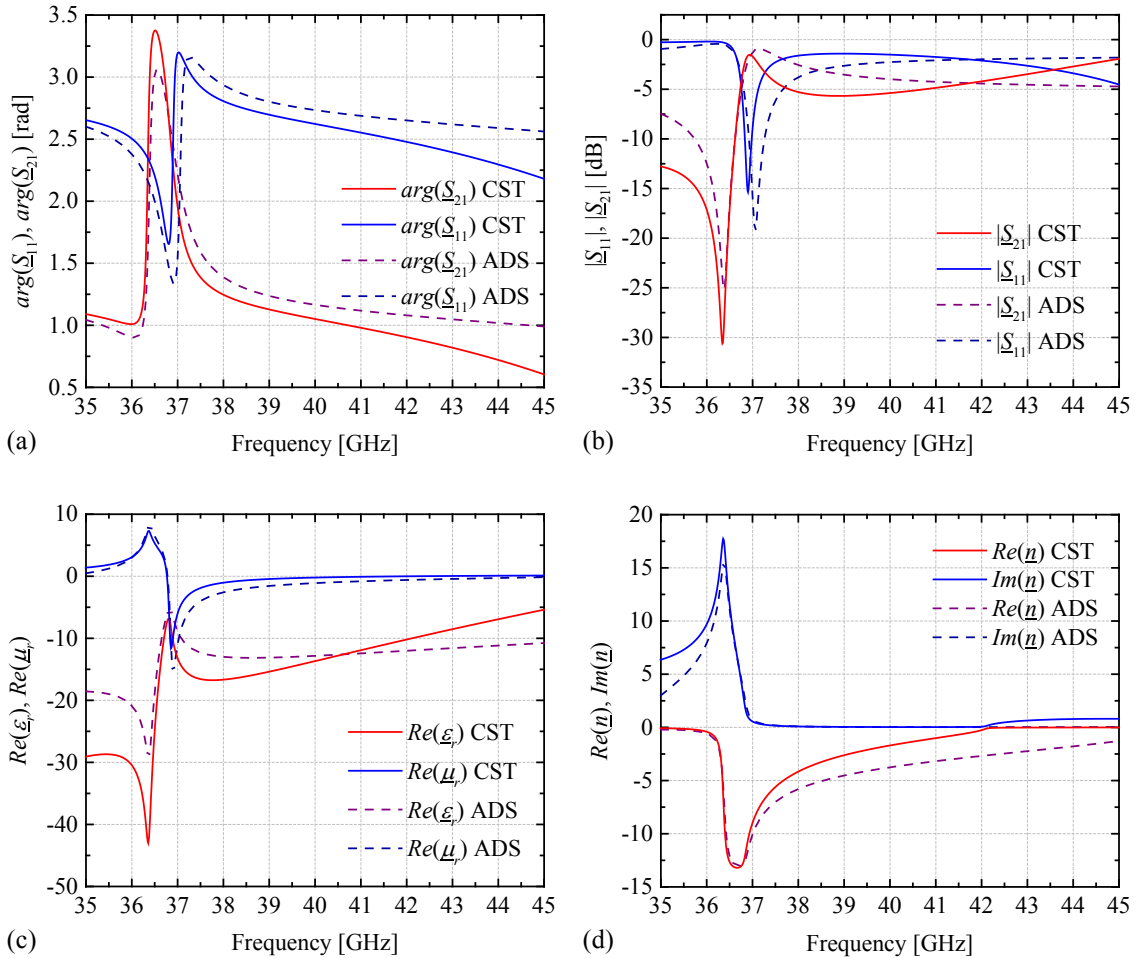


Figure B.2: Comparison between the simulated (a) amplitude and (b) phase of the S-parameters and the retrieved (c) real part of the permittivity, permeability, and (d) complex refractive index using CST MWS and ADS.

C. Design of an aspheric lens at radio frequencies

The dielectric plano-convex lens is designed based on a hyperbolic shape in order to eliminate any spherical aberrations. The design of the aspheric lens is realized following the theoretical calculations in [125].

The used dielectric is a Teflon substrate with a relative permittivity $\epsilon_r = 2.1$ and a thickness $T = 10.8$ mm. The diameter of the lens is chosen as $D = 72$ mm to have almost the same area as the plano-concave NIM lens. Thus, the 3D form of the lens is fully described using the equation

$$x^2 + y^2 = (\epsilon_r - 1)z^2 + 2F(\sqrt{\epsilon_r} - 1)z, \quad (\text{C.1})$$

and a graphical representation of the structure is shown in Figure C.1. The focal length of the lens can then be determined to

$$F = \frac{1}{2} \frac{T}{\sqrt{\epsilon_r} - 1} \left[\left(\frac{D}{2T} \right)^2 - \epsilon_r + 1 \right], \quad (\text{C.2})$$

which gives $F = 120.4$ mm and FFL = 109.6 mm. The FFL of the fabricated structure is measured to a smaller value of nearly 95 mm, which can be attributed to fabrication deviations of the hyperbolic surface.

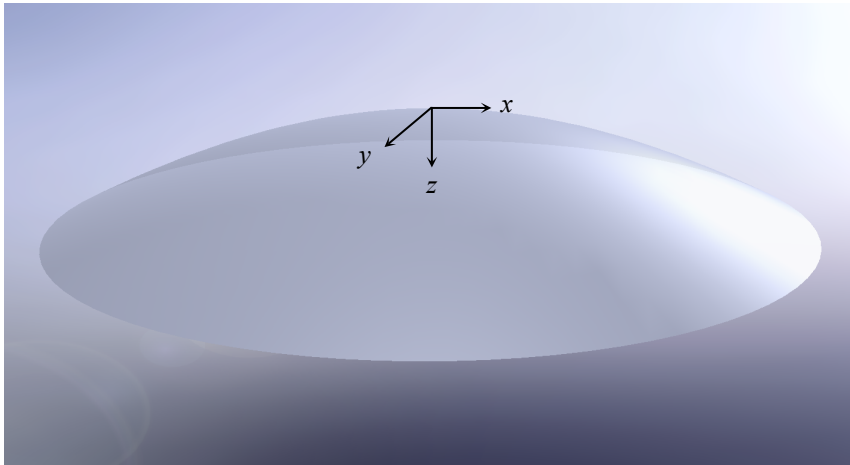


Figure C.1: Schematic drawing of the designed plano-convex dielectric lens.

D. Waveguide losses

In order to determine the exact coupling efficiency of the fabricated grating couplers, different loss factors, including the insertion loss of the setup and the waveguiding structures on the chip, have to be taken into consideration. As the input and output gratings are generally connected by a thin waveguide of a length L_W , the additional losses of the tapers $2a_T$ and of the waveguide $a_W L_W$ have to be measured separately. The coupling efficiency is then determined as follows

$$\eta_{GC} = -\frac{1}{2} (P_{L,\text{dBm}} - P_{P,\text{dBm}} - a_S - 2a_T - a_W L_W). \quad (\text{D.1})$$

When using a waveguide of the same width as the gratings, the tapers are saved and only the waveguide losses may play a role. By varying the waveguide length and averaging the fiber-to-fiber transmission, the waveguide loss per length a_W can be then calculated from the slope of the curve since

$$P_{P,\text{dBm}} - P_{L,\text{dBm}} = -a_W L_W + 2\eta_{GC} - a_S. \quad (\text{D.2})$$

Figure D.1(a) illustrates a structure composed of two gratings linked by a waveguide with a width of 14 μm . The measured transmission as a function of the waveguide length at a wavelength of 1550 nm is depicted in Figure D.1(b), and the waveguide loss per length is calculated to $a_W = 0.06$ dB/mm. Thus, for relatively large widths these losses are negligible and the grating coupler efficiency can be determined directly from the difference of the input and output optical powers after subtracting the setup losses.

When the waveguide width is decreased, the losses increase dramatically due to the stronger interaction of the fundamental mode with the waveguide faces, especially for the TE polarization. Here the sidewall roughness caused by the fabrication process and the stitching errors of the electron beam writer represent scattering centers for the guided electromagnetic wave. Figure D.2(a) represents a microscopic picture of a structure composed of two gratings linked by a thin waveguide with a width of 400 nm and two adiabatic tapers. The measured transmission as a function of the waveguide length at a wavelength of 1550 nm is depicted in Figure D.2(b), and the waveguide loss per length is calculated to $a_W = 1.2$ dB/mm. It should be noted that this loss factor is smaller for

TM than for TE since the electric field interacts with the top and bottom waveguide faces rather than with the sidewalls.

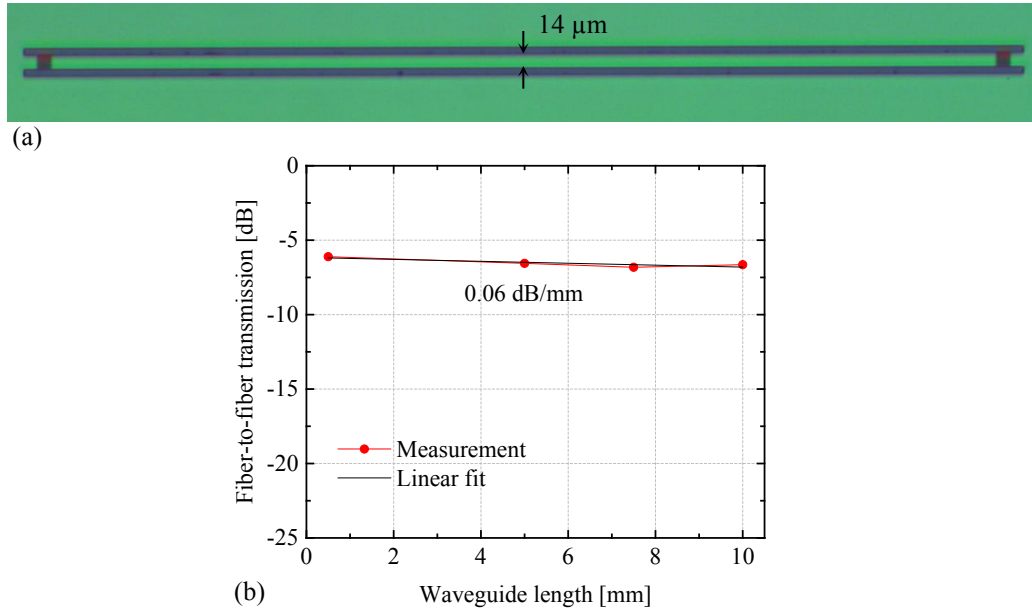


Figure D.1: (a) Microscopic picture of a structure composed of two gratings linked by a waveguide with a width of $14\ \mu\text{m}$. (b) Measured transmission as a function of the waveguide length at $1550\ \text{nm}$ for TE polarization.

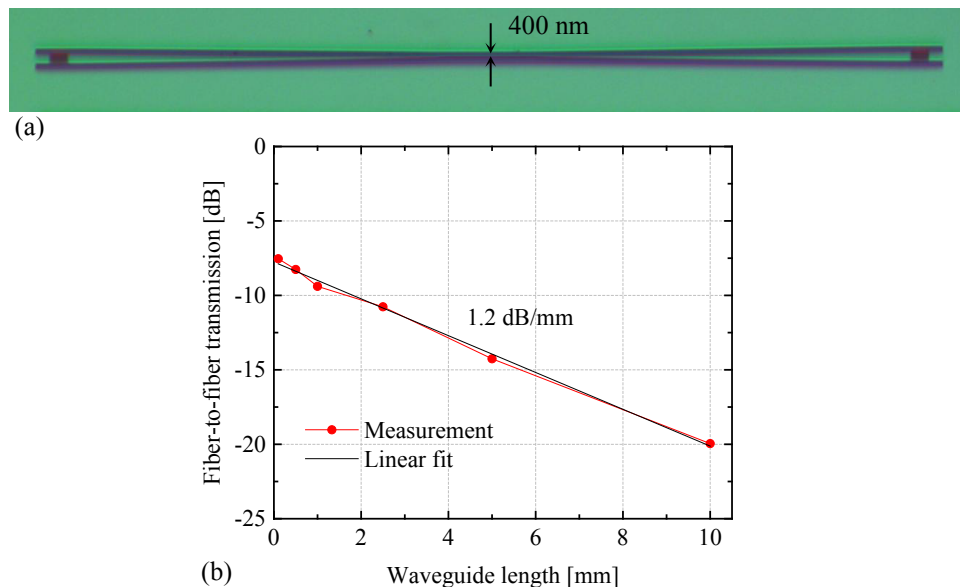


Figure D.2: (a) Microscopic picture of a structure composed of two gratings linked by two tapers and a $400\ \text{nm}$ wide waveguide. (b) Measured transmission as a function of the waveguide length at $1550\ \text{nm}$ for TE polarization.

E. 1D Bragg gratings for TM coupling

In this thesis, only coupling of the TE polarization based on 1D Bragg gratings is considered. In order to couple light using a polarization-independent configuration, 2D gratings can also be used with the additional functionality to rotate the other orthogonal TM polarization inherently into the TE mode.

When a pure TM wave has to be coupled, the period of the 1D grating has to be calculated accordingly since the effective refractive index of the fundamental TM mode is lower than that in the TE case. Alternatively, the 1D grating can be designed to couple both TE and TM waves in a polarization splitting configuration.

E.1. Single polarization coupling

Based on the calculations in the fourth chapter, coupling of a pure TM wave to the first diffraction order $m = 1$ can be realized for example at $\alpha_i = 9^\circ$ and $\lambda_0 = 1550$ nm using $\Lambda = 860$ nm. The coupling efficiency spectrum of this periodic structure, including a metal mirror underneath, is illustrated in Figure E.1 with a maximum value of -1 dB. In order to enhance the transmission, the grating elements are optimized based on the introduced algorithm, and the simulated coupling efficiency is also shown in the same graph. In this case, the efficiency at 1550 nm is increased to -0.33 dB. The dimensions of the individual ribs and grooves are listed in Table E.1.

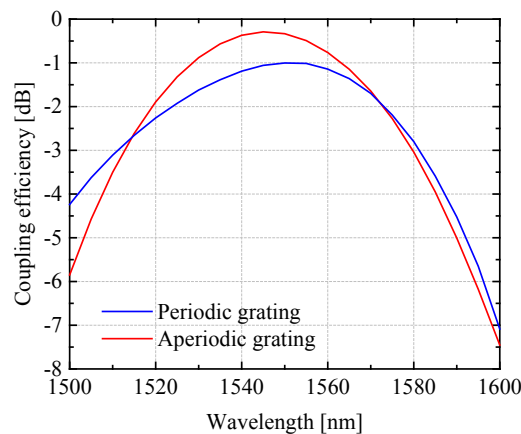


Figure E.1: Simulated coupling efficiency spectrum for TM coupling at $\alpha_i = 9^\circ$ using a periodic grating with $\Lambda = 860$ nm and an aperiodic grating with the dimensions listed in Table E.1. The BOX thickness is $2.96 \mu\text{m}$.

Table E.1: Dimensions of the optimized nonuniform grating for TM coupling in nm. g_1 corresponds to the length of the nearest groove to the output waveguide.

g_1	b_1	g_2	b_2	g_3	b_3	g_4	b_4	g_5	b_5	g_6	b_6	g_7	b_7	g_8	b_8	g_9
60	733	62	730	87	674	98	683	104	665	158	629	383	454	384	465	386
b_9	g_{10}	b_{10}	g_{11}	b_{11}	g_{12}	b_{12}	g_{13}	b_{13}	g_{14}	b_{14}	g_{15}	b_{15}	g_{16}	b_{16}	g_{17}	b_{17}
475	344	482	388	490	338	490	358	486	366	503	318	495	382	463	368	472
g_{18}	b_{18}	g_{19}	b_{19}	g_{20}												
381	507	339	548	324												

E.2. Polarization beam splitting

The second method to couple a TM wave using a 1D grating relies on exciting a diffraction order different from the 0th and 1st modes. In this case, the structure is designed in a polarization splitting configuration by transmitting the TM wave to the other side of the waveguide following $m = -1$, while the TE wave is transmitted to the conventional direction following $m = 1$. This is achieved initially by determining the required combination of Λ and α_i .

In order to achieve identical transmission to both waveguide parts, the number of periods and the position of the fiber have to be additionally optimized in a second step. Using a periodic structure with $\Lambda = 640$ nm, $\alpha_i = 16^\circ$, $N = 15$, and having a metal mirror underneath, the coupling efficiency at 1550 nm reaches -1.5 dB for both polarizations with an extinction ratio better than 23 dB at the two outputs as shown in Figure E.2(a). Here outputs 1 and 2 correspond to the diffraction orders 1 and -1 respectively.

The efficiency is enhanced to more than -1.2 dB by optimizing the individual grating elements using a slightly modified algorithm [110], and the transmission spectrum of the aperiodic grating with the dimensions listed in Table E.2 is illustrated in Figure E.2(b). The extinction ratio is larger than 21 dB at 1550 nm and exceeds 20 dB in a wavelength range of more than 60 nm.

It should be noted that the common efficiency cannot reach the values obtained in the last subsection since the maximal transmission of each orthogonal polarization takes place at a different fiber position on the grating.

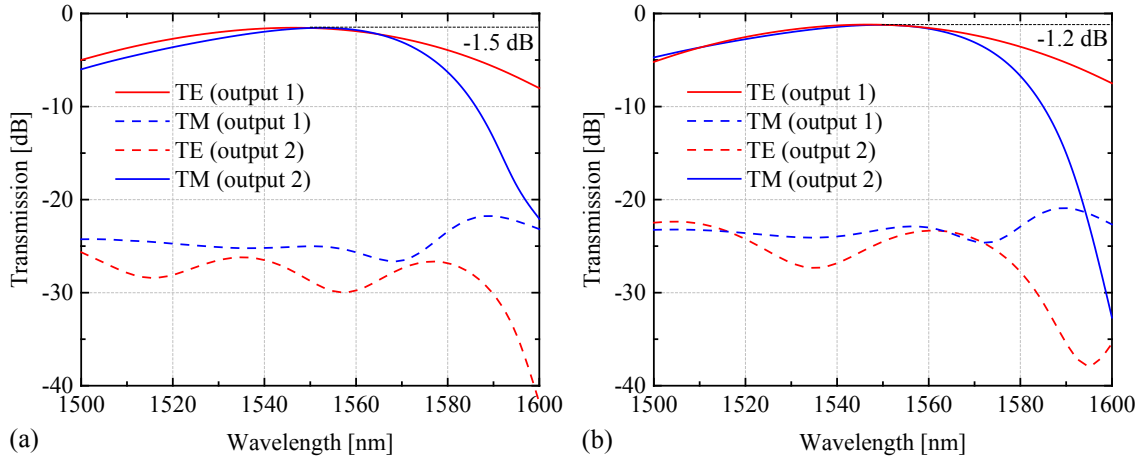


Figure E.2: (a) Simulated transmission spectrum at $\alpha_i = 16^\circ$ using (a) a periodic grating with $\Lambda = 640$ nm and (b) an aperiodic grating with the dimensions listed in Table E.1. The number of periods is 15 and the BOX thickness is $2.96 \mu\text{m}$. Both structures have a metal mirror to enhance the directionality.

Table E.2: Dimensions of the optimized nonuniform polarization beam splitter in nm [36]. g_1 corresponds to the length of the nearest groove to the TE output.

g_1	b_1	g_2	b_2	g_3	b_3	g_4	b_4	g_5	b_5	g_6	b_6	g_7	b_7	g_8	b_8	g_9
204	391	302	368	288	352	288	352	307	333	294	346	310	340	293	343	294
b_9	g_{10}	b_{10}	g_{11}	b_{11}	g_{12}	b_{12}	g_{13}	b_{13}	g_{14}	b_{14}	g_{15}					
339	299	341	290	321	324	307	350	281	335	345	171					

References

- [1] “Cisco visual networking index: forecast and methodology, 2012-2017,” Cisco Systems (2013).
- [2] “The Nobel Prize in Physics 2009,” Information for the public, The Royal Swedish Academy of Sciences (2009).
- [3] “London apartment blocks get gigabit speeds,” FTTH case study, FTTH Council Europe (2013).
- [4] D. Qian, M.F. Huang, E. Ip, Y.K. Huang, Y. Shao, J. Hu, and T. Wang, “101.7-Tb/s (370×294-Gb/s) PDM-128QAM-OFDM transmission over 3×55-km SSMF using pilot-based phase noise mitigation,” Optical Fiber Communication Conference, Los Angeles, USA, PDPB5 (2011).
- [5] H. Takara, A. Sano, T. Kobayashi, H. Kubota, H. Kawakami, A. Matsuura, Y. Miyamoto, Y. Abe, H. Ono, K. Shikama, Y. Goto, K. Tsujikawa, Y. Sasaki, I. Ishida, K. Takenaga, S. Matsuo, K. Saitoh, M. Koshihara, and T. Morioka, “1.01-Pb/s (12 SDM/222 WDM/456 Gb/s) crosstalk-managed transmission with 91.4-b/s/Hz aggregate spectral efficiency,” European Conference on Optical Communication, Amsterdam, The Netherlands, Th.3.C.1 (2012).
- [6] R.E. Camacho-Aguilera, Y. Cai, N. Patel, J.T. Bessette, M. Romagnoli, L.C. Kimmerling, and J. Michel, “An electrically pumped germanium laser,” *Optics Express*, Vol. 20, No. 10, 11316-11320 (2012).
- [7] “Corning SMF-28 optical fiber,” Product information, Corning (2002).
- [8] A. Andryieuski and A.V. Lavrinenko, “Nanocouplers for infrared and visible light,” *Advances in OptoElectronics*, doi:10.1155/2012/839747 (2012).
- [9] R. Takei, M. Suzuki, E. Omoda, S. Manako, T. Kamei, M. Mori, and Y. Sakakibara, “Silicon knife-edge taper waveguide for ultralow-loss spot-size converter fabricated by photolithography,” *Applied Physics Letters* 102, 101108 (2013).

- [10] M. Pu, L. Liu, H. Ou, K. Yvind, and J.M. Hvam, "Ultra-low-loss inverted taper coupler for silicon-on-insulator ridge waveguide," *Optics Communications* 283, 3678-3682 (2010).
- [11] A. Mekis, S. Gloeckner, G. Masini, A. Narasimha, T. Pinguet, S. Sahni, and P. De Dobbelaere, "A grating-coupler-enabled CMOS photonics platform," *IEEE Journal of Selected Topics in Quantum Electronics*, Vol. 17, No. 3, 597-608 (2011).
- [12] D. Vermeulen, S. Selvaraja, P. Verheyen, G. Lepage, W. Bogaerts, P. Absil, D. Van Thourhout, and G. Roelkens, "High-efficiency fiber-to-chip grating couplers realized using an advanced CMOS-compatible silicon-on-insulator platform," *Optics Express*, Vol. 18, No. 17, 18278-18283 (2010).
- [13] X. Chen and H.K. Tsang, "Engineering of silicon-on-insulator waveguide gratings for coupling to optical fibers," *Proceedings of Opto-Electronics and Communications Conference, Kaohsiung, Taiwan*, pp. 845-846 (2011).
- [14] A. Mekis, S. Abdalla, D. Foltz, S. Gloeckner, S. Hovey, S. Jackson, Y. Liang, M. Mack, G. Masini, M. Peterson, T. Pinguet, S. Sahni, M. Sharp, P. Sun, D. Tan, L. Verslegers, B.P. Welch, K. Yokoyama, S. Yu, and P.M. De Dobbelaere, "A CMOS photonics platform for high-speed optical interconnects," *Proceedings of IEEE Photonics Conference, Burlingame, USA*, pp. 356-357 (2012).
- [15] J.B. Pendry, D. Schurig, and D.R. Smith, "Controlling electromagnetic fields," *Science*, Vol. 312, 1780-1782 (2006).
- [16] Y. Urino, S. Akiyama, T. Akagawa, T. Baba, T. Usuki, D. Okamoto, M. Miura, J. Fujikata, T. Shimizu, M. Okano, N. Hatori, M. Ishizaka, T. Yamamoto, H. Takahashi, Y. Noguchi, M. Noguchi, M. Imai, M. Yamagishi, S. Saitou, N. Hirayama, M. Takahashi, E. Saito, D. Shimura, H. Okayama, Y. Onawa, H. Yaegashi, H. Nishi, H. Fukuda, K. Yamada, M. Mori, T. Horikawa, T. Nakamura, and Y. Arakawa, "Demonstration of 30-Tbps/cm² bandwidth density by silicon optical interposers fully integrated with optical interconnects," *European Conference on Optical Communication, London, UK, Mo.4.B.2* (2013).
- [17] J.D. Love, "Spot size, adiabaticity and diffraction in tapered fibres," *Electronics Letters*, Vol. 23, No. 19, 993-994 (1987).

- [18] K. Shiraishi, N. Kawasaki, H. Yoda, K. Watanabe, M. Umetsu, T. Hitomi, and K. Muro, "High-index-layer coating on a lensed fiber endface for enhanced focusing power," *Journal of Lightwave Technology*, Vol. 27, No. 7, 864-870 (2009).
- [19] K. Shiraishi, M. Kagaya, K. Muro, H. Yoda, Y. Kogami, and C.S. Tsai, "Single-mode fiber with a plano-convex silicon microlens for an integrated butt-coupling scheme," *Applied Optics*, Vol. 47, No. 34, 6345-6349 (2008).
- [20] S. Scheerlinck, D. Taillaert, D. Van Thourhout, and R. Baets, "Flexible metal grating based optical fiber probe for photonic integrated circuits," *Applied Physics Letters* 92, 031104 (2008).
- [21] F. Renna, G. Brambilla, and D.C. Cox, "Light confinement in optical fibers using surface plasmon polaritons," *IEEE Photonics Technology Letters*, Vol. 21, No. 20, 1508-1510 (2009).
- [22] T.J. Antosiewicz, P. Wróbel, and T. Szoplik, "Nanofocusing of radially polarized light with dielectric-metal-dielectric probe," *Optics Express*, Vol. 17, No. 11, 9191-9196 (2009).
- [23] Y. Liu, H. Xu, F. Stief, N. Zhitenev, and M. Yu, "Far-field superfocusing with an optical fiber based surface plasmonic lens made of nanoscale concentric annular slits," *Optics Express*, Vol. 19, No. 21, 20233-20243 (2011).
- [24] P.K. Tien and R. Ulrich, "Theory of prism-film coupler and thin-film light guides," *Journal of the Optical Society of America*, Vol. 60, No. 10, 1325-1337 (1970).
- [25] G.T. Reed and A.P. Knights, "Silicon photonics: an introduction," Wiley (2005).
- [26] T. Miyashita, "The microlens," in *Handbook of optical interconnects*, edited by S. Kawai, Taylor & Francis (2005).
- [27] L.S. Huang, S.S. Lee, E. Motamedi, M.C. Wu, and C.J. Kim, "MEMS packaging for micro mirror switches," *Proceedings of Electronic Components and Technology Conference*, Seattle, USA, pp. 592-597 (1998).
- [28] J.B. Pendry, "Negative refraction makes a perfect lens," *Physical Review Letters*, Vol. 85, No. 18, 3966-3969 (2000).
- [29] D. Schurig and D.R. Smith, "Negative index lens aberrations," *Physical Review E* 70, 065601 (2004).

- [30] B.D. Casse, W.T. Lu, Y.J. Huang, and S. Sridhar, "Nano-optical microlens with ultrashort focal length using negative refraction," *Applied Physics Letters* 93, 053111 (2008).
- [31] Q. Meng, X. Zhang, L. Cheng, P. Cao, Y. Li, H. Zhang, and G. Wang, "Deep subwavelength focusing of light by a trumpet hyperlens," *Journal of Optics* 13, 075102 (2011).
- [32] D. Lu and Z. Liu, "Hyperlenses and metalenses for far-field super-resolution imaging," *Nature Communications* 3:1205, doi:10.1038/ncomms2176 (2012).
- [33] Q. Wang, T.H. Loh, D.K. Ng, and S.T. Ho, "Design and analysis of optical coupling between silicon nanophotonic waveguide and standard single-mode fiber using an integrated asymmetric super-GRIN lens," *IEEE Journal of Selected Topics in Quantum Electronics*, Vol. 17, No. 3, 581-589 (2011).
- [34] L.H. Gabrielli and M. Lipson, "Integrated Luneburg lens via ultra-strong index gradient on silicon," *Optics Express*, Vol. 19, No. 21, 20122-20127 (2011).
- [35] N. Fang, Z. Yang, A. Wu, J. Chen, M. Zhang, S. Zou, and X. Wang, "Three-dimensional tapered spot-size converter based on (111) silicon-on-insulator," *IEEE Photonics Technology Letters*, Vol. 21, No. 12, 820-822 (2009).
- [36] **W. Sfar Zaoui**, A. Kunze, W. Vogel, and M. Berroth, "CMOS-compatible polarization splitting grating couplers with a backside metal mirror," *IEEE Photonics Technology Letters*, Vol. 25, No. 14, 1395-1397 (2013).
- [37] Z. Zhang, Z. Zhang, B. Huang, C. Cheng, and H. Chen, "CMOS-compatible vertical grating coupler with quasi Mach-Zehnder characteristics," *IEEE Photonics Technology Letters*, Vol. 25, No. 3, 224-227 (2013).
- [38] G. Roelkens, D. Van Thourhout, and R. Baets, "Silicon-on-insulator ultra-compact duplexer based on a diffractive grating structure," *Optics Express*, Vol. 15, No. 16, 10091-10096 (2007).
- [39] F. Van Laere, T. Claes, J. Schrauwen, S. Scheerlinck, W. Bogaerts, D. Taillaert, L. O'Faolain, D. Van Thourhout, and R. Baets, "Compact focusing grating couplers for silicon-on-insulator integrated circuits," *IEEE Photonics Technology Letters*, Vol. 19, No. 23, 1919-1921 (2007).

- [40] E. Cubukcu, N. Yu, E.J. Smythe, L. Diehl, K.B. Crozier, and F. Capasso, "Plasmonic laser antennas and related devices," *IEEE Journal of Selected Topics in Quantum Electronics*, Vol. 14, No. 6, 1448-1461 (2008).
- [41] M.W. Knight, H. Sobhani, P. Nordlander, and N.J. Halas, "Photodetection with active optical antennas," *Science*, Vol. 332, 702-704 (2011).
- [42] A. Andryieuski, R. Malureanu, G. Biagi, T. Holmgaard, and A. Lavrinenko, "Compact dipole nanoantenna coupler to plasmonic slot waveguide," *Optics Letters*, Vol. 37, No. 6, 1124-1126 (2012).
- [43] P. De Dobbelaere, S. Abdalla, S. Gloeckner, M. Mack, G. Masini, A. Mekis, T. Pinguet, S. Sahni, D. Guckenberger, M. Harrison, and A. Narasimha, "Si photonics based high-speed optical transceivers," *European Conference on Optical Communication*, Amsterdam, The Netherlands, We.1.E.5 (2012).
- [44] J.M. Senior, *Optical fiber communications: principles and practice*, Pearson Education (2009).
- [45] G. Ghione, *Semiconductor devices for high-speed optoelectronics*, Cambridge University Press (2009).
- [46] Y. Achiam, A.M. Kaplan, and M. Seimetz, "Systems with higher-order modulation," in *Fibre optic communication: key devices*, edited by H. Venghaus and N. Grote, Springer (2012).
- [47] C. Zhang, S. Liang, H. Zhu, B. Wang, and W. Wang, "A modified SAG technique for the fabrication of DWDM DFB laser arrays with highly uniform wavelength spacings," *Optics Express*, Vol. 20, No. 28, 29620-29625 (2012).
- [48] "100G ultra long haul DWDM framework document," *Optical Internetworking Forum* (2009).
- [49] L.B. Soldano and E.C. Pennings, "Optical multi-mode interference devices based on self-imaging: principles and applications," *Journal of Lightwave Technology*, Vol. 13, No. 4, 615-627 (1995).
- [50] D. Taillaert, H. Chong, P.I. Borel, L.H. Frandsen, R.M. De La Rue, and R. Baets, "A compact two-dimensional grating coupler used as a polarization splitter," *IEEE Photonics Technology Letters*, Vol. 15, No. 9, 1249-1251 (2003).
- [51] C. Schubert, J.K. Fischer, C. Schmidt-Langhorst, R. Elschner, L. Molle, M. Nölle, and T. Richter, "New trends and challenges in optical digital transmission sys-

- tems,” European Conference on Optical Communication, Amsterdam, The Netherlands, We.1.C.1 (2012).
- [52] R. Syms and J. Cozens, *Optical guided waves and devices*, McGraw-Hill Book Company (1992).
- [53] P. Nouchi, P. Sillard, and D. Molin, “Optical fibers,” in *Fibre optic communication: key devices*, edited by H. Venghaus and N. Grote, Springer (2012).
- [54] “Beam divergence from an SMF-28 optical fiber,” Naval Research Laboratory (2006).
- [55] M. Seimetz, *High-order modulation for optical data transmission*, Springer (2009).
- [56] K.J. Ebeling, *Integrierte Optoelektronik*, Springer (1992).
- [57] J.D. Joannopoulos, S.G. Johnson, J.N. Winn, and R.D. Maede, *Photonic crystals: molding the flow of light*, Princeton University Press (2008).
- [58] G. Lehner, *Elektromagnetische Feldtheorie*, Springer (2010).
- [59] J.M. Ziman, *Principles of the theory of solids*, Cambridge University Press (1999).
- [60] S.A. Maier, *Plasmonics: fundamentals and applications*, Springer (2007).
- [61] M.A. Ordal, L.L. Long, R.J. Bell, S.E. Bell, R.R. Bell, R.W. Alexander, and C.A. Ward, “Optical properties of the metals Al, Co, Cu, Au, Fe, Pb, Ni, Pd, Pt, Ag, Ti, and W in the infrared and far infrared,” *Applied Optics*, Vol. 22, No. 7, 1099-1119 (1983).
- [62] M. Berroth, “Optoelectronic devices and circuits II,” *Scriptum*, University of Stuttgart (2011).
- [63] C.A. Bennett, *Principles of physical optics*, John Wiley & Sons (2007).
- [64] B.E. Saleh and M.C. Teich, *Fundamentals of photonics*, John Wiley & Sons (1991).
- [65] “Fundamental optics,” *Technical guide*, Melles Griot (2009).
- [66] S.G. Lipson, H.S. Lipson, and D.S. Tannhauser, *Optik*, translated by H. Becker, Springer (1997).
- [67] G.Z. Mashanovich, G.T. Reed, B.D. Timotijevic, and S.P. Chan, “Silicon photonic waveguides,” in *Silicon photonics: the state of the art*, edited by G.T. Reed, John Wiley & Sons (2008).

- [68] J.M. Liu, *Photonic devices*, Cambridge University Press (2005).
- [69] “RSoft BeamPROP,” User guide, Synopsys (2013).
- [70] Q. Xu, V.R. Almeida, C.A. Barrios, R.R. Panepucci, and M. Lipson, “Silicon void nano-waveguides for guiding and confining light,” Conference on Lasers and Electro-Optics, San Francisco, USA, CFH2 (2004).
- [71] D.N. Nikogosyan, “Multi-photon high-excitation-energy approach to fibre grating inscription,” *Measurement Science and Technology* 18, R1-R29 (2007).
- [72] A. Yariv and P. Yeh, *Optical waves in crystals: propagation and control of laser radiation*, John Wiley & Sons (1984).
- [73] L. Solymar and E. Shamonina, *Waves in metamaterials*, Oxford University Press (2009).
- [74] T. Driscoll, D.N. Basov, A.F. Starr, P.M. Rye, S. Nemat-Nasser, D. Schurig, and D.R. Smith, “Free-space microwave focusing by a negative-index gradient lens,” *Applied Physics Letters* 88, 081101 (2006).
- [75] M. Antelius, K.B. Gylfason, and H. Sohlström, “An apodized SOI waveguide-to-fiber surface grating coupler for single lithography silicon photonics,” *Optics Express*, Vol. 19, No. 4, 3592-3598 (2011).
- [76] S.A. Ramakrishna, “Physics of negative refractive index materials,” *Reports on Progress in Physics* 68, 449-521 (2005).
- [77] J.B. Pendry, A.J. Holden, W.J. Stewart, and I. Youngs, “Extremely low frequency plasmons in metallic mesostructures,” *Physical Review Letters*, Vol. 76, No. 25, 4773-4776 (1996).
- [78] J.B. Pendry, A.J. Holden, D.J. Robbins, and W.J. Stewart, “Magnetism from conductors and enhanced nonlinear phenomena,” *IEEE Transactions on Microwave Theory and Techniques*, Vol. 47, No. 11, 2075-2084 (1999).
- [79] R. Ortuno, C. García-Meca, F.J. Rodríguez-Fortuño, J. Martí, and A. Martínez, “Role of surface plasmon polaritons on optical transmission through double layer metallic hole arrays,” *Physical Review B* 79, 075425 (2009).
- [80] A. Andryieuski, C. Menzel, C. Rockstuhl, R. Malureanu, F. Lederer, and A. Lavrinenko, “Homogenization of resonant chiral metamaterials,” *Physical Review B* 82, 235107 (2010).

- [81] A.M. Nicolson and G.F. Ross, "Measurement of the intrinsic properties of materials by time-domain techniques," *IEEE Transactions on Instrumentation and Measurement*, Vol. IM-19, No. 4, 377-382 (1970).
- [82] X. Chen, T.M. Grzegorzczak, B.I. Wu, J. Pacheco, and J.A. Kong, "Robust method to retrieve the constitutive effective parameters of metamaterials," *Physical Review E* 70, 016608 (2004).
- [83] Y. Hao and R. Mittra, *FDTD modeling of metamaterials: theory and applications*, Artech House (2009).
- [84] X. Zhang and Z. Liu, "Superlenses to overcome the diffraction limit," *Nature Materials*, Vol. 7, 435-441 (2008).
- [85] V.A. Podolskiy and E.E. Narimanov, "Near-sighted superlens," *Optics Letters*, Vol. 30, No. 1, 75-77 (2005).
- [86] P. Kolinko and D.R. Smith, "Numerical study of electromagnetic waves interacting with negative index materials," *Optics Express*, Vol. 11, No. 7, 640-648 (2003).
- [87] R.B. Gregor, C.G. Parazzoli, J.A. Nielsen, M.A. Thompson, M.H. Tanielian, D.C. Vier, S. Schultz, D.R. Smith, and D. Schurig, "Microwave focusing and beam collimation using negative index of refraction lenses," *IET Microwave Antennas Propagation*, Vol. 1, No. 1, 108-115 (2007).
- [88] D.R. Smith, W.J. Padilla, D.C. Vier, S.C. Nemat-Nasser, and S. Schultz, "Composite medium with simultaneously negative permeability and permittivity," *Physical Review Letters*, Vol. 84, No. 18, 4184-4187 (2000).
- [89] G. Dolling, C. Enkrich, M. Wegener, J.F. Zhou, C.M. Soukoulis, and S. Linden, "Cut-wire pairs and plate pairs as magnetic atoms for optical metamaterials," *Optics Letters*, Vol. 30, No. 23, 3198-3200 (2005).
- [90] S. Zhang, W. Fan, K.J. Malloy, S.R. Brueck, N.C. Panoiu, and R.M. Osgood, "Near-infrared double negative metamaterials," *Optics Express*, Vol. 13, No. 13, 4922-4930 (2005).
- [91] G. Dolling, M. Wegener, C.M. Soukoulis, and S. Linden, "Negative-index metamaterial at 780 nm wavelength," *Optics Letters*, Vol. 32, No. 1, 53-55 (2007).

- [92] J. Valentine, S. Zhang, T. Zentgraf, E. Ulin-Avila, D.A. Genov, G. Bartal, and X. Zhang, "Three-dimensional optical metamaterial with a negative refractive index," *Nature*, Vol. 455, 376-379 (2008).
- [93] **W. Sfar Zaoui**, K. Chen, W. Vogel, and M. Berroth, "Low loss broadband polarization independent fishnet negative index metamaterial at 40 GHz," *Photonics and Nanostructures: Fundamentals and Applications*, Vol. 10, Iss. 3, 245-250 (2012).
- [94] "RT/duroid[®] 5880: glass microfiber reinforced polytetrafluoroethylene composite," Data sheet, Rogers Corporation (1999).
- [95] "CST Microwave Studio[®]: workflow and solver overview," Manual, Computer Simulation Technology (2008).
- [96] **W. Sfar Zaoui**, M. Nafe, M. Geng, W. Vogel, and M. Berroth, "Theoretical and experimental investigation of negative index fishnet metamaterial multilayers in the Q-band," *Waves in Random and Complex Media*, Vol. 24, No. 2, 149-163 (2014).
- [97] M.A. Nafe, **W. Sfar Zaoui**, and M. Berroth, "Simulation study of 3D polarization independent fishnet negative index metamaterials at 40 GHz," *International Conference on Aerospace Sciences and Aviation Technology*, Cairo, Egypt, 009-MS (2013).
- [98] R.A. Depine and A. Lakhtakia, "A new condition to identify isotropic dielectric-magnetic materials displaying negative phase velocity," *Microwave and Optical Technology Letters*, Vol. 41, No. 4, 315-316 (2004).
- [99] "Agilent RF and microwave test accessories," Agilent waveguide products data, Agilent Technologies (2000).
- [100] P.F. Goldsmith, T. Itoh, and K.D. Stephan, "Quasi-optical techniques," in *Handbook of microwave and optical components*, Vol. 1, edited by K. Chang, Wiley (1989).
- [101] "Material library," Electromagnetic properties of Teflon (PTFE), CST Microwave Studio.
- [102] N.H. Shen, T. Koschny, M. Kafesaki, and C.M. Soukoulis, "Optical metamaterials with different metals," *Physical Review B* 85, 075120 (2012).

- [103] G. Dolling, C. Enkrich, M. Wegener, C.M. Soukoulis, and S. Linden, "Low-loss negative-index metamaterial at telecommunication wavelengths," *Optics Letters*, Vol. 31, No. 12, 1800-1802 (2006).
- [104] X. Ni, S. Ishii, M.D. Thoreson, V.M. Shalaev, S. Han, S. Lee, and A.V. Kildishev, "Loss-compensated and active hyperbolic metamaterials," *Optics Express*, Vol. 19, No. 25, 25242-25254 (2011).
- [105] G.V. Naik, J. Kim, and A. Boltasseva, "Oxides and nitrides as alternative plasmonic materials in the optical range," *Optical Materials Express*, Vol. 1, No. 6, 1090-1099 (2011).
- [106] D. Taillaert, "Grating couplers as interface between optical fibres and nanophotonic waveguides," PhD thesis, Ghent University (2004).
- [107] W. Bogaerts and D. Vermeulen, "Off-chip coupling," in *Handbook of silicon photonics*, edited by L. Vivien and L. Pavesi, Taylor & Francis (2013).
- [108] W. Bogaerts, P. Dumon, D. Van Thourhout, D. Taillaert, P. Jaenen, J. Wouters, S. Beckx, V. Wiaux, and R.G. Baets, "Compact wavelength-selective functions in silicon-on-insulator photonic wires," *IEEE Journal of Selected Topics in Quantum Electronics*, Vol. 12, No. 6, 1394-1401 (2006).
- [109] C. Kopp, S. Bernabé, B. Ben Bakir, J.M. Fedeli, R. Orobtcouk, F. Schrank, H. Porte, L. Zimmermann, and T. Tekin, "Silicon photonic circuits: on-CMOS integration, fiber optical coupling, and packaging," *IEEE Journal of Selected Topics in Quantum Electronics*, Vol. 17, No. 3, 498-509 (2011).
- [110] A. Kunze, "Optimization and characterization of photonic integrated devices for optical datacommunication," Diploma thesis, University of Stuttgart (2013).
- [111] S.K. Selvaraja, D. Vermeulen, M. Schaekers, E. Sleetx, W. Bogaerts, G. Roelkens, P. Dumon, D. Van Thourhout, and R. Baets, "Highly efficient grating coupler between optical fiber and silicon photonic circuit," *Conference on Lasers and Electro-Optics*, Baltimore, USA, CTuC6 (2009).
- [112] F. Van Laere, G. Roelkens, M. Ayre, J. Schrauwen, D. Taillaert, D. Van Thourhout, T.F. Krauss, and R. Baets, "Compact and highly efficient grating couplers between optical fiber and nanophotonic waveguides," *Journal of Lightwave Technology*, Vol. 25, No. 1, 151-156 (2007).

- [113] C. Kopp, E. Augendre, R. Orobtcouk, O. Lemonnier, and J.M. Fedeli, “Enhanced fiber grating coupler integrated by wafer-to-wafer bonding,” *Journal of Lightwave Technology*, Vol. 29, No. 12, 1847-1851 (2011).
- [114] **W. Sfar Zaoui**, M. Félix Rosa, W. Vogel, M. Berroth, J. Butschke, and F. Letzkus, “High-efficient CMOS-compatible grating couplers with backside metal mirror,” *European Conference on Optical Communication*, Amsterdam, The Netherlands, Tu.1.E.2 (2012).
- [115] “Unibond™ Wafers: G6P-141-01,” Data sheet, SOITEC (2009).
- [116] Y. Tang, Z. Wang, L. Wosinski, U. Westergren, and S. He, “Highly efficient non-uniform grating coupler for silicon-on-insulator nanophotonic circuits,” *Optics Letters*, Vol. 35, No. 8, 1290-1292 (2010).
- [117] **W. Sfar Zaoui**, A. Kunze, W. Vogel, M. Berroth, J. Butschke, F. Letzkus, and J. Burghartz, “Bridging the gap between optical fibers and silicon photonic integrated circuits,” *Optics Express*, Vol. 22, No. 2, 1277-1286 (2014).
- [118] “CAMFR manual,” P. Bienstman, Ghent University (2007).
- [119] J. Butschke, A. Ehrmann, B. Höfflinger, M. Imscher, R. Käsmaier, F. Letzkus, H. Löschner, J. Mathuni, C. Reuter, C. Schomburg, and R. Springer, “SOI wafer flow process for stencil mask fabrication,” *Microelectronic Engineering*, Vol. 46, Iss. 1-4, 473-476 (1999).
- [120] J. Butschke and F. Letzkus, “Process flow description,” Personal communication (2012).
- [121] “Cargille fused silica matching liquid code 50350,” Data sheet, Cargille Laboratories (2002).
- [122] Personal information from J. Butschke (2014).
- [123] I.N. Bronstein, K.A. Semendjajew, G. Musiol, and H. Mühlig, *Taschenbuch der Mathematik*, Harri Deutsch (2005).
- [124] M. Kafesaki, I. Tsiapa, N. Katsarakis, T. Koschny, C.M. Soukoulis, and E.N. Economou, “Left-handed metamaterials: the fishnet structure and its variations,” *Physical Review B* 75, 235114 (2007).
- [125] N. Gagnon, “Design and study of a free-space quasi-optical measurement system,” Master thesis, University of Ottawa (2002).

Personal publications

- [P.1] **W. Sfar Zaoui**, “Efficient focusing based on fishnet negative index metamaterial lenses at radio frequencies,” CST European User Conference, Berlin, Germany, 6.3.3 (2014).
- [P.2] **W. Sfar Zaoui**, M. Berroth, J. Butschke, and F. Letzkus, “High-efficient CMOS-compatible grating couplers with backside metal mirror,” European Patent Application, EP 2 703 858 A1 (2014).
- [P.3] **W. Sfar Zaoui**, M. Nafe, M. Geng, W. Vogel, and M. Berroth, “Theoretical and experimental investigation of negative index fishnet metamaterial multilayers in the Q-band,” *Waves in Random and Complex Media*, Vol. 24, No. 2, 149-163 (2014).
- [P.4] **W. Sfar Zaoui**, A. Kunze, W. Vogel, M. Berroth, J. Butschke, F. Letzkus, and J. Burghartz, “Bridging the gap between optical fibers and silicon photonic integrated circuits,” *Optics Express*, Vol. 22, No. 2, 1277-1286 (2014).
- [P.5] **W. Sfar Zaoui**, A. Kunze, W. Vogel, M. Berroth, J. Butschke, and F. Letzkus, “CMOS-compatible nonuniform grating coupler with 86% coupling efficiency,” European Conference on Optical Communication, London, UK, Mo.3.B.3 (2013).
- [P.6] **W. Sfar Zaoui**, A. Kunze, W. Vogel, and M. Berroth, “CMOS-compatible polarization splitting grating couplers with a backside metal mirror,” *IEEE Photonics Technology Letters*, Vol. 25, No. 14, 1395-1397 (2013).
- [P.7] M.A. Nafe, **W. Sfar Zaoui**, and M. Berroth, “Simulation study of 3D polarization independent fishnet negative index metamaterials at 40 GHz,” International Conference on Aerospace Sciences and Aviation Technology, Cairo, Egypt, 009-MS (2013).
- [P.8] **W. Sfar Zaoui**, M. Félix Rosa, W. Vogel, M. Berroth, J. Butschke, and F. Letzkus, “Cost-effective CMOS-compatible grating couplers with backside metal

- mirror and 69% coupling efficiency,” *Optics Express*, Vol. 20, No. 26, B238-B243 (2012).
- [P.9] M. Berroth, T. Föhn, **W. Sfar Zaoui**, W. Vogel, T. Veigel, and M. Grözing, “Electronic and photonic circuits for optical links beyond 100 Gb/s,” *Joint Symposium on Opto- and Microelectronic Devices and Circuits*, Hangzhou, China, M09 (2012).
- [P.10] **W. Sfar Zaoui**, M. Félix Rosa, W. Vogel, and M. Berroth, “Grating coupler serving as polarization beam splitter in silicon-on-insulator platform,” *Joint Symposium on Opto- and Microelectronic Devices and Circuits*, Hangzhou, China, M07 (2012).
- [P.11] **W. Sfar Zaoui**, M. Félix Rosa, W. Vogel, M. Berroth, J. Butschke, and F. Letzkus, “High-efficient CMOS-compatible grating couplers with backside metal mirror,” *European Conference on Optical Communication*, Amsterdam, The Netherlands, Tu.1.E.2 (2012).
- [P.12] **W. Sfar Zaoui**, K. Chen, W. Vogel, and M. Berroth, “Low loss broadband polarization independent fishnet negative index metamaterial at 40 GHz,” *Photonics and Nanostructures: Fundamentals and Applications*, Vol. 10, Iss. 3, 245-250 (2012).
- [P.13] M. Berroth, W. Vogel, **W. Sfar Zaoui**, T. Föhn, and S. Klinger, “Silicon photonic devices for advanced modulation formats,” *ITG-Workshop*, Nürnberg, Germany, invited paper (2011).
- [P.14] **W. Sfar Zaoui**, S. Klinger, W. Vogel, and M. Berroth, “Photonic crystal polarization beam splitter in silicon-on-insulator platform,” *Proceedings of the Joint Symposium on Opto- and Microelectronic Devices and Circuits*, Berlin, Germany, pp. 75-78 (2010).
- [P.15] **W. Sfar Zaoui**, K. Chen, W. Vogel, and M. Berroth, “Novel low loss broadband polarization independent fishnet negative index metamaterials at 40 GHz,” *International Conference on Photonic and Electromagnetic Crystal Structures*, Granada, Spain (2010).
- [P.16] J.E. Bowers, A. Ramaswamy, D. Dai, **W. Sfar Zaoui**, Y. Kang, T. Yin, and M. Morse, “Recent advances in Ge/Si PIN and APD photodetectors,” *Physica Status Solidi C*, 1-6 (2010).

- [P.17] J.E. Bowers, D. Dai, **W. Sfar Zaoui**, Y. Kang, and M. Morse, "Resonant Si/Ge avalanche photodiode with an ultrahigh gain bandwidth product," IEEE Photonics Society Winter Topicals Meeting Series, Majorca, Spain, WC2.2, invited paper (2010).
- [P.18] Y. Kang, M. Morse, M.J. Paniccia, M. Zadka, Y. Saad, G. Sarid, A. Pauchard, **W. Sfar Zaoui**, H.W. Chen, D. Dai, J.E. Bowers, H.D. Liu, D.C. McIntosh, X. Zheng, and J.C. Campbell, "Monolithic Ge/Si avalanche photodiodes," Group IV Photonics, San Francisco, USA, WB6 (2009).
- [P.19] S. Klinger, M. Grözing, **W. Sfar Zaoui**, M. Berroth, M. Kaschel, M. Oehme, E. Kasper, and J. Schulze, "Ge on Si p-i-n photodiodes for a bit rate of up to 25 Gbit/s," European Conference on Optical Communication, Vienna, Austria, 9.2.3 (2009).
- [P.20] **W. Sfar Zaoui**, H.W. Chen, J.E. Bowers, Y. Kang, M. Morse, M.J. Paniccia, A. Pauchard, and J.C. Campbell, "Frequency response and bandwidth enhancement in Ge/Si avalanche photodiodes with over 840GHz gain-bandwidth-product," Optics Express, Vol. 17, No. 15, 12641-12649 (2009).
- [P.21] J.E. Bowers, A. Ramaswamy, D. Dai, **W. Sfar Zaoui**, Y. Kang, and T. Yin, "CMOS-compatible Ge/Si photodetectors," International Symposium on Compound Semiconductors, Santa Barbara, USA, invited paper (2009).
- [P.22] Y. Kang, H.D. Liu, M. Morse, M.J. Paniccia, M. Zadka, S. Litski, G. Sarid, A. Pauchard, Y.H. Kuo, H.W. Chen, **W. Sfar Zaoui**, J.E. Bowers, A. Beling, D.C. McIntosh, X. Zheng, and J.C. Campbell, "Epitaxially-grown germanium/silicon avalanche photodiodes for near infrared light detection," Conference on Enabling Photonics Technologies for Defense, Security and Aerospace Applications, Orlando, USA, invited paper (2009).
- [P.23] **W. Sfar Zaoui**, H.W. Chen, J.E. Bowers, Y. Kang, M. Morse, M.J. Paniccia, A. Pauchard, and J.C. Campbell, "Origin of the gain-bandwidth-product enhancement in separate-absorption-charge-multiplication Ge/Si avalanche photodiodes," Optical Fiber Communication Conference, San Diego, USA, OMR6 (2009).
- [P.24] M. Piels, A. Ramaswamy, **W. Sfar Zaoui**, J.E. Bowers, Y. Kang, and M. Morse, "Microwave nonlinearities in Ge/Si avalanche photodiodes having a gain-

- bandwidth product of 300 GHz,” Optical Fiber Communication Conference, San Diego, USA, OMR1 (2009).
- [P.25] Y. Kang, H.D. Liu, M. Morse, M.J. Paniccia, M. Zadka, S. Litski, G. Sarid, A. Pauchard, Y.H. Kuo, H.W. Chen, **W. Sfar Zaoui**, J.E. Bowers, A. Beling, D.C. McIntosh, X. Zheng, and J.C. Campbell, “Monolithic germanium/silicon avalanche photodiodes with 340 GHz gain-bandwidth product,” *Nature Photonics* 3, 59-63 (2008).
- [P.26] A. Rumberg, **W. Sfar Zaoui**, and M. Berroth, “Focusing and coupling into dielectric waveguides with dielectric and metallic photonic crystals,” *Proceedings of the German Microwave Conference, Hamburg, Germany*, pp. 424-427 (2008).

Curriculum Vitae

Personal information

Name	Wissem Sfar Zaoui
Date of birth	September 1 st , 1983
Place of birth	Sousse, Tunisia

Academic education

Feb. 2009 – present	University of Stuttgart, Germany Scientific researcher at the Institute of Electrical and Optical Communications Engineering
May 2008 – Nov. 2008	University of California Santa Barbara, USA Diploma thesis at the Department of Electrical and Computer Engineering
Oct. 2003 – Nov. 2008	University of Stuttgart, Germany Electrical engineering studies, degree: Dipl.-Ing.
Sept. 2002 – June 2003	Heidelberg University, Germany German language proficiency test
Sept. 1998 – June 2002	Lycée Tahar Sfar Mahdia, Tunisia Baccalaureate

Practical experience

Oct. 2007 – Apr. 2008	Agilent Technologies, Photonic Test Division, Böblingen, Germany
July 2007 – Sept. 2007	University of Tokyo, Research Center for Advanced Science and Technology, Japan
July 2003 – Sept. 2003	Heidelberger Druckmaschinen, Wiesloch, Germany

Acknowledgment

I would like to acknowledge all those who supported me during my thesis at the Institute of Electrical and Optical Communications Engineering (INT) at the University of Stuttgart and contributed to the success of this work.

First of all, I thank Prof. Manfred Berroth for giving me the opportunity to be involved in such interesting research topics, for his supervision, continuous encouragement, and faith in me.

I also thank Prof. Joachim Burghartz for agreeing to be the co-examiner and for the close collaboration between IMS CHIPS and INT, which has delivered very fruitful results.

Many thanks go to my colleagues Felix Lang, Damir Ferenci, and Thomas Alpert who made my time at the INT both pleasant and joyous.

I am also indebted to all the students who supported my researches during their Bachelor, Master, and Diploma theses, especially Andreas Kunze.

Furthermore, I would like to thank Jörg Butschke and Florian Letzkus from IMS CHIPS for the technological facilities, Jelde Elling from IHFG for the SEM pictures, and Andrei Andryieuski from the Technical University of Denmark for his valuable recommendations.

Particular thanks go in addition to Wolfgang Vogel, Niklas Hoppe, Andreas Kunze, and Martin Hill for proofreading this dissertation.

Finally, I owe my greatest gratitude to my parents, my sisters, and my wife, Nadia. Their continuous support has brought me much hope and is the most precious reason for me to keep trying.